SHALLOW FLOW TURBULENCE:

AN EXPERIMENTAL STUDY

A thesis

submitted in partial fulfilment

of the requirements for the Degree

of

Master of Civil Engineering

in the

University of Canterbury

by

W. B. Veale

University of Canterbury

Christchurch, New Zealand

2005

Abstract

A particle tracking velocimetry (PTV) system is used to investigate the turbulent properties at the free surface of shallow shear flows and a shallow vortex street (VS) wake flow. The resolution of the PTV system enables information to be gathered regarding the large-scale turbulent structure of these flows, and also enables analysis to proceed in both the temporal and spatial domains. Statistical tools such as the probability density function (PDF), autocorrelation and power spectral density (PSD) are utilised to characterise the turbulent properties at the flow surface.

Two supercritical flows and one subcritical shallow shear flow are analysed. Taylor's frozen turbulence hypothesis is shown to be valid for these flows, and the integral length scales indicate that 2D isotropic structures with scales larger than the flow depth are present at the free surface. Such large-scale structures at the free surface are consistent with observations from dye visualisation experiments and with "spiral eddies" identified by Kumar, et al (1998).

The longitudinal extent of near and intermediate wake fields for the shallow VS wake flow is well defined by the integral wake length scale specified by v.Carmer (2005). The near wake region is characterised by high rates of exchange between the mean flow and large-scale 2D coherent structures (2DCS). In the intermediate field, the rate of decay of the turbulent stress components greatly diminishes as the 2DCS are stabilised and dissipated under the action of bed friction. Multiple peaks are observed in the power spectral density (PSD) of the turbulent fluctuations. The periodic shedding of 2DCS behind the circular cylinder is characterised by an energy peak at a Strouhal number of 0.21, and further energy peaks are observed in the near-wake region. The PSD estimates are consistent with the findings of v.Carmer (2005) in which a -5/3 decay law to high frequencies is observed, and no evidence of an inverse energy cascade is present.

Acknowledgements

Firstly I would like to extend thanks to my supervisors, Dr Roger Nokes at the University of Canterbury and Dr Vladimir Nikora, at the National Institute of Water and Atmospheric Research (NIWA). I am indebted to the support, enthusiasm, insight and assistance you both provided throughout the course of this project.

Many thanks also go to Ian Sheppard, Kevin Wines (University of Canterbury) and Glenn Cooper (NIWA), whose skills were invaluable in manufacturing, fixing and finding anything to do with the technical side of this project.

I would also like to thank the University of Canterbury for providing financial support during the initial stage of this Masters degree. Finally, I wish to thank Frances, and fellow fluids post-grads Gustaff, Andrew, Langford and Dave for their continued support throughout the course of this project.

Table of Contents

List of Figures

List of Symbols

Lower Case Latin

c_f	Skin friction coefficient	–
d_p	Particle diameter	m
g	Gravitational acceleration	m/s^2
k	Wavenumber ($k = 1/\lambda$)	$1/m$
k_e	Turbulent kinetic energy per unit mass	m^2/s^2
k_f	Forcing wavenumber	$1/m$
ℓ_M	Integral wake length scale	m
f	Frequency	$1/s$
f_s	Sampling frequency	$1/s$
n	Order of structure function	–
p_i	Pressure component (index notation)	N/m^2
$p(r)$	Probability density function of variable r	–
$\hat{r}$	Standardised variable r ($\hat{r} = (r - \overline{R})/\sigma_r$)	–
t	Time	s
t_0	Initial sampling time	s
u	Instantaneous longitudinal (streamwise) velocity component	m/s
u_i	Instantaneous velocity component (index notation)	m/s
u_i'	Fluctuating velocity component (index notation)	m/s
$u'_{i\,rms}$	RMS velocity component (index notation)	m/s
u_ℓ	Velocity scale of large scale turbulent structures	m/s
u_*	Shear velocity	m/s
v	Instantaneous transverse (spanwise) velocity component	m/s
w	Instantaneous vertical velocity component	m/s
x	Longitudinal (streamwise) direction	m
y	Transverse (spanwise) direction	m
y^+	Wake half-width	–
z	Vertical direction	m

Upper Case Latin

D	Cylinder diameter	m
$D_{Gu_in_i}$	Generalised structure function of order n_i for velocity component u_i	m^{n_i}/s^{n_i}
$D_{Ku_in_i}$	Kolmogorov structure function of order n_i for velocity component u_i	m^{n_i}/s^{n_i}

Fl	Flatness	–
Fr	Froude number	–
H	Flow depth	m
K	Kurtosis	–
L	Characteristics length scale of large scale turbulent structures	m
L_{∂}	Turbulent boundary layer development length	m
L_f	Eddy formation length	m
L_{u_i}	Integral length scale for velocity component u_i	m
N	Number of experiments	–
$P(r)$	Probability of variable r	–
R	Hydraulic radius	m
$R_{u_i}(\Delta x_i)$	Spatial autocorrelation function for velocity component u_i	–
$R_{u_i}(\tau)$	Temporal autocorrelation function for velocity component u_i	–
Re	Reynolds number	–
Re_H	Reynolds number based on depth	–
Re_{4R}	Reynolds number based on hydraulic radius	–
Re_D	Reynolds number based on cylinder diameter	–
S	Channel slope	–
St	Strouhal number	–
S_{ws}	Wake stability parameter	–
S_{u_i}	Power spectral density for velocity component u_i	$m^2/s^2/units$
Sk	Skewness	–
T_{u_i}	Integral time scale for velocity component u_i	s
T_s	Temporal sampling interval	s
U_a	Depth averaged velocity	m/s
U_0	Free stream velocity	m/s
U_s	Surface velocity	m/s
U^+	Velocity deficit	–
$\overline{U_i}$	Time averaged velocity component (index notation)	m/s
ΔX_s	Spatial sampling interval	m

Greek

δ	Turbulent boundary layer thickness	m
ε	Roughness height	m
ε_e	Turbulent energy dissipation rate	m^2/s^3
ζ_n	Exponent of structure function of order n	–
η	Kolmogorov length scale	m
$\dot{\eta}$	Enstrophy dissipation rate	$1/s^3$

λ	Wavelength	m
λ_ℓ	Horizontal length scale	m
v_η	Kolmogorov velocity scale	m/s
ρ	Density	kg/m^3
σ_r	Standard Deviation of variable r	$units$
σ_r^2	Variance of variable r	$units^2$
τ	Temporal delay	s
τ_0	Bed shear stress	$kg/m.s^2$
τ_η	Kolmogorov time scale	s
τ_s	Particle response time scale	s
υ	Kinematic viscosity	m^2/s
Δx_i	Spatial delay	m

Symbols

$\overline{\quad}$	Time-average
$\langle\ \rangle$	Ensemble average

Abbreviations

$2D$	Two-dimensional
$2DCS$	Two-dimensional coherent structure
$3D$	Three-dimensional
CCD	Charge coupled device
CFD	Computational fluid dynamics
LDV	Laser Doppler velocimetry
PDF	Probability density function
PIV	Particle image velocimetry
PP	Polypropylene
PSD	Power spectral density
PTV	Particle tracking velocimetry
RMS	Root mean square
SB	Steady bubble
TKE	Turbulent kinetic energy
UB	Unsteady bubble
VS	Vortex street

1.0 Introduction

Shallow flows are defined as fluid flows in which the lateral extent of the flow is much greater than the flow depth. Such flows are common in the environment, and examples can be found in the form of wide river channels, flow in estuaries, surface-water runoff, flow in shallow costal waters and stratified atmospheric flows.

Shallow flows exhibit two contrasting forms of turbulence. The first type of turbulent motion is three-dimensional and has scales of the order of the flow depth. 3D turbulence in an open-channel flow is generated by vertical shear, induced by instabilities in the boundary layer at the fixed bed, or by wind shear acting along the free surface. A second type of turbulent motion is induced by lateral shear, generated, for example, by a bridge pier. Due to the confinement of the water depth in the vertical dimension, lateral instabilities propagate freely in the horizontal plane and therefore acquire quasi two-dimensional characteristics, with length scales potentially much greater than the flow depth.

Examples of quasi-2D turbulence are depicted in Figure 1.1. In these images, a stably stratified flow in the lower atmosphere is pierced by island topography. Consequently lateral instabilities are generated, and coherent, large-scale, 2D turbulent structures are shed in the lee of the island, which are observed to propagate for large distances downstream. The organised pattern of the vortices is known as a von Karman vortex street.

Since shallow flows are ubiquitous in the environment, an understanding of 3D turbulence, as well as the formation and propagation of large-scale quasi-2D turbulent structures, is important to accurately predict pollutant transport, sediment transport and erosion processes, as well as to validate and refine computational fluid dynamic (CFD) models.

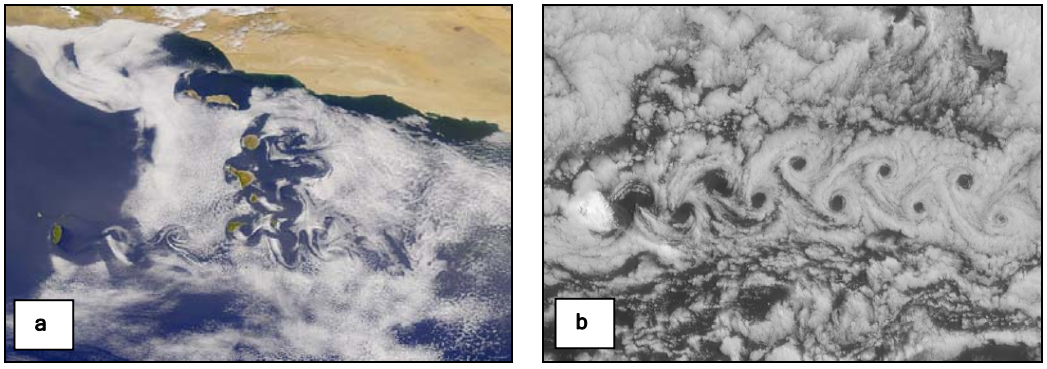

Figure 1.1 - **(a)** Large-scale, quasi-2D turbulent structures are evident in a von Karman vortex street wake, generated in the lower atmosphere due to obstruction of wind flow by the Canary and Malderia islands (located off the coast of Morocco) (NASA, 2005) **(b)** Quasi-2D turbulent structures are shed (as a von Karman vortex street wake), in the lower atmosphere over a distance of 300km south of Beerenberg volcano (elevated 2200m above sea level, located 650km northeast of Iceland) (NASA, 2005).

The present study will use particle tracking velocimetry (PTV) to explore the large-scale turbulent characteristics at the surface of shallow, turbulent shear flows and shallow, turbulent wake flows generated in the laboratory. The proposed research endeavours to contribute to the current understanding of turbulence confined to shallow flows and will also provide information on the limitations and abilities of a PTV system, using surface-tracer particles, to provide mean flow and turbulent data at the surface of shallow flows.

This report firstly provides the mathematical basis for analysing turbulent flows in Chapter 2. In Chapter 3, a background on the subject of shallow flows is presented, along with the key findings from recent research into shallow flow turbulence. The experimental objectives are detailed in Chapter 4, and the experimental apparatus and methods used to achieve these goals are then presented.

The experimental results are split into two chapters. Chapter 5 presents and discusses the experimental results from the analysis of shallow, uniform, turbulent shear flows. A circular cylinder was then introduced into the plane, shallow shear flows outlined in Chapter 5, in order to generate large-scale quasi-2D turbulent structures. Chapter 6 discusses the experimental data obtained for this shallow, turbulent wake flow. Finally, conclusions are drawn, and recommendations for the direction of future work are outlined in Chapter 7.

2.0 Background I: Turbulence

2.1 INTRODUCTION

Turbulence is the name given to the irregular, unsteady fluctuations that occur in fluid motion. An example of turbulent fluid motion is depicted in Figure 2.1, which displays turbulent emission of pyroclastic material from Mt Saint Helens. Since almost all industrial and environmental flows are turbulent, an understanding of turbulent motion is integral to any study in the fields of hydraulics and fluid mechanics.

Figure 2.1 - Turbulent plume of pyroclastic material, emitted from Mt Saint Helens (Corbis, 2005)

Turbulent flows always occur at high Reynolds numbers. The Reynolds number is defined in Eq. (2.1) where U_c and L_c are characteristic velocity and length scales of the flow respectively, and υ is the fluid viscosity.

$$\mathrm{Re} = \frac{U_c L_c}{\upsilon} \sim \frac{inertial\ forces}{viscous\ forces} \tag{2.1}$$

For an open channel flow at $\mathrm{Re} \gtrsim 1800$ (Pope, 2000), viscous forces do not suppress instabilities in the flow and a turbulent flow structure dominates. Turbulent fluid motion is highly rotational and three-dimensional; containing eddies, or fluctuating vorticity, over a range of different scales. Due to this unsteady, chaotic motion, turbulence induces rapid mixing and increased transfer rates of momentum, heat and mass. Turbulent flows also rapidly dissipate energy, and as a result require an energy source to be maintained. Such an energy source is usually provided by shear in the mean flow.

All flows considered in the present study are turbulent and therefore the following sections provide a brief overview of the field of turbulence. Section 2.2 presents the equations that govern turbulent fluid motion, and Sections 2.3 and 2.4 introduce mathematical techniques used to quantify turbulence.

2.2 GOVERNING EQUATIONS

The Navier-Stokes equations are a set of non-linear differential equations that govern the motion of an incompressible fluid. Eq. (2.2) denotes the Navier-Stokes equations in index notation, using a Cartesian coordinate system with axes, $x_1 = x$ (longitudinal), $x_2 = y$ (transverse) and $x_3 = z$ (vertical), and associated velocity components $u_1 = u$, $u_2 = v$ and $u_3 = w$. The symbol ρ denotes the fluid density, p the pressure term and g_i represents body forces (such as gravity).

$$\frac{\partial u_i}{\partial t} + u_j \frac{\partial u_i}{\partial x_j} = -\frac{1}{\rho}\frac{\partial p}{\partial x_i} + \upsilon \frac{\partial^2 u_i}{\partial x_j \partial x_j} + g_i \tag{2.2}$$

The Navier-Stokes equations contain four unknowns, u, v, w and p, each of which is a function of x, y, z and t. To solve for the dependent variables, a fourth equation is needed to close the system. This is provided by the continuity equation, defined in Eq. (2.3) for an incompressible fluid.

$$\frac{\partial u_i}{\partial x_i} = 0 \tag{2.3}$$

In a turbulent flow all four unknowns are continually changing with respect to time and space in a random, unsteady manner. This fact, coupled with the inherent complexity of the governing equations, means that no general solution to the Navier-Stokes equations exists for high Reynolds number turbulent flows.

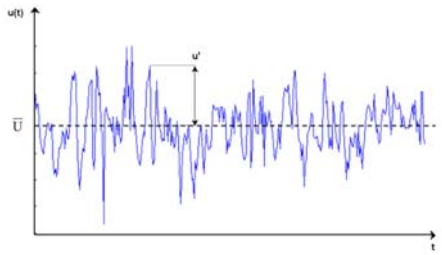

Figure 2.2 - Illustration of the streamwise velocity component measured over time at a fixed location in a shallow, turbulent channel flow.

In order to simplify the Navier-Stokes equations, Osborne Reynolds (*circa* 1880) decomposed the velocity into a mean and fluctuating part. This decomposition is illustrated in Figure 2.2 where the stream-wise velocity component, u, is measured over time at a fixed point in a turbulent flow. In general, the instantaneous velocity (u_i) is expressed as the sum of the mean ($\overline{U_i}$) and fluctuating velocity (u_i'), as expressed in Eq. (2.4). The mean, in this case, is taken over a time interval (further discussion on averaging procedures is outlined in Section 2.3.1).

$$u_i = \overline{U_i} + u_i' \tag{2.4}$$

When Eq. (2.2) is averaged and Reynolds decomposition of velocity and pressure is applied, the governing equations become the Reynolds-averaged Navier-Stokes equations (RANS), as defined in Eq. (2.5).

$$\frac{\partial \overline{U_i}}{\partial t} + \overline{U_j}\frac{\partial \overline{U_i}}{\partial x_j} = -\frac{1}{\rho}\frac{\partial \overline{P_i}}{\partial x_i} + \frac{\partial}{\partial x_j}\left(\upsilon\frac{\partial \overline{U_i}}{\partial x_j} - \overline{u_i' u_j'}\right) + g_i \tag{2.5}$$

The averaging procedure yields a turbulent stress term $-\overline{u_i' u_j'}$, which is commonly known as the Reynolds stress. The Reynolds stress quantifies mixing of momentum by turbulent motion within a flow (Glickman, 2000). However, since the stress term introduces six additional unknowns, the system is no longer closed (known as the closure problem of turbulence) and hence is unsolvable without the provision of additional equations. For this reason, turbulence remains one of the great, unsolved problems of modern science. Despite the lack of a deterministic solution for turbulent motion, many techniques can be still used to describe the properties and structure of turbulence. Some of these techniques are outlined in Sections 2.3 and 2.4.

2.3 A STATISTICAL DESCRIPTION OF TURBULENCE

A turbulent process is characterised by a continuous random fluctuation of a quantity (e.g. velocity, temperature, pressure) in time or space (v.Carmer, 2005). Although the exact turbulent signal is not reproducible, the bulk statistical properties that define the signal are. As a result of this, statistical methods are commonly used to quantify turbulence, and these techniques are outlined in the following sections.

2.3.1 Bulk Characteristics

The following analysis is restricted to a single, stationary, random turbulent component $r(t)$ measured over time at a fixed point in space. The same techniques can be applied to a turbulent component measured over space at a fixed time, $r(x_i)$, but this case is omitted for brevity.

The time-average (denoted with an overbar) for the instantaneous turbulent component, $r(t)$, is evaluated by Eq. (2.6). The mean flow needs to be steady over the sampling interval, so that the time interval (*T*) is independent of t_o (the initial sampling time). If this is not possible then an ensemble-average (denoted by brackets $\langle\ \rangle$) is employed which takes an average from *N* identical experiments (refer to Eq. (2.7)).

$$\overline{R} = \frac{1}{T}\int_{t_o}^{t_o+T} r(t)dt \tag{2.6}$$

$$\langle R \rangle = \frac{1}{N}\sum_{n=1}^{N} r_n(t) \tag{2.7}$$

Subtracting the mean from the instantaneous component yields the fluctuating component, $r' = r - \overline{R}$ as defined previously in Eq. (2.4). The mean-square of the fluctuating component, denoted $\sigma_r{}^2$ in Eq. (2.8), is defined as the variance of r. The root-mean-square (rms) of the fluctuating component is defined in Eq. (2.9), and is also known as the standard deviation, σ_r. The standard deviation provides a measure of how widely values are dispersed from the mean (Kennedy & Neville, 1986).

$$\sigma_r{}^2 = \overline{r'r'} \tag{2.8}$$

$$\sigma_r = \left(\overline{r'r'}\right)^{1/2} = r'_{rms} \tag{2.9}$$

2.3.2 The Probability Density Function

The previously defined statistics provide an indication of the bulk characteristics of a turbulent signal evaluated at a point in the flow. However to fully characterize a turbulent signal, the probability density function (PDF) is used.

A random variable can be plotted as a probability distribution by splitting the overall range of values of the random variable into a number of class intervals (or bins). The vertical axis then represents the probability (denoted P) of occurrence of the random variable for a given class interval, as depicted in Figure 2.3.

If the total number of observations of the random variable is increased indefinitely (i.e. to infinity) and the class width correspondingly approaches zero, the probability distribution will approach a continuous curve (Kennedy & Neville, 1986) as depicted in Figure 2.3. When the height of such a curve is scaled so that the area beneath the curve is equal to unity a probability density function results, as defined in Eq. (2.10) where $p(r)$ denotes the PDF. The probability (P) that the random variable r falls within the range $r_1 < r < r_2$ is given by integrating the PDF between the limits r_1 and r_2 (refer to Eq. (2.11)).

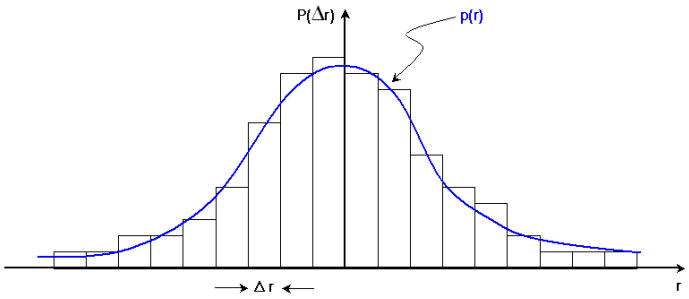

Figure 2.3 - The probability distribution is depicted as the probability of the random variable (P(Δr)) falling into a class interval (Δr). The probability density function (p(r)) results as the total number of observations of the random variable tends towards infinity, the class interval width approaches zero and the area under the curve scaled to unity.

$$\int_{-\infty}^{\infty} p(r)dr = 1 \tag{2.10}$$

$$P(r_1 < r < r_2) = \int_{r_1}^{r_2} p(r)dr \tag{2.11}$$

It should be noted that in the present study, all measurements are made over a finite sampling interval. Therefore all probability density functions published in the present study represent only a finite approximation of the theoretically continuous probability density function.

The PDF is commonly standardized by the mean and standard deviation of the signal according to Eq. (2.12). Standardisation centralises the distribution so that the mean is equal to zero and integer increments from zero represent multiples of the standard deviation.

$$\hat{r} = \frac{r - \overline{R}}{\sigma_r} \tag{2.12}$$

Taking the first and second moments of the PDF (Eq. (2.13) and Eq. (2.14) respectively) provides definitions for the mean and variance of the random variable. Note that the fluctuating component is used in Eq. (2.14) because the variance is associated with deviations from the mean.

$$\overline{R} = \int_{-\infty}^{\infty} (r)\, p(r)dr \tag{2.13}$$

$$\sigma_r{}^2 = \int_{-\infty}^{\infty} (r')^2\, p(r)dr \tag{2.14}$$

The third order moment, non-dimensionalised by the second order moment to the power of $3/2$, is known as skewness and is defined in Eq. (2.15). The skewness (Sk) characterises the degree of asymmetry of a distribution about the mean. The fourth order moment, non-dimensionalised by the second order moment squared, is called the flatness (Fl) and is defined in Eq. (2.16). This statistic indicates the flatness of the distribution relative to the Gaussian distribution.

$$Sk_r = \frac{1}{(\sigma^2)^{3/2}} \int_{-\infty}^{\infty} (r')^3\, p(r)dr \tag{2.15}$$

$$Fl_r = \frac{1}{(\sigma^2)^2} \int_{-\infty}^{\infty} (r')^4\, p(r)dr \tag{2.16}$$

A natural random process (such as turbulence) often exhibits a Gaussian probability distribution (v.Carmer, 2005). The standardised Gaussian distribution (defined in Eq. (2.17)) has a flatness of three and is perfectly symmetrical about the mean ($Sk = 0$). The flatness of a PDF can alternatively be described by the kurtosis, K_r, which is defined as the flatness minus three (Nikora, 2005), as stated in Eq. (2.18). Accordingly, the Gaussian distribution has a kurtosis of zero.

$$p(\hat{r}) = \frac{1}{\sqrt{2\pi}} e^{-\frac{\hat{r}}{2}} \tag{2.17}$$

$$K_r = Fl_r - 3 \tag{2.18}$$

2.3.3 Stationary, Isotropic, Homogeneous Turbulence

Theoretical analysis of turbulence often assumes that turbulence is statistically stationary, isotropic and homogeneous. The definitions of these three terms are given below (adapted from Pope, 2000):

i) Stationary: A turbulent flow field is statistically stationary if all flow statistics are invariant under a shift in time.

ii) Isotropic: Isotropic turbulence is statistically independent with respect to rotation of the coordinate system. This means that the turbulent motions have no preferred direction (i.e. rotationally symmetric). In isotropic turbulence the turbulent normal stresses are equal ($\overline{u'^2} = \overline{v'^2} = \overline{w'^2}$) and the Reynolds stress term is equal to zero ($-\overline{u'v'} = 0$).

iii) Homogeneous: A statistically homogeneous turbulent field is invariant under translation (i.e. a shift in the coordinate system). In other words, the fluctuating statistics ($p'(x_i)$ and $u_i'(x_i)$) are statistically the same at all spatial positions (i.e. there are no mean velocity or pressure gradients over the flow field).

Statistically stationary, homogeneous, isotropic turbulence is an idealised representation of turbulent flows. Such conditions rarely exist in the environment, and are difficult to reproduce in the laboratory.

Despite this, these simplifications are commonly used in order to analyse the fundamental properties of idealised turbulent flows.

2.4 A STRUCTURAL DESCRIPTION OF TURBULENCE

Section 2.3 briefly outlined the statistical methods that are commonly used to quantify and describe the random velocity and pressure signals that result from point measurements in a turbulent flow. However, turbulence is also observed to contain coherent structures that are short lived and interact over a range of length scales. This section details the methods of classifying and analysing coherent turbulent structures in order to gain a further understanding of turbulent motion.

2.4.1 The Energy Cascade

It is commonly proposed that turbulent flows contain coherent structures called eddies, as depicted in Figure 2.4. Eddies can be thought of as rotating vortices of fluid within a turbulent fluid mass that have a certain structure and life history of their own (Glickman, 2000).

In 1922, L.F. Richardson postulated that turbulent motion consists of a spectrum of such eddies that are constantly interacting over a range of different length scales. The largest scales of turbulence are supplied energy from shear in the mean flow on a scale imposed by the flow geometry (e.g. by the boundary layer depth). Smaller-scale eddies are generated from the larger eddies through the non-linear process of vortex stretching (Glickman, 2000). The smallest eddies are in turn dissipated by friction (viscosity) and their energy turned into heat. This implies that there must be an internal transfer of energy in turbulence from large scales to small scales. This exchange of energy is known as the energy cascade.

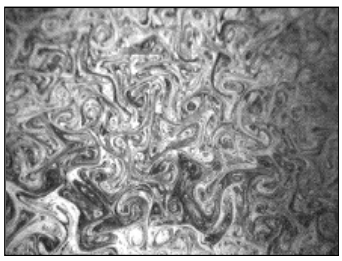

Figure 2.4 - Turbulent structures (eddies) observed in a soap film (adapted from Rutgers, 1998).

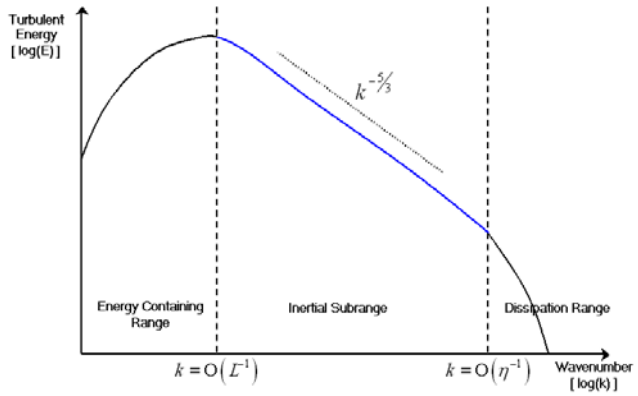

Figure 2.5 - Sketch of the theoretical energy spectrum for three-dimensional turbulence

The existence of the energy cascade is clearly demonstrated in the form of a turbulent energy spectrum (depicted in Figure 2.5). The energy spectrum describes the relative amount of kinetic energy each turbulent scale contributes to the total turbulent kinetic energy. The turbulence scale is commonly represented by a wavenumber, k, with dimensions $[1/m]$.

Figure 2.5 illustrates that the majority of energy is contained in the large-scale structures (of order L), and that energy is transferred down through the inertial subrange, to smaller scales (η) via Kolmogorov's theoretical -5/3 power-law for isotropic, three-dimensional turbulence. The methods for quantifying the length (as well as the time and velocity) scales of the large and small-scale structures are outlined in the following sections.

2.4.2 Large-Eddy Scales

Large-scale eddies are characterized by a time-scale, T_{u_i}, that approximates the turnover time of the eddy. This time-scale can be estimated using the autocorrelation function. The temporal autocorrelation function, $R_{u_i}(\tau)$, for the fluctuating velocity component is defined in Eq. (2.19), where τ denotes the temporal delay between an original, $u_i'(t)$, and a time shifted signal, $u_i'(t+\tau)$. The denominator of Eq. (2.19) normalises the autocorrelation function so that if the two signals are perfectly correlated the autocorrelation takes a value of ± 1, and if the two signals are perfectly uncorrelated, then the autocorrelation will be equal to 0. An estimate of the large-eddy time-scale is

provided from the autocorrelation function by the integral time scale, denoted T_{u_i} and defined in Eq. (2.20).

$$R_{u_i}(\tau) = \frac{\overline{u_i'(t)u_i'(t+\tau)}}{\sqrt{\overline{u_i'(t)^2}}\sqrt{\overline{u_i'(t+\tau)^2}}} = \frac{\overline{u_i'(t)u_i'(t+\tau)}}{\overline{u_i'^2}} \tag{2.19}$$

$$T_{u_i} = \int_0^\infty R_{u_i}(\tau)d\tau \tag{2.20}$$

The integral length-scale, L_{u_i}, can be estimated by using the autocorrelation function in the spatial domain (i.e. $R_{u_i}(\Delta x_i)$, where Δx_i denotes the spatial offset), in a similar manner to that outlined for the integral time-scale. However the integral length-scale can also be estimated from the integral time-scale by utilizing Taylor's hypothesis of 'frozen' turbulence.

Taylor's hypothesis assumes that the advection due to turbulent circulation is small, and therefore the advection of a field of turbulence past a fixed point can be taken to be entirely due to the mean flow (Glickman, 2000). This is known as Taylor's frozen turbulence hypothesis, and is valid provided the turbulent intensity is relatively small ($u'_{i\,rms}/\overline{U} \ll 1$), and the flow is uni-directional. If this hypothesis holds, then the integral length-scale (L_{u_i}) will be related to the integral time-scale (T_{u_i}) by the mean flow velocity, as defined in Eq. (2.21). The application of Taylor's hypothesis allows spatial scales to be deduced from a time series measured at a point in the flow.

$$L_{u_i} = T_{u_i}\overline{U} \tag{2.21}$$

Finally, as the bulk of the energy in turbulence is contained in the large-eddy scales, the velocity-scale of the large-scale structures, u_ℓ, can be scaled from the turbulent kinetic energy per unit mass (k_e) as defined in Eq. (2.22) using index notation. This equation assumes isotropic turbulence as defined in Section 2.3.3.

$$u_\ell \sim \left(2k_e/3\right)^{1/2} = \left[1/3\left(\overline{u_i'u_i'}\right)\right]^{1/2} \tag{2.22}$$

2.4.3 Small-Eddy Scales

In 1941, Kolmogorov proposed that the smallest turbulent scales are isotropic motions that are statistically independent of the large-scale turbulent structures. Furthermore the small-scale turbulence is controlled solely by viscosity, υ, and the rate at which the small turbulent scales dissipate the kinetic energy (ε_e) supplied from large-scale structures. Using dimensional analysis, Kolmogorov defined the length, velocity and time scales, defined by Eq. (2.23), Eq. (2.24) and Eq. (2.25) respectively, of the smallest structures in turbulent motion. These scales are known as the Kolmogorov micro-scales.

$$\eta = \left(\upsilon^3 / \varepsilon_e\right)^{1/4} \tag{2.23}$$

$$v_\eta = \left(\upsilon \varepsilon_e\right)^{1/4} \tag{2.24}$$

$$\tau_\eta = \left(\upsilon / \varepsilon_e\right)^{1/2} \tag{2.25}$$

It is important to note that the Kolmogorov micro-scales as well as the scales outlined in Section 2.4.2 are order-of-magnitude estimates only. Turbulent structures are chaotic and complex, exhibiting a random variety of geometries and sizes. To describe turbulent structures as a series of rotating eddies is only a simple analogy used to parameterise turbulent motion. In a sense, one can regard the coherent structures, defined in Section 2.4.2 and the Kolmogorov micro-scales, as theoretical, short-term structures, revealed by conditional averaging that provide only a limited insight into the structure of turbulent flow (Nezu & Nagakawa, 1993).

2.4.4 Structure Functions

One underlying assumption in the derivation of the Kolmogorov's micro-scales and the theoretical -5/3 power law for 3D turbulence is that the transfer rate of turbulent kinetic energy is independent of scale within the inertial subrange. This implies that energy transfer is self-similar (or scale invariant) within the inertial subrange. This assumption can be tested with the structure function.

The Kolmogorov, longitudinal structure function, $D_{Ku_in}(\Delta x)$, of order n is defined by Eq. (2.26) for the instantaneous velocity component, where Δx denotes the spatial separation between the original, $u_i(x)$ and space-shifted signal, $u_i(x+\Delta x)$. The brackets denote an averaging process (e.g. ensemble or time). The formula can also be defined for data obtained in the temporal domain, $u_i(t)$, but has been omitted for brevity. The generalised structure function is given in Eq. (2.27), which differs from the Kolmogorov structure function by taking the absolute value of the velocity difference.

$$D_{Ku_in}(\Delta x) = \left\langle \left(u_i(x+\Delta x) - u_i(x)\right)^n \right\rangle \tag{2.26}$$

$$D_{Gu_in}(\Delta x) = \left\langle \left|\left(u_i(x+\Delta x) - u_i(x)\right)\right|^n \right\rangle \tag{2.27}$$

Kolmogorov predicted that if transfer of turbulent energy is scale invariant, then for inertial range separations ($\eta \ll \Delta x \ll L$, as depicted in the turbulent energy spectrum of Figure 2.5) $D_{Ku_in}(\Delta x)$ depends only on the turbulent energy dissipation rate, ε, and the spatial separation, Δx (Pope, 2000). Following this reasoning, Eq. (2.28) is reached by dimensional analysis, where C_n is a constant relating to the order of the structure function, and $\zeta(n)$ denotes the exponent of the structure function of order n.

$$D_{Ku_in}(\Delta x) = C_n \varepsilon^{n/3} \Delta x^{\zeta(n)} \tag{2.28}$$

For self-similar energy transfer in the inertial subrange the exponent $\zeta(n) = n/3$ (Nikora & Goring, 2001). Experimental evidence confirms Kolmogorov's prediction (i.e. $\zeta(n) = n/3$) for orders of n up to approximately three. However at higher-orders the results differ from the Kolmogorov hypothesis (Pope, 2000). This is generally considered to be a result of intermittency. For a detailed discussion on intermittency, refer to Pope (2000), Leiseur (1990), Frisch (1995) and Nikora & Goring (2001).

2.5 SUMMARY

This chapter has provided a brief introduction into the phenomenon of turbulent fluid motion in Section 2.1 and introduced the governing equations of turbulence in Sections 2.2. A mathematical basis for analysing turbulent flows was then provided in Sections 2.3 and 2.4. The following chapter introduces the characteristics of turbulence confined to shallow water flows.

3.0 Background II: Shallow Flow Turbulence

3.1 INTRODUCTION

Shallow flows are defined as fluid flows in which the horizontal scale of the flow is much greater than the depth of the flow. The ratio of the horizontal scale (λ_ℓ) to the depth (H) is known as the aspect ratio and shallow flows occur when $\lambda_\ell/H >> 1$ (Jirka, 2001). Many environmental flows can be characterised as shallow, and examples include the flow in wide rivers, lakes, estuaries, and shallow coastal waters.

The present study involves an investigation into the mean flow and turbulent properties of shallow, turbulent shear flows and shallow, turbulent wakes generated in an open-channel. As a result the present chapter provides a background into open-channel hydraulics in Section 3.2. The turbulent structures present in shallow, open-channel flows are described in Section 3.3, and Section 3.4 outlines the key findings from recent research into shallow turbulent wake flows.

3.2 SHEAR FLOW THEORY

The base flows considered in the present study are shallow, steady, uniform, plane, turbulent shear flows. Steady and uniform implies that the base flow is unvarying over time and space respectively. Plane denotes that the channel exhibits no changes in bathymetry, and the flows are turbulent by ensuring that the Reynolds number (Re_H) is of magnitude 10^3 or larger. A shear flow denotes that the flow is bounded by the base of the channel and influenced by the turbulent boundary layer that forms on this boundary. The following sections describe the general hydraulic properties of such base flows.

Before proceeding, it is important to note that such idealised conditions are not typically present in environmental scale shallow flows, which are normally un-steady, non-uniform and contain significant changes in bathymetry. Shear can also be introduced at the free surface due to influence of wind, and

surface waves are typically present. Despite these facts, the imposed restrictions represent a basis from which more complicated regimes can be analysed.

3.2.1 Vertical Flow Field

The vertical velocity profile in a fully, developed, uniform open-channel flow consists of three regions; the viscous sub-layer, the inner region and the outer region as depicted in Figure 3.1. The velocity profile in the inner and outer regions have time-averaged, logarithmic distributions that can be defined respectively by the law of the wall and the velocity defect law (refer to Nezu & Nagakawa, 1993).

The shear stress in a turbulent open-channel flow varies linearly with height above the bed, and tends towards zero at the free surface (Nezu & Nagakawa, 1993). Within the viscous sub-layer the shear stress approaches a constant value and is denoted as the bed shear stress (τ_0) (Glickman, 2000). The bed shear stress for uniform flows is defined by Eq. (3.1), where ρ is the fluid density, g is gravitational acceleration, R is the hydraulic radius of the channel and S is the slope of the channel bed. A velocity scale derived from the bed shear stress is known as the shear velocity, denoted u_* and defined in Eq. (3.2). The shear velocity also represents the scale of turbulent velocity fluctuations near the bed (Glickman, 2000).

$$\tau_0 = \rho g R S \tag{3.1}$$

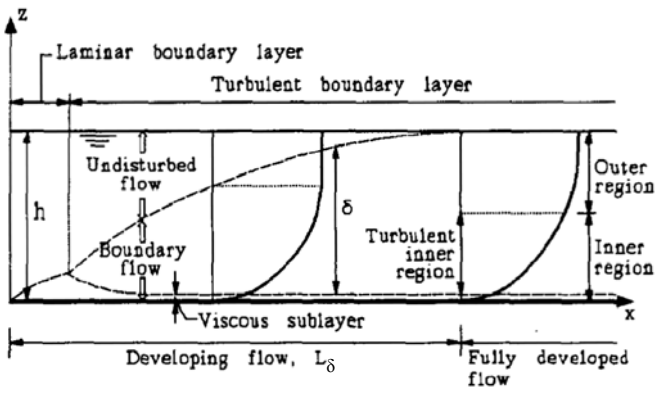

Figure 3.1 - Velocity profiles in developing and fully developed open channel flow (Kirgkov, 1997)

$$u_* = \sqrt{\frac{\tau_0}{\rho}} = \sqrt{gRS} \sim \left|\overline{u'w'}\right|^{1/2} \tag{3.2}$$

As indicated in Figure 3.1, the fully developed turbulent flow takes a certain distance (L_δ) to develop from the channel entrance. This distance depends on the development of the turbulent boundary layer. Henderson (1966) states that for a flat plate held parallel to the flow, the turbulent boundary layer thickness (δ) will grow with distance x from the leading edge of the plate, according to Eq. (3.3) (where $\mathrm{Re}_x = U_0 x/\upsilon$, and U_0 denotes the free-stream velocity). Kirkgov (1997) conducted experiments over a smooth glass plate and found that the distance from the edge of the plate to the fully developed boundary layer region (L_δ) could be approximated by Eq. (3.4), where H is the flow depth, Re_{4R} is a Reynolds number based on the hydraulic radius ($= 4U_0 R/\upsilon$), and Fr is the Froude number ($= \mathrm{U}_0/\sqrt{\mathrm{gH}}$).

$$\delta = 0.38x\left(\mathrm{Re}_x\right)^{-1/5} \tag{3.3}$$

$$L_\delta = H\left(76 - 0.0001\frac{\mathrm{Re}_{4R}}{\mathrm{Fr}}\right) \tag{3.4}$$

However both these formulas imply ideal, undisturbed entrance conditions and a smooth channel bed. Given that most channels do not satisfy these conditions, both of these formulae provide a conservative estimate of the development length of the turbulent boundary layer.

3.2.2 Vertical Distribution of Turbulent Intensity

The vertical distribution of the turbulent intensity ($u'_{irms} = \sigma_{u_i} = \sqrt{\overline{u'_i u'_i}}$) in an open channel follows the semi-empirical formula given by Eq. (3.5) (Nezu & Nagakawa, 1993). This equation is only valid outside of the viscous sub-layer (i.e. $0.15 \le z/H \le 0.9$) in a plane, smooth, open-channel flow. The turbulent intensity has been normalised by the shear velocity of the channel and C_{u_i} represents a constant relating to the three velocity components ($C_u = 2.3$, $C_v = 1.63$ and $C_w = 1.27$). This formula has been verified experimentally with LDV for open channel flows over a wide range of Reynolds and Froude numbers.

$$\frac{u'_{irms}}{u_*} = C_{u_i} e^{(-z/H)} \tag{3.5}$$

Eq. (3.5) implies that the production of turbulent energy reaches a maximum near the bed of the channel after which exponential decay is observed with increasing height above the channel bed. The free surface acts to damp turbulent intensity components (especially the vertical component), and Eq. (3.5) has not been experimentally verified at the free surface (i.e. at $z/H = 1$) (Nezu & Nagakwa, 1993).

3.2.3 Horizontal Flow Field

Provided that the base flow in an open-channel is plane, steady and remote from the influence of sidewalls, it is expected that the time-averaged transverse velocity profile will be uniform (i.e. $\partial\overline{U}/\partial y = 0$). Furthermore, if the flow is fully developed then it is assumed that the velocity profile will be independent of downstream distance (i.e. $\partial\overline{U}/\partial x = 0$).

To summarise, Section 3.2 has outlined the general hydraulic properties of plane, uniform, turbulent open-channel flows. The vertical velocity gradient between the base of the channel and the free surface results in a shear stress distribution that varies with a maximum value at the channel base, and a minimum value at the free-surface. A similar distribution is observed for the turbulent intensity components, as turbulent energy is produced at the base of the channel and suppressed by the free surface. Finally, if the channel is straight (plane), then the horizontal velocity profiles are expected to be homogeneous. These flow conditions are expected to prevail in the shallow, channel flows considered in the present study. The following section describes the turbulent structures present in shallow, shear flows.

3.3 TURBULENT STRUCUTRES IN SHALLOW SHEAR FLOWS

As opposed to free shear flows where there are no boundaries influencing fluid motion (e.g. ocean outfall discharges and smoke plumes), shallow flows are confined in the vertical direction. For an open-channel flow, a solid wall confines the base of the flow and a free-surface confines the vertical extent of the flow (v.Carmer, 2005). Such boundaries influence the formation and propagation of turbulent structures in shallow flows. The following sections outline the turbulent structures that have been identified from research into shallow, open-channel flows.

3.3.1 Structures Generated by Vertical Shear

3.3.1.1 3D Turbulence

At the base of a shallow, turbulent, shear flow vertically sheared three-dimensional structures are produced from instabilities in the turbulent boundary layer. Instabilities arise from burst and sweep phenomena (refer to Nezu & Nagakawa, 1993), where 3D eddies are ejected from the relatively low speed fluid close to the channel bed and lifted towards the free surface. 3D structures have been found experimentally to follow Kolmogorov's –5/3 power law of energy transfer from large-scale to small-scale structures (Nezu and Nagakawa, 1993). The size of 3D turbulent structures are restricted to the flow depth, as the free surface of the flow restricts further vertical propagation.

3.3.1.2 2D Structures at the Free-Surface

Kumar, et al (1998) identified the presence of 2D spiral eddies at the free-surface of an open-channel flow (provided that the free-surface is smooth and undisturbed). These are secondary structures that form at the edges of up-welling 3D eddies, as close to the free surface interface, turbulent normal stresses perpendicular to the boundary ($w'w'$) are suppressed and, due to

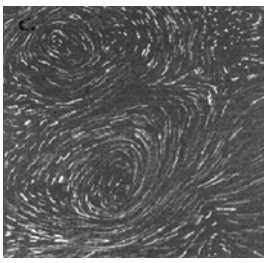

Figure 3.2 - Streak-lines (visualised by hollow glass "microballoons") of spiral eddies at the free surface of a turbulent, shallow channel flow (Re=8800, H=4.2cm). The area covered by the picture is 6.7cm x 4.5cm. (Kumar, et al, 1998).

conservation of momentum, turbulent kinetic energy from three-dimensional structures is redistributed into the tangential normal stresses (v.Carmer, 2005). As a result spiral eddies are predominantly 2D structures that propagate in the horizontal domain at the free-surface of the flow. Furthermore, Kumar, et al (1998) identified that spiral eddies can exhibit length scales greater than the flow depth, and have the potential to adhere to the inverse energy cascade, which is outlined in the following section.

3.3.2 Structures Generated by Lateral Shear

If a mechanism to produce lateral shear is introduced into the flow (for example by an obstacle such as a bridge pier), eddies with scales much larger than the depth, can develop in the horizontal plane. The shallowness of the water prevents these eddies from being stretched in the vertical dimension and forces the large eddies into a quasi two-dimensional motion (Uijttewaal and Booij, 2000). In contrast to the vortex stretching mechanisms of 3D turbulence, 2D eddies, with the same sense of rotation, can merge via vortex pairing and therefore grow in size. Thus for 2D turbulence, the spectral energy can be transferred from small-scale structures to large-scale structures via an inverse energy cascade (v.Carmer, 2005).

For theoretically 2D turbulence, energy is transferred from small to large scales following a -5/3 power law, whilst enstrophy (a measure of local rotation in a fluid flow) is transferred from large to small scales via a -3 power law (Danilov & Gurarie, 2000). This dual transfer is illustrated in the energy spectra, $E(k)$, of Figure 3.3, where ε_e and $\acute{\eta}$ represents the dissipation rates of energy and enstrophy respectively. The symbol, k_f, represents the forcing wavenumber.

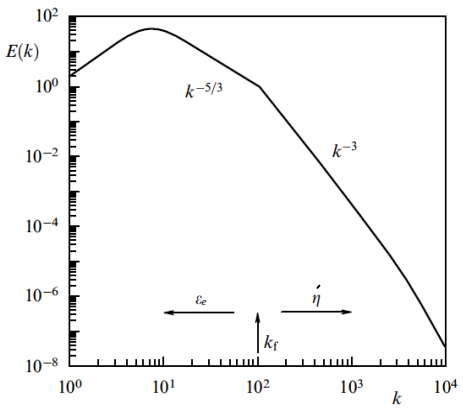

Figure 3.3 - Conceptual sketch of the theoretical energy spectrum for 2D turbulence. (Danilov & Gurarie, 2000).

3.3.2.1 Forcing Mechanisms

Jirka (2001) defines the large-scale turbulent structures, generated by lateral shear as two-dimensional coherent structures (2DCS). Furthermore 2DCS are generated by, three main mechanisms (Type A, B and C), which are outlined below (adapted from Jirka, 2001).

[TYPE A] Topographical Forcing: Topographic features (islands, jetties, groynes, etc) lead to flow separation and return velocities in the lee of the feature. As a result vortices are shed from the topographic feature, and evolve laterally to form large-scale quasi-2D turbulent structures. A striking example of this is illustrated in Figure 3.4a. In this figure the oil tanker, Argo Merchant, is stranded on a stretch of shallow water off Nantucket, Massachusetts, USA. The wake generated from the flow around the tanker has vortices of the order of $600m$ in diameter, which are clearly much greater than the approximately $15m$ depth of the flow (Balachandar, et al, 2000).

[TYPE B] Internal Transverse Shear Instabilities: Velocity variations in the transverse direction provide a mechanism for the growth of 2DCS. Such velocity variations can arise due to the presence of a turbulent jet (e.g. discharge from a wastewater pipe) or density anomalies in the flow domain. Also topographical changes such as changes in

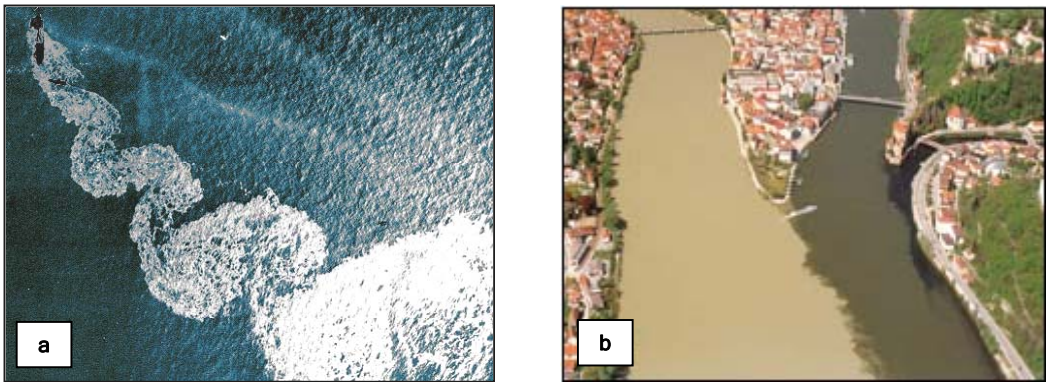

Figure 3.4 - **(a)** 2DCS are generated by topographical forcing due to the stranding of oil tanker, Argo Merchant, in shallow costal waters off Nantucket, Massachusetts (Van Dyke, 1982) **(b)** 2DCS generated by a transverse shear layer, at the confluence of the rivers Danube and Inn, located in the Bavarian city of Passau (v.Carmer, 2005).

roughness or bed height can provide the velocity variation needed to form 2DCS. An example of 2DCS generated by transverse shear is depicted in Figure 3.4b. In this figure, the confluence of two rivers (one coloured light brown due to sediment loading) produces a transverse shear layer and 2DCS are observed to grow with distance downstream.

[TYPE C] Secondary Instabilities of Base Flow: This is the weakest type of generation mechanism and research into this type of forcing is limited. This generation occurs when the vertically sheared 3D turbulent structures undergo instabilities caused from slight imbalances in the flow, localized roughness zones or underwater obstacles. The instability in the 3D structures leads ultimately to the formation 2DCS.

The present study firstly generates shallow turbulent shear flows in the laboratory with the aim of identifying the hydraulic and turbulent composition at the surface of such flows. Secondly a mechanism to produce 2DCS is introduced into the shallow turbulent shear flows in the form of an isolated single cylinder (i.e. a TYPE A forcing mechanism). The type of flow that results from the introduction of the cylinder into the flow is known as a turbulent wake flow, and Section 3.4 provides a background into this class of flow.

3.4 SHALLOW TURBULENT WAKES

The wakes considered in the present study are examples of shallow, turbulent plane wakes, where a uniform stream flows around a cylinder, which is aligned with the vertical axis (Pope, 2000). Before introducing the characteristics of shallow turbulent wakes in Sections 3.4.2 and 3.4.3, a review of the fundamental properties of unbounded (deep) turbulent, plane wakes is presented in Section 3.4.1.

3.4.1 Aspects of Turbulent, Unbounded Wakes

When a fluid flows past a circular cylinder, a region of disturbed flow is always formed around the cylinder (Zdravkovich, 1997). Figure 3.5 shows the division of the disturbed flow regions. Region (i) is a narrow region of retarded flow, (ii) denotes the region where the two boundary layers attach to the surface of the cylinder. Region (iii) depicts two sidewise regions of displaced and accelerated flow, and region (iv) is one wide region of separated flow called the wake (Zdravkovich, 1997). The wake region is characterised by vortex shedding processes. For a turbulent unbounded, plane wake, the spanwise length scale of vortices is roughly proportional to the width of the wake and the vortices exhibit strong 3D components (Lloyd & Stansby, 1997).

Zdravkovich (1997) describes a wide range of wake behaviour for unbounded flow around a smooth circular cylinder. The type of wake that forms is classified by the Reynolds number based on the cylinder diameter ($\mathrm{Re}_D = U_o D/\upsilon$, where U_o is the free stream velocity and D denotes the cylinder diameter). For the Reynolds numbers in the range $300 \lesssim \mathrm{Re}_D \lesssim 200000$ a TrSL (transition-in-shear-layers) regime dominates (Zdravkovich, 1997). This flow state is characterised by the formation of eddies in the shear layer as depicted in Figure 3.6a. In this figure the boundary layers (depicted as region (ii) in Figure 3.5) transform from laminar to turbulent some distance away from the lee of the circular cylinder and transition waves appear as undulations in the free shear layers. With increasing

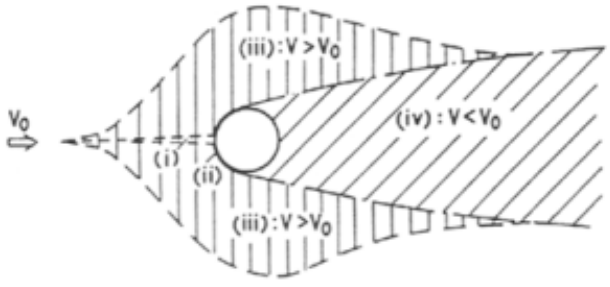

Figure 3.5 - Regions of disturbed flow around a circular cylinder (Zdrakovich, 1997)

Re_D (as depicted in Figure 3.6b), the transition waves roll up as discrete eddies and are alternately shed and advected downstream as a von Karman vortex street. The periodic shedding of vortices is characterised by a nearly constant Strouhal number ($St = fD/U_o$) of ≈ 0.2 over the range $1000 \lesssim \mathrm{Re}_D \lesssim 100000$ (Zdravkovich, 1997). It should also be noted that disturbances such as roughness elements on the cylinder and background turbulence in the approaching flow can trigger turbulence in the shear layers at Reynolds numbers much less than those illustrated in Figure 3.6.

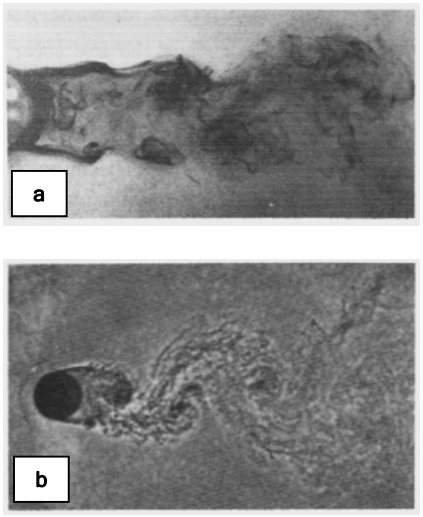

Figure 3.6 – Transition to turbulence in the free shear layers that develop downstream of a cylinder in an unbounded flow with a Reynolds number of **(a)** Re_D=2000 **(b)** Re_D =110000 (Zdrakovich, 1997)

The near wake region for the TrSL regime is classified as the region over which eddy formation occurs (Zdravkovich, 1997). This region is designated as the longitudinal distance (L_f) from the midpoint of the cylinder to the location of maximum streamwise fluctuation (u'_{rms}) in the wake. Alternatively L_f is defined as the longitudinal distance from the midpoint of the cylinder to the point at which the time-averaged streamwise velocity ($\overline{U}$) is zero. The length of L_f decreases with increasing Re_D in the TrSL regime.

The far wake of an unbounded plane wake flow has been found experimentally to be self-preserving in terms of momentum conservation (refer to Pope, 2000). Additionally unbounded plane wakes reveal self-similar behaviour in the far-field (i.e. when non-dimensionalied by local characteristic scales, the transverse velocity profile is independent of downstream position) (v.Carmer, 2005).

3.4.2 Shallow Wake Classification

Turbulent wakes in shallow flows differ from unbounded wakes due to the confinement of the flow in the vertical direction. The effect of vertical shear at the channel bed generates 3D turbulence, which exhibits length scales of the order of the flow depth. Secondly, due to the presence of a bluff body, large-scale structures are generated as a result of lateral shear. Due to the confinement imposed by the shallow water depth, the large-scale structures assume quasi-2D characteristics (i.e. TYPE A forcing of 2DCS as detailed in Section 3.3.2.1).

The growth of the 2DCS in shallow flows is maintained on one hand by transverse shear, entrainment and vortex pairing (Jirka, 2001), whilst on the other hand energy is extracted from the 2DCS by the stabilising effect of bed friction. A non-dimensional parameter which characterises the stabilising effect of bed friction relative to the destabilising influence of transverse shear is given by the wake stability number, S_{ws}, defined in Eq. (3.6), where c_f is the skin friction coefficient, D is the cylinder diameter and H denotes the flow depth.

$$S_{ws} = c_f \frac{D}{H} \tag{3.6}$$

Chen & Jirka (1995) used the wake stability number in an extensive experimental study to classify the stability of shallow turbulent wakes induced by bluff bodies (v.Carmer, 2005). They concluded that three distinct wake classes form in the lee of bluff bodies, which can be predicted by the wake stability number. These three wakes are illustrated in Figure 3.7 and denoted von Karman vortex-street (VS), unsteady bubble (UB) and steady bubble (SB) wakes.

Wake Type	Vortex Street	Unsteady Bubble	Steady Bubble
Wake-Stability Number Range	$S_{ws} \lesssim 0.2$	$0.2 \lesssim S_{ws} \lesssim 0.5$	$S_{ws} \gtrsim 0.5$
Image of Wake	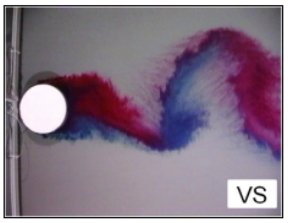	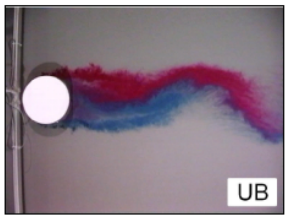	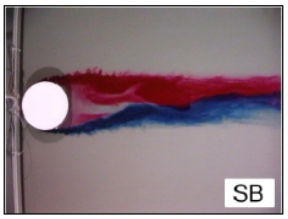

Figure 3.7 - Wake-stability parameter ranges for vortex-street, unsteady-bubble and steady-bubble type wakes generated from flow around a circular cylinder in a shallow flow (adapted from v.Carmer & Jirka 2001).

Furthermore, Chen & Jirka (1995) found that for large distances downstream (x/H) of the bluff body, the wakes "stabilised". This meant that as the mechanisms for growth and maintenance of large-scale structures became suppressed by bed friction, the wake collapsed into a more ordered flow that predominantly contained vertically sheared 3D turbulence.

Due to the finite extent of the experimental flume used in the present study, only vortex street type shallow wakes could be generated in the laboratory. As a result Section 3.4.3 focuses on key findings from recent research into shallow VS type wakes.

3.4.3 Characteristics of Shallow VS Wakes

As a continuation of the work by Chen & Jirka (1995), v.Carmer (2005) used a combined LDV-LIF, and PIV techniques to study momentum and mass transfer in shallow turbulent wake flows generated by circular cylinders. In this study measurements of turbulent velocities were evaluated on the centreline of VS, UB and SB wakes using LDV at a depth of $z/H = 2/3$, for several locations downstream. The power spectral densities for the transverse velocity component are displayed in Figure 3.8.

Figure 3.8 firstly shows that regardless of the stability class, all shallow turbulent wakes display an energy cascade that follows the Kolmogorov –5/3 law, indicating the existence of energy dissipation

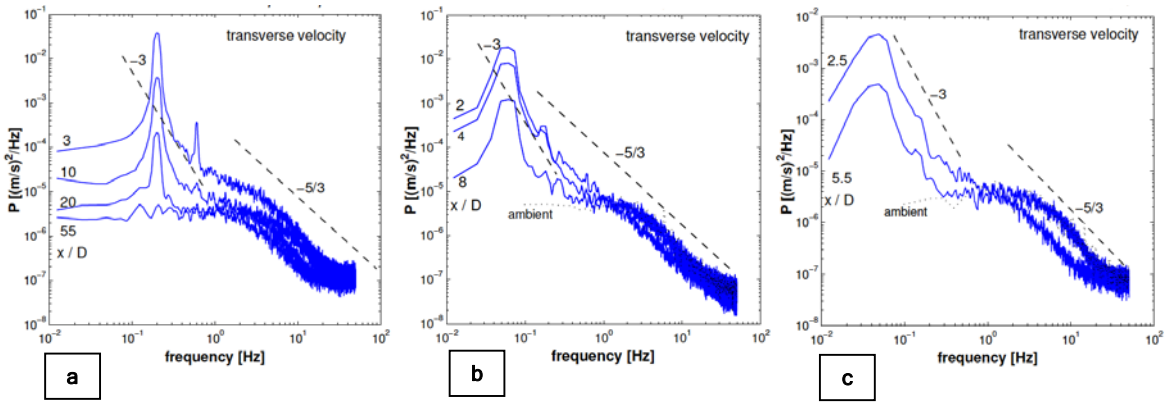

Figure 3.8 - 1D PSD estimates of the transverse velocity evaluated using LDV (sampling frequency = 100Hz) for **(a)** vortex street (Re_H=2336; H=18mm; D=125mm) **(b)** unsteady bubble (Re_H=2080; H=17mm; D=500mm) and **(c)** steady bubble (Re_H=3692; H=24.8mm; D=1120mm) type wakes. Data has been obtained at selected downstream positions along the centrelines of the wakes at a flow depth of z/H=2/3 (v.Carmer, 2005).

via an inertial subrange (v.Carmer, 2005). Secondly the peaks of each spectrum represent forcing of large-scale coherent motion at a frequency specified by the non-dimensional Strouhal number ($St = fD/U_a$), which characterises the periodic shedding process of the wake. Thirdly, the existence of an –3 cascade is indicated which characterises the transfer of enstrophy from large-scale 2D turbulence to small-scale turbulent structures (refer to Figure 3.3). However an inverse energy cascade is absent for each shallow wake flow.

For the case of a VS wake, the absence of an inverse energy cascade is attributed to the organisation of the 2DCS in a highly organised vortex-street like arrangement (v.Carmer, 2005) as illustrated in Figure 3.9. In the VS type wakes, neighbouring vortices with the same sense of rotation are separated by regions of ambient fluid entrainment, effectively preventing any merging of vortices.

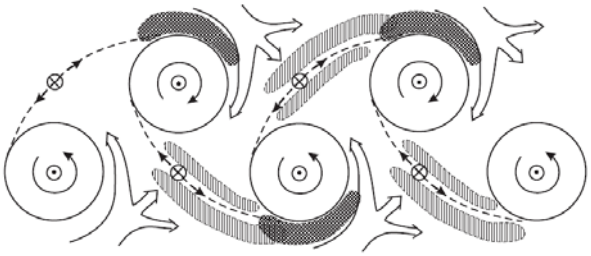

Figure 3.9 - A conceptual sketch of a vortex street-like shallow wake flow with predominant 2DCS. The vortex cores are denoted by ⊙ symbols, saddle points of the streamlines are denoted by ⊗ symbols. Dashed lines indicate the braids connecting counter-rotating 2DCS across the wake. Double-lined arrows show the entrainment of fresh ambient fluid into the wake. Vertically hatched areas on both sides of the braids indicate regions production of TKE. Crosshatched areas indicate regions of intense mass mixing. (v.Carmer, 2005).

v.Carmer (2005) also investigated the time-averaged transverse velocity distribution across the wake. The velocity deficit (U^+) and wake half-width (y^+) were used to normalise the respective velocity and transverse scales. The velocity deficit is defined in Eq. (3.7), where u is the instantaneous velocity component, and U_a and U_c denote the respective ambient velocity (outside the wake) and centreline velocity. The wake half-width is defined in Eq. (3.8), where $y_{0.5}$ is the cross-sectional distance from the centreline, at which the velocity component reaches half the fraction of the centreline velocity (v.Carmer, 2005).

$$U^+ = \frac{u - U_a}{U_c - U_a} \tag{3.7}$$

$$y^+ = y / y_{0.5} \tag{3.8}$$

The transverse distribution of velocity deficit was found to be largely self-similar and Gaussian over the full extent of the wake. However for $x/D \lesssim 2.5$, the velocity deficit deviated from self-similarity. This result was also verified by Balachandar & Tachie (2001).

The longitudinal development of a shallow wake flow was also investigated by v.Camer (2005). A shallow wake flow was categorised into the three regions. The wake *near-field* was defined as an unstable region over which large-scale vortical structures were formed, and the organised VS wake developed. This region closely resembled flow in an unbounded plane wake. The *intermediate-field* is dominated by counter-rotating streets of 2DCS, which propagate above and below the cylinder centreline. Finally, the wake *far-field* is dominated by random, vertically sheared 3D turbulence, which acts to disintegrate the 2DCS. v.Carmer (2005) suggests that the transition between the near-field and intermediate-field occurs at $x/\ell_M \approx 10$ to 20, where ℓ_M is the integral wake length scale defined in Eq. (3.9).

$$\ell_M = (\sqrt{\pi/8} HD)^{1/2} \tag{3.9}$$

Akilli & Rockwell (2002) used high resolution PIV to investigate the processes occurring in the near wake region. They presented streamline topology, mean velocity, vorticity and turbulent stress fields at near-bed ($z/H = 0.06$), mid-plane ($z/H = 0.5$) and near-surface ($z/H = 0.96$) elevations for $x/D < 1$. Their key finding was that the vortex formation process in the re-circulation region was highly three-dimensional, (as indicated in Figure 3.10).

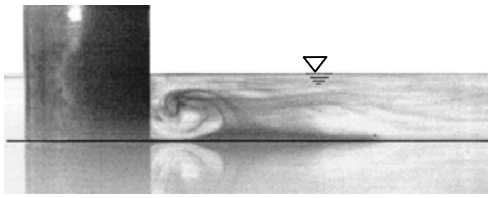

Figure 3.10 - Three dimensional vortex formation in the near wake region, as visualised by dye injection (Akilli & Rockwell, 2002).

3.5 SUMMARY

This chapter has provided a brief introduction into the characteristics of shallow turbulent shear flows and shallow turbulent wake flows. Section 3.2 and 3.3 outlined the hydraulic properties and turbulent structures present in shallow shear flows, while Section 3.4 focused on aspects shallow turbulent wake flows.

The present study will investigate shallow, shear flows and shallow vortex-street wake flows using PTV. Mean velocity, turbulent stress, probability density function (PDF), autocorrelation and power spectral density (PSD) fields are endeavoured to be resolved in order to provide further insight into the characteristics of shallow, shear flows and shallow, turbulent wake flows. The following chapter describes the methods used to generate such flows in the laboratory as well as describing the systems used to gather experimental data.

4.0 Methodology

This chapter describes laboratory experiments that have been performed to investigate the mean flow and turbulent properties of shallow flows using particle-tracking velocimetry (PTV). Section 4.1 outlines the objectives of the laboratory program, and Section 4.2 describes the flume used to produce shallow, turbulent flows. Section 4.3 provides a detailed overview of the PTV system used in the present study. Finally, Section 4.4 lists the experimental procedure used to gather data.

4.1 EXPERIMENTAL OBJECTIVES

The experimental aim of the present study was to investigate the turbulent properties of shallow flows, generated in the laboratory. This was achieved by using a PTV system to analyse the two shallow flow regimes outlined below:

(i) Shallow Turbulent Shear Flow Regime: An investigation into the mean flow and turbulent properties of plane, uniform, shallow turbulent shear flows.

(ii) Shallow Turbulent Wake Flow Regime: Large-scale lateral instabilities were introduced into the vertically sheared base flows considered in (i), by introducing a single, isolated circular cylinder into the flow. The mean flow and turbulent properties were subsequently analysed.

The proposed research will firstly provide information on the limitations and abilities of a PTV system, using surface-tracer particles, to provide mean flow and turbulent data at the surface of shallow flows. Secondly the current investigation endeavours to improve the current understanding of the turbulent properties of shallow flows.

4.2 EXPERIMENTAL FLUME

A flume designed and built by NIWA (National Institute of Water and Atmospheric Research) was used throughout the experimentation. This flume is depicted in Figure 4.1, and was stationed in the Fluid Mechanics Laboratory at the University of Canterbury. The flume was designed specifically to model shallow flows over variable bed slopes, and had overall dimensions of 2.675*m* (length) x 1.170*m* (width) x 0.185*m* (channel height). The important characteristics of the flume are detailed in the following sections.

4.2.1 Channel Bed

The flume channel initially consisted of a stainless steel surface. A false bed was overlaid on top of the existing surface in order to raise the bed of the flume to coincide with the leading edge of the inlet basin. The false bed consisted of a white Foamboard base (10*mm* thick). The bed had a smooth, impermeable surface that was spray painted black in order to contrast with the white particles used during PTV visualisation. The tolerance of the flume bed was evaluated with a survey level, and found to depart by approximately ±0.5*mm* from the horizontal. The overall dimensions of the flume bed, with the false base in position, was 1970*mm* (length) x 974*mm* (width).

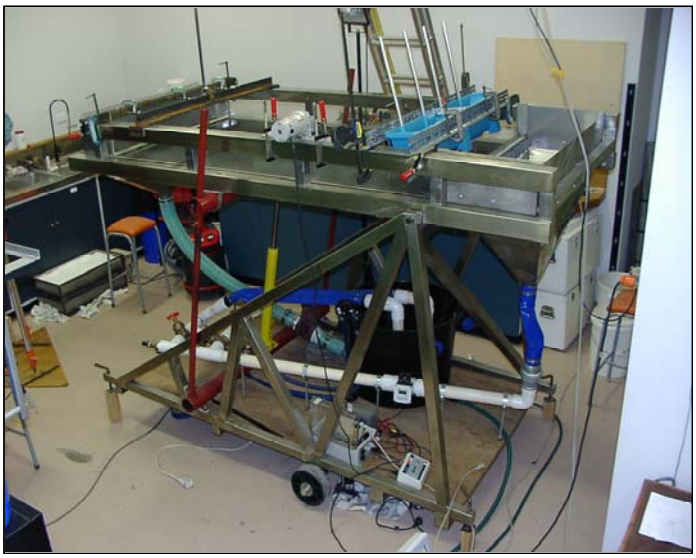

Figure 4.1 - The shallow flow flume situated in the Fluid Mechanics Laboratory at the University of Canterbury.

The channel bed had the ability to be tilted over slopes ranging from zero to ten degrees by adjusting a hydraulic jack, situated underneath the channel bed. Fine adjustment of the bed slope was possible by manipulation of four screw jacks attached to each corner of the flume. Bed slopes were calculated by taking level measurements at locations on the channel bed using a survey level and staff (refer to Appendix A for a description of this procedure). The measurement accuracy of the survey level was approximately $\pm 0.5mm$ over the elevation difference between the inlet and outlet of the flume.

4.2.2 Flow Control

The flume operated as a self-reticulating circuit (refer to Figure 4.2). Two Grundfos^{TM} KP350-A1 pumps were situated in a 135 litre polythene tank underneath the channel bed. Each pump delivered water from the polythene tank into the inlet basin. The fluid flowed across the bed of the flume, spilled across an overfall weir at the downstream end of the flume, and re-circulated back into the polythene tank.

The two pumps operated independently, and the flow rate was controlled with valves located on the outlet pipes. Each pump had a maximum output of approximately 3.15 *l/s*. This gave the ability to vary the flow rate up to a maximum flow of approximately 6.30 *l/s*. Two back-feeder pipes were also installed in the system. Opening the back-feeder valves allowed water in the outlet pipes bypass to the inlet basin, and flow directly back into the polythene tank. This back-feeding system enabled fine adjustment of the flow rate.

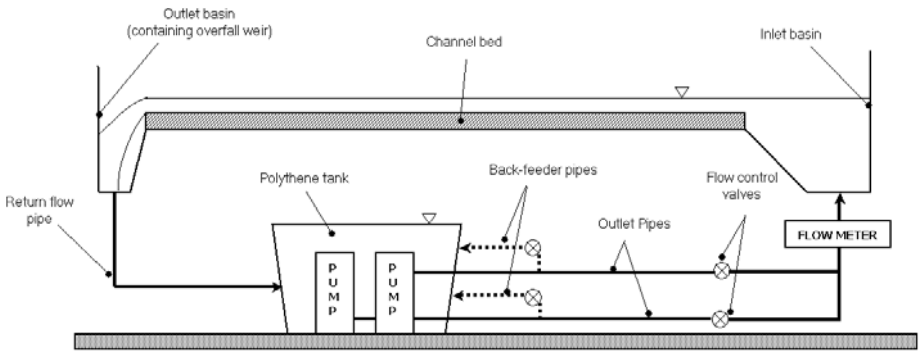

Figure 4.2 - Elevation schematic of self-reticulating flow circuit

An ABB^{TM} FXL5000 electromagnetic flow meter was attached to the pipe that fed the inlet basin (refer to Figure 4.2). This flow meter was calibrated with an existing electromagnetic flow meter and calibration pit at the Fluid Mechanics Laboratory at the University of Canterbury. The ABB^{TM} FXL5000 was found to differ by $\pm 1\%$ with the other two flow recording devices. A data logger (Starlogger^{TM} 6004c) was connected to the flow meter in order to record the flow rate at five-second intervals during experimentation. The data from the logger was downloaded and analysed with a spreadsheet.

Flow depths were obtained with an adjustable point gauge. The point gauge could be moved in both the longitudinal and transverse directions so that depth measurements could be obtained at any point over the working area of the flume. The error associated with the point gauge was $\pm 0.25mm$.

4.2.3 Inlet and Outlet Conditions

The inlet to the flume contained a porous baffle and honeycomb flow stabiliser that covered the inlet pipe (refer to Figure 4.3). These diffusers were employed to remove a non-uniform transverse velocity distribution as outlined in Appendix B and summarised in Figure 4.4a. The implementation of honeycomb flow stabilisers and porous baffle contributed to predominantly homogeneous flow conditions. However small unavoidable imperfections in the channel bed and discharge meant that the transverse velocity profile departed from uniform conditions by approximately $\pm 2.5\%$. A strip of flow

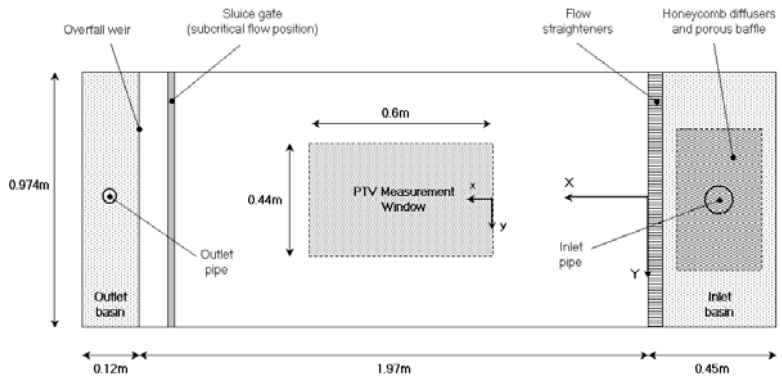

Figure 4.3 - Plan schematic of the flume bed

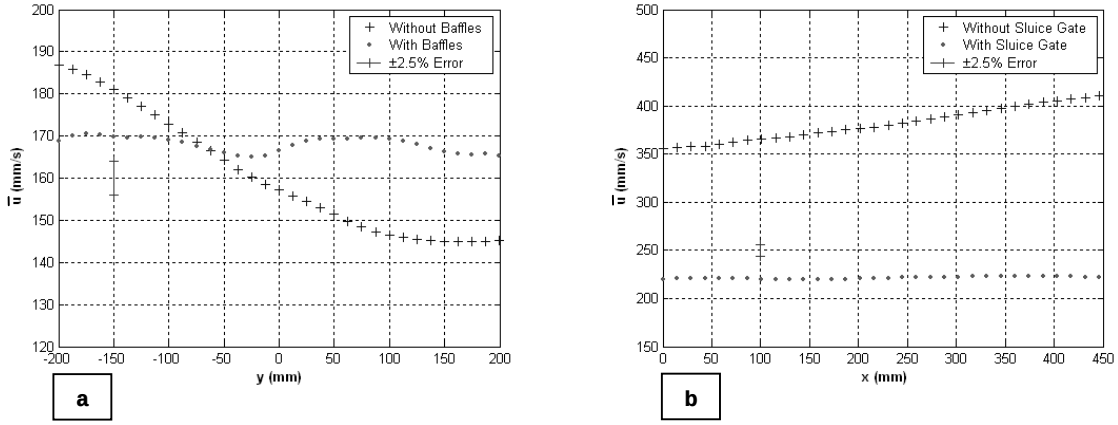

Figure 4.4 - **(a)** Effect of baffles on the time-averaged, transverse surface-velocity profile (i.e. $\bar{U}(y)$ for x=300mm) evaluated using PTV (Run#1D) **(b)** Effect of sluice gate on time-averaged, longitudinal surface velocity profile (i.e. $\bar{U}(x)$ for y=0mm) evaluated using PTV (*with sluice gate:* Run#6A; *without sluice gate:* Run#6B). Flow parameters for each run are outlined in Appendix B.

straighteners, which spanned the channel width, were also present to remove any secondary currents resulting from the inlet pipe.

The outlet of the flume consisted of an overfall weir, which spilled into the outlet basin. However given the limited longitudinal extent of the flume, this outlet condition was not sufficient to establish longitudinal, uniform flow conditions (refer to Appendix B and Figure 4.4b). As a result, a Perspex sluice gate was placed $50mm$ downstream from the flume inlet for supercritical conditions, and $110mm$ upstream of the flume outlet for sub-critical conditions. Figure 4.4b displays that a predominantly uniform longitudinal velocity profile was achieved with the implementation of the sluice gate.

4.2.4 Flow Visualisation

Food dye was injected into the flows to obtain a qualitative understanding of the flow structure. For flow visualisation experimentation a white laminated sheet was affixed to the channel bed. Food dye was then injected into the flow via an intravenous system. This system consisted of a syringe attached by plastic tubing to a flask containing dye. A valve on the plastic tubing allowed the seepage rate of the dye to be controlled. The syringe was attached to a point gauge, so that the dye could be injected at variable depths within the flow.

4.3 PARTICLE TRACKING VELOCIMETRY SYSTEM

With the advent of digital video technology, velocities of fluid flows are now generally measured using particle image velocimetry (PIV) or particle tracking velocimetry (PTV). As opposed to previous techniques (LDV and hot-wire anemometry), which provide velocity information only at a fixed point in a flow, PIV and PTV both provide full spatial and temporal resolution of velocities in a flow (Ballard, 2004).

The present investigation used a PTV system to measure velocity fields at the surface of the flow. The physical setup of the system was based on a PIV system used by Weitbrecht, et al (2002). The system is depicted schematically in Figure 4.5, and consisted of a particle distribution system that seeded the surface of the flow with polypropylene particles (2-3*mm* in diameter). The particle movement was recorded with a digital video camera and velocity fields were generated from the digital images using PTV software designed by Nokes (2005b). A detailed explanation of the PTV system is outlined in the following sections.

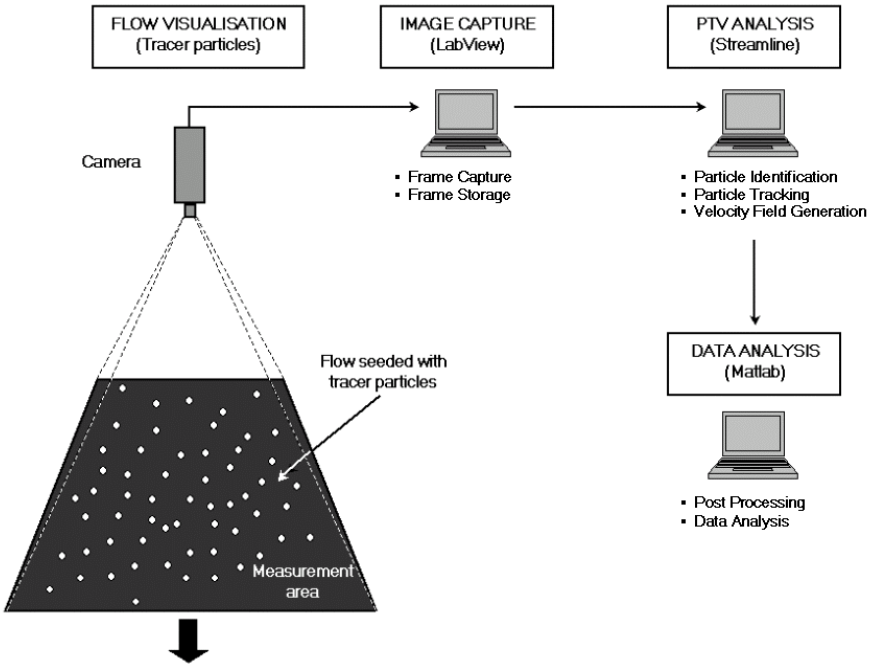

Figure 4.5 - Schematic of PTV system (adapted from Weitbrecht, et al, 2002)

4.3.1 Flow Visualization & Image Capture

PTV is based on the principal of capturing digital video images of a flow seeded with tracer particles and from that video record, extracting quantitative information about the flow field (Nokes, 2005b). The following sections focus on the components of the system used to visualise the flow as well as the equipment used to capture digital images of the flow.

4.3.1.1 Tracer Particles

Particle selection is paramount to a successful PTV system. Particles ideally need to be constructed from an impermeable, robust material so that they do not change size by absorbing water or by breaking up within the flow. Particles also need to be large enough for the camera to resolve, but small enough so that they do not have significant inertial forces that prevent them from accurately responding to turbulent structures within the flow.

Previous PTV experimentation at the University of Canterbury has used Pliolite resin as a tracer material. Pliolite resin has a density of $1.03 g/cm^3$ and can be sieved to a diameter ranging between $80 \mu m$ to ~$1.2 mm$. This tracer floats in suspension within a flow, and a white light or laser sheet, is used to illuminate the particles. However initial testing with Pliolite particles in the self-reticulating flume found that these particles were difficult to resolve at the velocities (0.16 - 1.50m/s) and depths (5 - 20mm) present within the flume. Additionally these particles did not re-circulate through the system, but agglomerated at the surface of the downstream reservoir. These factors contributed to the decision to investigate seeding the flow with water surface tracers.

The main considerations for water-surface tracers are their size, and tendency to agglomerate. Agglomeration tends to affect all floating particles as a result of surface tension on the water surface. This agglomeration effect is undesirable, as the force of attraction between particles can potentially overcome forces resulting from the flow itself. As a result particles need to have a low tendency to agglomerate on the water surface.

Weitbrecht, et al (2002) tested a variety of particles for use in a PIV system designed to obtain surface velocity fields (refer to Table 4.1). The results published in Table 4.1 are consistent with testing carried out in the present study on polystyrene, polypropylene and polyethylene surface tracers. Polystyrene particles were significantly influenced by airflow above the water surface. Polyethylene particles exhibited significant agglomeration, where as polypropylene particles showed relatively little tendency to agglomerate, and could be easily resolved with the camera. As a result of these findings polypropylene (PP) particles were used for all subsequent experimentation. The PP particles were white, roughly cylindrical in shape, 2-3*mm* in diameter and had a density of $0.9 g/cm^3$.

PTV tracks particles embedded within the fluid and therefore determines particle velocities, not fluid velocities. As a result, the dynamic properties of particles need to be evaluated in order to determine whether they accurately sample the fluid velocity. Raffel, et al (1998) derived a time scale, τ_s, that characterises the time lag for a particle to attain velocity equilibrium in a continuously accelerating fluid. This scale is defined in Eq. (4.1), where d_p denotes the particle diameter, ρ_p the particle density, ρ_f the fluid density and υ the kinematic viscosity of the fluid. Applying Eq. (4.1) to the PP particles used in the present study yields a time scale of 0.31 seconds for a particle diameter of 2.5*mm*. However Eq. (4.1) has been derived from Stokes law, which assumes a spherical particle in a viscous fluid at very low Reynolds numbers, and so provides a conservative estimate of the tendency of

Table 4.1 - Properties of different tracer materials and their applicability to water surface PIV/PTV measurements (Weitbrecht, et al, 2002)

	(1)	(2)	(3)	(4)	(5)	(6)
material	Polystyrene	coal	wood	expanded clay	Polyethylene	Polypropylene
form	sphere	die	sphere	sphere	cylinder	cylinder
diameter [mm]	2	1-5	4	1-2	2-3	2-3
density [g/cm^3]	0.04	0.50	0.50	0.73	0.90	0.90
resistance to air flow	-	+	+	+	+	+
avoidance of agglomeration	-	-	o	-	-	o
price	o	+	-	+	+	+
durability	+	o	-	+	+	+

-poor, o acceptable, + good

particles to obtain velocity equilibrium. Indeed, Brennen (2005) indicates that the response time of a particle in a turbulent flow can be up to five times less than the particle response time in a low Reynolds number flow.

$$\tau_s = d_p{}^2 \frac{\rho_p}{18\upsilon\rho_f} \tag{4.1}$$

In order to provide a more robust estimate of the inertial response of PP particles to accelerations in the flow, particles were placed, with negligible initial momentum, into a shallow, turbulent, uniform, shear flow. Figure 4.6 depicts the ensemble average of the streamwise Langrangian velocity (u) of five particles tracked at 12*Hz* over 420*mm*. This figure indicates that as a particle is placed in the flow ($t = 0$) it is instantly accelerated to within 2.5% of the ambient surface velocity, U_s. This implies that the response time of the PP particles cannot be resolved at a sampling rate of $0.08333s \equiv 12Hz$.

Weitbrecht (2004) states that flow structures can be adequately resolved by PP particles, if their length scale is at least five times bigger than the particle diameter. Particles used in the present study were approximately 2-3*mm* in diameter and so flow structures in the order of 15*mm* can be expected to be resolved.

4.3.1.2 Particle Dispenser

A particle dispenser was used to ensure the flow was seeded with a relatively homogeneous distribution of particles as well as to provide a sufficient number of particles per frame. Various techniques were considered to distribute particles into the flow. Initially, a pyramid shaped dispenser was tested (refer to Figure 4.7a). This dispenser consisted of two sheets of triangular shaped Perspex. Particles were manually poured

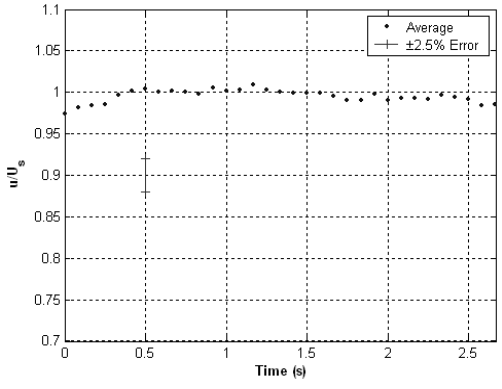

Figure 4.6 - Average stream-wise Lagrangian velocity (u) of five particles tracked over 420mm. Velocities are non-dimensionalised by the background surface velocity (U_s).

into the apex of the triangle. Between the two sheets of Perspex various slots separated particles as they fell from the apex, so that at the base of the dispenser the particles were distributed relatively homogenously across the width of the dispenser. This dispenser provided an adequate number of particles per frame for all flow regimes, but required manual feeding, which meant that the uniformity of particles within the flow was dependant on the rate of pouring. The large fall velocity, that caused particles to plunge into the flow, was also an undesirable feature of this dispenser.

To overcome the difficulty of manual feeding, a mechanically driven dispenser was constructed, based on a design used by Weitbrecht, et al (2002) (refer to Figure 4.7b). The dispenser was assembled from two 42cm Gardena^{TM} 425-20 fertiliser spreaders. The spreaders consisted of a rectangular, plastic hopper, which stored the particles. A rotating brush at the base of the hopper spun on an axle, which forced particles from the storage hopper, through slots at the bottom of the spreader. The two spreaders were attached together and the axles joined together, so that the two spreaders operated as one and spanned the width of the flume. A cog was attached to one end of the axle and attached by a chain-drive to an AC motor. This motor could be operated at variable speed, allowing the particles to be distributed at a variable rate. This dispenser design proved to be the most reliable and consistent method of seeding the flow, and was used for all subsequent experimentation.

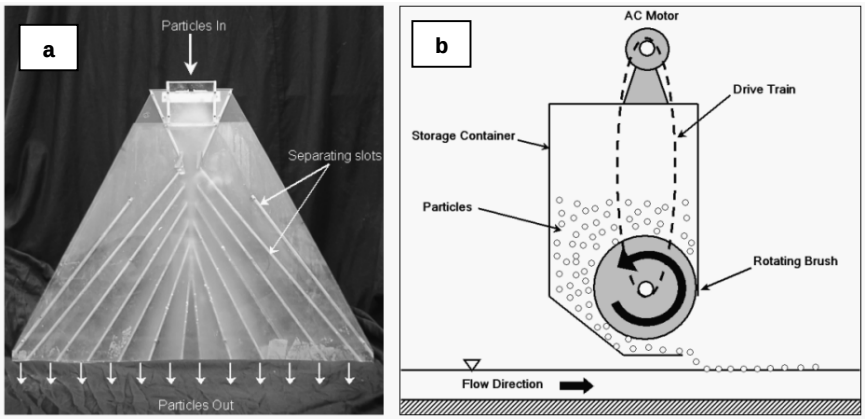

Figure 4.7- **(a)** Pyramid shaped particle dispenser **(b)** Side schematic of mechanically driven particle dispenser (adapted from Weitbrecht, et al, 2002)

The mechanical dispenser seeded the flows at a rate that produced particle densities ranging between 0-1500+ particles per frame. Particle densities greater than approximately 1200 particles per frame lead to severe agglomeration of particles, and particle densities any lower than approximately 300 meant that the particle spacing would be too sparse to resolve any meaningful turbulent information.

As a result approximately 400 particles per frame were used for the shallow turbulent shear flow regime (refer to Section 4.1) in order to minimise particle agglomeration. For the shallow turbulent wake regime, the nature of the wake that was shed in the lee of the cylinder, caused particles to cluster in certain regions, leaving other regions with a lack of particles. In order to compensate for this particle rearrangement approximately 900 particles per frame were used in the shallow turbulent wake regime. Although particle agglomeration was evident in the shallow, turbulent wake regime (refer to Figure 4.8b), this effect was compensated by removing particle matches within agglomerated particles, as outlined in Section 4.3.2.2.

4.3.1.3 Digital Camera

Images of the seeded flow were captured with a PULNiX^{TM} TM-6710 progressive scan digital camera. This camera had a resolution of 684 x 484 pixels, a variable frame rate of up to 120*Hz* and a ½" CCD sensor. The choice of this camera was based on the frame rate. Since the flow velocities were relatively high (up to 1.5*m/s*), frame rates of 60*Hz* were required to capture the particles traces. A shutter speed of 1/500 was used throughout the experimentation.

The trade off for high frame rate is resolution. Although the TM-6710 was of relatively low resolution, it was still adequate for the purposes of experimentation, as the particle identification algorithms outlined in Section 4.3.2.1, could accurately determine the position of the PP particles.

The camera was situated at a distance of 1.9*m* above the flume bed, and affixed with a Pentax^{TM} zoom lens (set to a focal length of 12.5*mm*). This setup gave a PTV image window of 750 x 530*mm* centred

about the midpoint of the channel bed. However the edges of these images were removed due to excessive lens distortion, leaving a PTV window of up to 600*mm* x 440*mm*.

4.3.1.4 Illumination

Provided the water surface was not strongly disturbed by wave motions, illumination of particles floating on the water surface could be achieved by floodlighting. This is a major advantage in capturing surface velocity fields, as PTV measurements made within the water body typically require a laser sheet. Furthermore, a subsurface, horizontal laser sheet was difficult to implement given the shallow flow depths (5-20*mm*) considered in this project. A laser sheet also has the disadvantage of losing particle tracks as particles move in and out of the light sheet.

Consequently, two halogen lights (300 watts each) were sufficient to illuminate the polypropylene particles within PTV image window. The lights were setup on either side of the channel bed and the beam directed down onto the measurement window of the flume. As stated in Section 4.2.1, the flume bed was spray painted black in order to contrast with the white PP particles. This negated any issues with shadows being cast by the PP particles on the channel bed. Such shadows can be mistaken for real particles, and therefore introduce error into the particle tracking process.

4.3.1.5 Image Capture

LabView software was used to control the camera frame rate and to capture images of the seeded flow. A PC equipped with 2GB RAM was used to store images before transferring them to the hard disk. The amount of RAM limited the number of images that could be captured. Typically 3000 images could be stored at a frame rate of 60*Hz* (enabling a 50 second time series). Frames of the captured flow are depicted in Figure 4.8.

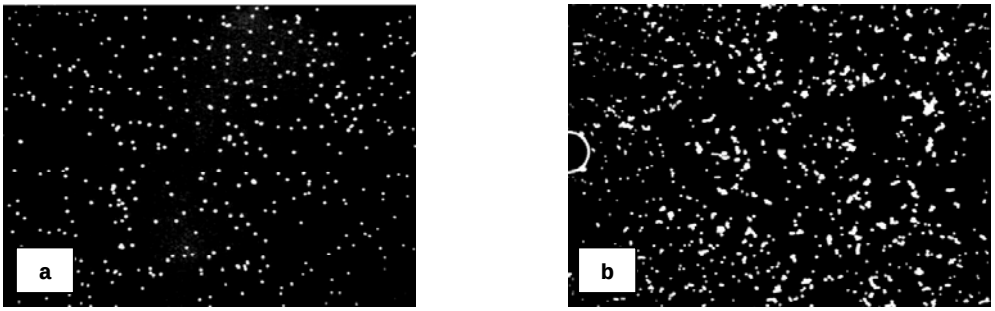

Figure 4.8 - Captured image (not to scale) of the PTV measurement window seeded with polypropylene particles for **(a)** the shallow shear flow regime (approximately 400 particles per frame) and **(b)** the shallow turbulent wake regime (approximately 900 particles per frame).

Before releasing the particles into the measurement window, a ruler shot was taken in order to provide correct length scales for the PTV analysis. This was achieved by placing a scaled-grid at the free surface of the flow, centred about the midpoint of the flume. The grid consisted of a matrix of black dots on a white background (dimension 600 x 440*mm*, with dot spacing 10*mm*). The camera was centred on the grid, and an image of the grid recorded. Horizontal and vertical scales were obtained using ImageStream 4.0 (Nokes, 2005a) by identifying pixels that corresponded to locations on the grid that were a known distance apart.

4.3.2 PTV Analysis

Captured images of the seeded flow were analysed using Streamline 5.0 PTV software (Nokes, 2005b). This programme created two-dimensional velocity fields from the raw images by a three-step process. Firstly, the particles in each frame were identified in order to create a video sequence of the flow. Secondly, particles were tracked from frame to frame using particle-tracking algorithms. Finally, velocity fields were interpolated onto a rectangular grid by analysing the displacement of the particles between frames that are a known time step apart. These three processes are outlined in the following sections.

4.3.2.1 Particle Identification

Streamline 5.0 provided an average-image and Gaussian-image algorithm for the purpose of particle identification. Both algorithms strive to accurately locate the centre of mass of each particle in a

frame, based on the intensity distribution across a particle. Figure 4.9 depicts the typical intensity distribution across one PP particle.

Figure 4.9 - Magnified image of one PP particle, which spans 3-4 pixels in diameter.

The average-image algorithm searches the image for pixels whose intensity exceeds a threshold value, defined by the user. When such a pixel is found, adjacent pixels that also have intensities greater than the threshold value are identified so that the physical extent of the particle can be determined. The size, centre of mass and location of the particles are then calculated. The user can also specify the maximum and minimum size of the particles so that regions that do not correspond to actual particles are eliminated.

The Gaussian-image algorithm is generally a more accurate algorithm that assumes the intensity distribution across a particle is normally distributed. The algorithm searches the image for pixels whose intensity is a local maximum and exceeds a threshold value, defined by the user. Adjacent pixels that exceed a second, user defined threshold value are assumed to be part of the same particle. A Gaussian distribution is fitted in both the *x* and *y* directions to the intensities of pixels on either side of the local maximum. If the Gaussian fit holds, then the particle size and location is recorded to sub-pixel accuracy.

In the present study, the average-image algorithm provided better results than the Gaussian-image algorithm. This was due to the uneven lighting and the non-uniform surface of the floating PP particles. The Gaussian-image algorithm found multiple intensity maxima on one particle, leading to particle identification errors. On the other hand, the average image-algorithm provided reliable particle identification. Another benefit of the average-image algorithm was that is dealt with particle agglomeration well. No maximum size was defined for the particles, so that if the particles agglomerated they were treated as one large particle instead of multiple particles. This significantly

decreased error in the particle-tracking process by removing the potential to track particles embedded within agglomerations.

The average image algorithm calculated the centre of mass of a given particle to an accuracy of $\pm 1/4$ of a pixel. Typically the particles moved in the order of 15*mm* per frame and one pixel spanned approximately 1.18*mm*. Therefore the maximum error associated in the velocity estimates as a result of locating particles with the average image algorithm was approximately ±2%.

4.3.2.2 Particle Tracking

Particle tracking is the essence of a PTV system and the accuracy of this process is crucial to the success of the system (Nokes, et al, 2003). Streamline 5.0 contains a series of costing strategies that employ algorithms to match particles in frame *i* with particles in frame *i+1*. Five costing strategies (distance, correlation, space-average, recent velocity and path length) were used to track particles in the present study, and brief descriptions of these algorithms are provided below. Appendix C provides a detailed outline of the non-dimensional parameters used to optimise the costing strategies, along with a description of the costing strategies used for the shallow, turbulent shear flow and shallow, turbulent wake flow regimes. Further information on particle tracking and costing strategies can be found in Nokes (2005b) and Nokes, et al (2003).

The distance and correlation costing are both examples of state-based costing strategies. A state-based costing requires information only on the state (e.g. size, intensity, location) of each particle in a frame. The *distance costing* strategy is based on the assumption that particles move only a short distance between frames, relative to their inter-particle spacing. This strategy matches a particle in one frame to the particle in the next frame that is the shortest distance away from the original particle. The *correlation costing* strategy is a more complex strategy than the distance costing, and essentially is based on comparing particle patterns, within a user defined window, over two consecutive frames. This is accomplished by calculating the cross-correlation of particle intensities over two subsequent frames, within the user-defined window. Both these costing strategies provided a robust first estimate

of particle tracks, which were subsequently refined using the match-based costing strategies that are outlined below.

The space average velocity, recent velocity and path length costing are all examples of match-based costing strategies. A match-based costing requires matches between particles (i.e. from the state based costing strategies) before being able to determine their costs. Each match-based costing strategy refined matches and removed erroneous matches evaluated from the distance and correlation costing strategies. The *space-average velocity* is a match-based costing that relates the velocity of the particle of interest to the velocities of surrounding particles within a user-defined window. Particles that reside closer to the particle of interest are weighted so that they contribute more to the velocity estimate. The *recent velocity* costing calculates the velocity of the particle of interest, based on current matches in the preceding and succeeding frames. Finally, the *path-length* costing removes particle paths whose length falls below a user-defined threshold.

The path length and recent velocity costing strategies proved effective in removing matches found within agglomerated particles. Avoiding matches from agglomerated particles was desirable as particle agglomerations will be less faithful in tracking the fluid flow due to their greater inertia. It was estimated that severely agglomerated particles counted for up to ten percent of all particles in the PTV window for the shallow turbulent wake regime (as indicated in Figure 4.8b). However these particle matches could be removed by implementing path length and recent velocity costing strategies.

Combinations of the costing strategies described above were used for particle tracking in the present study (as outlined in Appendix C). Application of each costing strategy was implemented over the whole image window, and from the particle tracks velocity fields could be generated as outlined in the following section.

4.3.2.3 Velocity Field Generation

The velocity of each particle (tracked using the costing strategies described in Section 4.3.2.2) could be calculated in Streamline 5.0 by analysing the displacement of the particles between frames that are a known time step apart. The randomly located particle velocities were then interpolated onto a rectangular grid, via Thessian triangulation. This process is illustrated in Figure 4.10.

In Figure 4.10a, velocity estimates (u_i, v_i) are available for three randomly located particles (p_i). The velocity estimate at a grid point, u_g, v_g as denoted in Figure 4.10b, is interpolated from the velocities of the particles at the interpolation triangle's corners. This procedure is carried out over the entire PTV window.

Streamline 5.0 allows the user to specify the extent of the triangles used in the triangulation procedure, as well as the node spacing of the grid (denoted by dimensions Δx_g and Δy_g in Figure 4.10b) onto which velocities are interpolated. If a grid point is located inside a triangle that has dimensions larger than those set by the user then the velocity will be left undefined at that grid point (Nokes, 2005b). Ideally the extent of the interpolation triangles and spacing between the nodes should correspond to the typical inter-particle spacing. This will ensure that velocities are interpolated from real particle tracks, and not smoothed onto the grid points by the interpolation procedure.

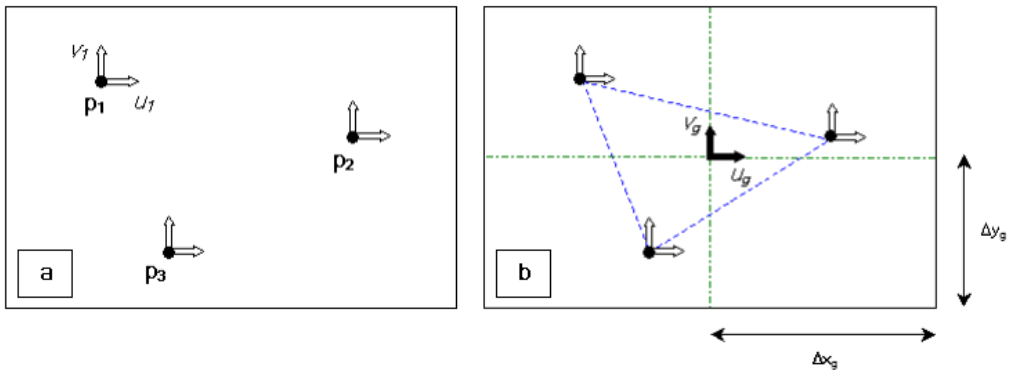

Figure 4.10 – Illustration of the velocity interpolation procedure. **(a)** Velocity estimates (u_i, v_i) for three randomly spaced particles (p_i) **(b)** A grid, outlined in green, is overlaid over the window, and an interpolation triangle, outlined in blue, is used to estimate the velocity at the grid point (u_g v_g), from velocities at the triangle's corners. The grid has a node spacing of Δx_g, Δy_g.

An investigation into the effects of limiting the extent of the interpolation triangles was undertaken for the flow around a circular cylinder. A 60.4*mm* cylinder was placed in a uniform, shallow flow with hydraulic parameters: $\mathrm{Re}_H = 2736$, $H = 20mm$, $S = 0.0025$ and PTV sampling parameters: $f = 20Hz$, $frames = 800$. Data was obtained for one run only, however data from two PTV windows were superimposed. Window B spanned from $x/D \approx 0$ to 10, whilst window A spanned from $x/D \approx 5$ to 15. The inter-particle spacing was approximately $20mm$, and nodes of the rectangular grid were spaced at $10mm$ increments. The maximum dimension of the interpolation triangles was decreased from no limits on their extent, down to an extent of $20mm$.

Figure 4.11a depicts the percentage of the centreline of the PTV window, averaged over time, that was specified with a velocity estimate from the interpolation procedure. As previously mentioned, if a grid point is located inside a triangle that has dimensions larger than those set by the user then the velocity will be left undefined at that grid point. Figure 4.11a indicates that using no limits on the size of the interpolation triangles enabled velocities to be estimated over the centreline of the PTV window one hundred percent of the time. However these velocity estimates are likely to be unreliable as velocities are being interpolated onto grid points from particle tracks that are far from the grid point itself. As the interpolation triangles are reduced to 30*mm*, the amount of coverage decreases sharply. This result is due to a lack of particle tracks within the specified extent of interpolation triangles.

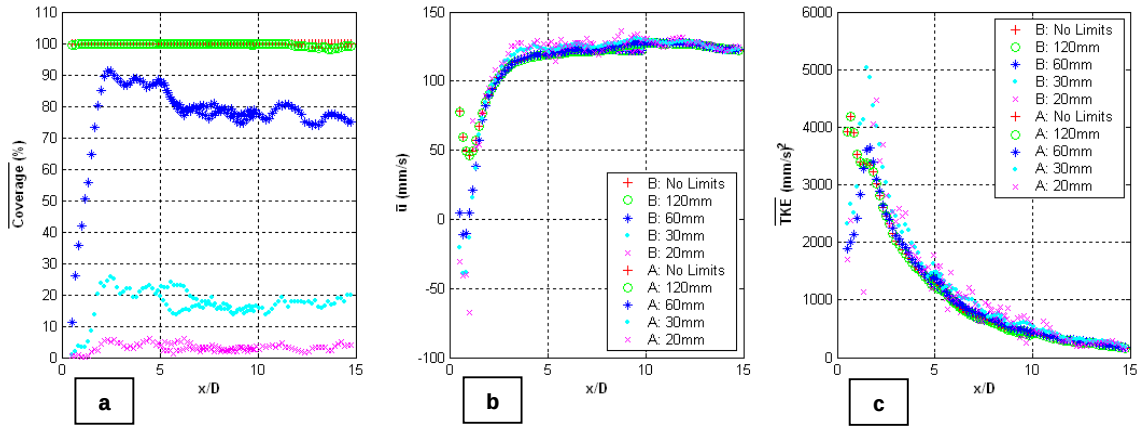

Figure 4.11 - Effect of triangulation limits on time-averaged **(a)** particle coverage (legend the same as Figure 5.9b) **(b)** stream-wise surface velocity and **(c)** turbulent kinetic energy ($0.5(\overline{u'u'} + \overline{v'v'})$) evaluated along cylinder centreline. Data has been superimposed from window A that spanned from x/D=0 to 10 and window B that spanned from x/D=5 to 15.

Figure 4.11b and 4.11c show that the general trend of the time-averaged, stream-wise velocity and turbulent kinetic energy (TKE) evaluated along the cylinder centreline show good agreement, for all sizes of interpolation triangles. As the coverage decreases, the time-averaged profiles show more fluctuation, as the averaging procedure occurs over a shorter data series. Close to the cylinder ($x/D \lesssim 2$) errors result in the return velocity and TKE estimates, as the particle coverage is low and velocities are interpolated from the flow far away from the localised region of low velocity behind the cylinder. As the triangulation limits are decreased the velocity estimates in the near-cylinder region ($x/D \lesssim 2$) become more physically reasonable and peak TKE estimates increase as the velocities are being interpolated only over the localised region of low velocity in the lee of the cylinder.

Overall the investigation into the effect of limiting the extent of the triangulation limits displays (i) that reasonable particle coverage can be obtained by limiting the triangles to 60*mm* (ii) using triangulation limits greater than the inter-particle spacing still provides reliable time-averaged statistics, and (iii) that velocity and TKE estimates in the near wake region, $x/D \lesssim 2$, will be erroneous due to the reasons outlined in the previous paragraph. As a result of these findings, interpolation triangles were specified with an extent of 60*mm* for all time-averaged velocity field calculations, and the grid size was specified at 10*mm*. For time-history information, the grid size was also specified at 10*mm*, but no limits were placed on the Thessian triangles, as a full data series was required for time-history analysis.

It should be noted that velocities were interpolated onto a 10*mm* grid, however this dimension is not indicative of the size of structures that can be resolved by the PTV system. The resolution of the PTV system is discussed in the following section.

4.3.3 Resolution of the PTV System

The resolution of the PTV system is a combination of the camera frame rate, and the density of particle seeding. This section discusses these factors in order to provide an indication of the resolution of the PTV system used for the purposes of this thesis.

The spatial resolution of the PTV system is primarily based on the density of particle seeding. Particle densities of approximately 400 particles per frame were used for the shallow shear flow regime in order to ensure particles did not agglomerate, whilst particle densities of approximately 900 particles per frame were used in the shallow turbulent wake regime. If the particles were homogeneously spaced within the PTV window, then velocity estimates would be available at distances of approximately $30mm$ for the low particle density case, and for the high seeding case at distances of approximately $20mm$. These dimensions provide a conservative estimate of the size of flow structures that can be resolved in the spatial domain.

However it should be noted that as the particles were randomly distributed throughout the PTV window, particles would, at times, be spaced at distances much less than an inter-particle spacing that assumes that the particle distribution is homogeneous. Therefore structures of size less than $20mm$ will be resolved at times, and as a result a grid size of $10mm$ was used to capture any small-scale information. The drawback of using a grid spacing ($10mm$) that is less than the homogeneous inter-particle spacing ($20mm$) is that the Thessian triangulation process will linearly interpolate the instantaneous velocity estimate at points. This will have the effect of smoothing the time-averaged velocity fields.

The temporal resolution of a PTV system is principally a function of the camera frame rate. The frame rate of the camera was set so that the PP particles moved approximately $15mm$ between frames ($particle\,movement = flow\,velocity / f_s$, where f_s represents the frame rate of the camera). The distance particles move between frames provides an indication of the resolution of the PTV system

due to the camera frame rate. However as the velocity at a grid point for each frame is interpolated from surrounding particle matches the particle density will also affect the resolution in the temporal domain. As a result a conservative estimate of $20mm$ is taken to be the limiting size of flow structures that are able to be resolved as a consequence of the camera frame rate.

4.3.4 PTV Errors

This section provides a breakdown of the errors involved with each part of the PTV system, in order to gauge the total error associated with the surface velocity fields.

Scales for the images were measured from a scaled-grid, which consisted of a matrix of black dots on a white background (dimension 600 x 440mm, with dot spacing at 10mm) centred about the midpoint of the flume (as outlined in Section 4.3.1.5). An error between the true length of the image and the length obtained via Imagestream 4.0 was estimated to be $\pm 0.5\%$ (due to image distortion and difficulties in correctly identifying pixels that corresponded to scales on the grid). The horizontal and vertical scales obtained from Imagestream 4.0 were consequently used in the PTV analysis to calculate velocities. Therefore the $\pm 0.5\%$ scale error was passed onto the velocities.

As outlined in Section 4.3.2.1, the average image algorithm was used for all PTV analysis. The error associated with the velocity estimates as a result of locating particles with the average image algorithm was approximately $\pm 2\%$. The particle tracking algorithms can also introduce error by incorrectly matching particles. However incorrect particle matches were largely eliminated through careful use of recent velocity, and path-length algorithms. Therefore it is estimated that the total error involved in the instantaneous velocity estimates generated by the PTV system is estimated to be a randomly distributed error of $\pm 2.5\%$.

4.3.5 Data Analysis

Streamline 5.0 provided three-dimensional (x, y, t) streamwise (u) and spanwise (v) velocity fields. These fields were exported from Streamline 5.0 into MATLAB 6.5 for analysis.

4.3.6 Summary of PTV System

Table 4.2 provides a summary of the individual components that make up the PTV system designed to capture velocity fields at the surface of shallow flows, over a window of up to 600*mm* x 440*mm*. It is estimated that the total error in surface velocity fields generated by the PTV system is $\pm 2.5\%$. Furthermore it is estimated that the PTV system can resolve large-scale flow structures in the order of $20mm$.

Table 4.2 – Summary of the physical components of the PTV system used to capture velocity fields at the surface of shallow flows.

Camera	
Type	PULNiX TM 6710
CCD chip	1/2" Progressive Scan
Resolution	648x484
Max Frame Rate	120 Hz
Lens	Pentax 12.5 - 75mm Zoom Lens
Tracer Particles	
Material	Polyproplyene
Diameter	2-3 mm
Density	0.9 g/cm^3
Particle Dispenser	
Custom-made mechanically driven particle spreader	
Illumination	
2 halogen lights (300 Watts each)	
PC for frame capture and data storage	
Type	INTEL P-IV 2.4GHz, 2GB RAM
Software	LabView
PC for PTV analysis	
Type	AMD Athlon 3000+, 1GB RAM
Software	Streamline 5.0 Imagestream 5.0 MATLAB 6.5

4.4 EXPERIMENTAL PROCEDURES

The typical procedure used to establish the flow and capture images of the tracer particles is outlined below:

(i) The channel bed was set to desired slope with a survey level.

(ii) The digital camera was levelled (with a slope adjustable spirit level) to correspond with the channel bed slope, and was positioned to coincide with the midpoint of channel bed.

(iii) An image of a scaled-grid (elevated to the level of flow depth), was captured and PTV window scales were evaluated from the grid using Imagestream 4.0.

(iv) The sluice gate was positioned, 110*mm* from downstream edge of the channel bed for sub-critical flow regimes and 50*mm* from the upstream edge of the channel bed for super-critical flow regimes.

(v) The desired flow was set by filling the polythene tank, starting the pumps and adjusting the flow control valves.

(vi) Flow depths were acquired with a point gauge.

(vii) The particle dispenser was setup (positioned 200*mm* from the upstream edge of the channel bed).

(viii) The particle dispenser was started, and images of seeded flow were captured and stored to PC.

(ix) The particle dispenser was stopped, and particles were collected from a sieve located within the outlet basin.

(x) Step (viii) and (ix) was repeated for each experimental run, and steps (i) to (vii) were carried out for each flow regime.

4.5 SUMMARY

The present chapter has detailed the experimental apparatus and techniques used to gather data for the purpose of analysing the mean flow and turbulent properties of shallow flows. Section 4.1 outlined the two experimental programmes to be considered. All flows are generated in a variable slope, shallow flow flume, with channel bed dimensions 1970*mm* x 974*mm*, as described in Section 4.2. To determine surface velocity fields a particle tracking velocimetry (PTV) system that utilised polypropylene particles was employed, as described in Section 4.3. Finally, Section 4.4 listed the experimental procedure used to establish flows and capture digital images of the seeded flows for subsequent PTV analysis. Chapters 5 and 6 discuss the results obtained from experimentation.

5.0 Results I: Analysis of Shallow Turbulent Shear Flows

The experimental results are split into two chapters. This chapter presents and discusses the results from shallow, turbulent shear flows generated in the laboratory. A circular cylinder was then introduced into the shallow shear flows outlined in this chapter, in order to generate large-scale quasi-2D turbulent structures. Chapter 6 discusses the experimental results obtained from this shallow, turbulent wake flow.

Section 5.1, of the present chapter, outlines the experimental programme, and Section 5.2 provides a qualitative description of the flow visualised by dye injection. The time-averaged profiles of velocity and turbulent intensity are presented and discussed in Section 5.3. In Section 5.4 the probability density function, autocorrelation and power spectral density are evaluated to obtain quantitative information regarding the flow structure. Finally, in Section 5.5 the key experimental results are summarised.

5.1 EXPERIMENTAL PROGRAMME

The purpose of analysing shallow, turbulent shear flows was to (a) assess the ability of the PTV system to resolve turbulent statistics for simple uniform flow conditions (b) provide information regarding the turbulent structure at the surface of such flows and (c) provide a data set for comparison with the data obtained in the shallow, turbulent wake regime, presented in Chapter 6.

5.1.1 Flow Regimes

A total of thirty-two experimental runs were completed, that involved three different flow regimes. These three regimes were denoted A, B and C, and the hydraulic data for each are outlined in Table 5.1. Bed slopes, flow rates and flow depths were obtained by the methods outlined in Chapter 4. The cross-sectional mean velocity, U_a as listed in column five, was evaluated according to Eq. (5.1), where Q is the measured discharge and A is the cross-sectional area of the flow. The shear velocity

Table 5.1 - Hydraulic parameters for flow regimes A, B and C

Flow Regime	Slope	Flow	Depth	Mean Velocity	Shear Velocity	Friction Coefficient	Froude #	Reynolds #
	S (rad)	Q (l/s)	H (mm)	U_a (mm/s)	u_* (mm/s)	c_f (-)	Fr (-)	Re_H (-)
A	0.1280	6.27	5.1	1262.2	79.6	0.0080	5.64	6437
B	0.0500	6.26	7.0	913.8	58.3	0.0081	3.48	6427
C	0.0025	2.67	20.0	136.8	8.5	0.0077	0.31	2741

(u_*) was evaluated according to: $u_* = \sqrt{gRS}$ (refer to Section 3.2.1). However due to error contained in the bed slope measurement for regime C, the shear velocity for this regime was calculated by a method described in Appendix D. The friction coefficient (listed in column seven of Table 5.1) was evaluated according to Eq (5.2). Finally, the Reynolds and Froude numbers were calculated according to Eq. (5.3) and Eq. (5.4) respectively.

$$U_a = Q / A \tag{5.1}$$

$$c_f = 2\left(\frac{u_*}{U_a}\right)^2 \tag{5.2}$$

$$\mathrm{Re}_H = \frac{U_a H}{\upsilon} \tag{5.3}$$

$$Fr = \frac{U_a}{\sqrt{gH}} \tag{5.4}$$

Flow regime A had the steepest slope and was the shallowest, supercritical flow that could be produced given the size of the particles used in the PTV system. Flow regime B was an intermediate slope, relative to A and B. Finally, regime C was the deepest sub-critical flow that could be produced based on the development of a turbulent boundary layer, as described in Section 5.1.3.

5.1.2 Sampling Parameters

The PTV sampling parameters for the three flow regimes are summarised in Table 5.2. The sampling period of regime A and B was limited by the storage capacity of the PC. For these regimes, 2899 frames were able to be stored at a frame rate of 60*Hz*, allowing for a total sampling time of 48 seconds. The sampling time of regime C was limited by the amassing of particles on the downstream

Table 5.2 - PTV sampling parameters for flow regimes A, B and C

Flow Regime	Sampling Frequency (Hz)	Sampling Period (sec)	PTV Frames (#)	Number of Runs (#)
A	60	48	2899	8
B	60	48	2899	8
C	12	83	1000	16

sluice-gate, which enabled approximately 80 seconds of video footage, recorded at 12*Hz*, to be captured before particles protruded to within 100*mm* of the PTV measurement window. The reason for altering the frame rate for each flow regime was to ensure that particles moved in the order of 15*mm* per frame, or greater ($particle\,movement \approx flow\,velocity / frame\,rate$). This ensured that errors in the velocity estimates as a result of the particle identification process were minimised (as outlined in Section 4.3.2.1).

Sixteen experimental runs were completed for regime C and eight for regimes A and B. The time-averaged streamwise surface velocity, measured at the midpoint of the PTV window, deviated by a maximum of $\pm 0.8\%$ between runs for regime A and by $\pm 1.25\%$ for regime C. This indicates that the experimental runs were repeatable. Repeating experiments improved averaging procedures, by allowing both time and ensemble averaging. The number of runs for regime C was double that of regimes A and B to keep a relatively consistent number of frames for analysis purposes.

5.1.3 Coordinate System & PTV Measurement Window

The coordinate system is outlined in Figure 5.1. The coordinates for the channel bed are in uppercase, $[X \;\; Y]$, and the coordinates for the PTV window are denoted in lowercase, $[x \;\; y]$. The PTV window was centred about the mid-point of the flume and spanned $\pm 280mm$ in the x-direction and $\pm 200mm$ in the y-direction. The coordinate origin for the PTV window was located on the centreline of the flume and the upstream boundary of the PTV window. Velocities obtained via PTV analysis were interpolated onto a grid with a cell size of $10mm$ x $10mm$ that covered this window (as outlined in Section 4.3.2.3).

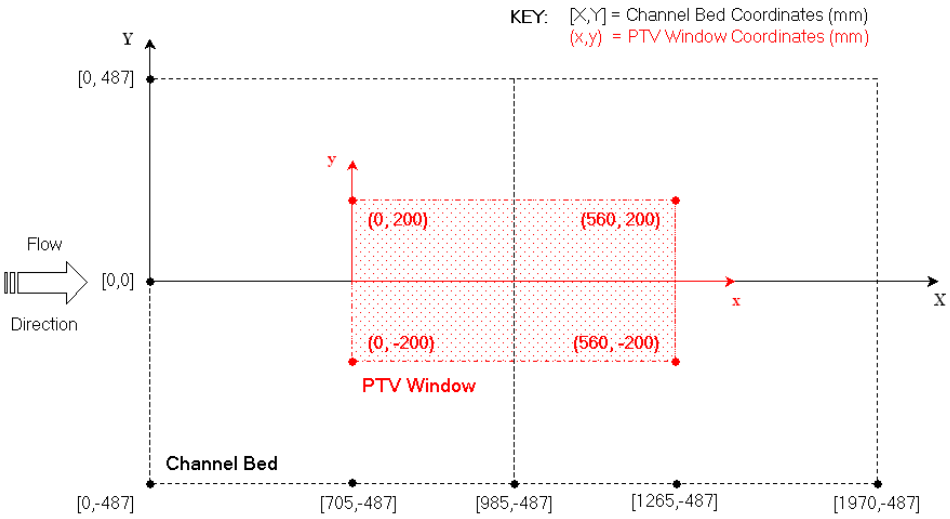

Figure 5.1 - Illustration of the extent of channel bed, PTV measurement window and coordinate system. All units are in millimetres. Diagram is not to scale.

The lateral edges of the PTV window were located 287*mm* from the walls of the flume, in order to minimise interference effects from the sidewalls. Furthermore, the PTV window was located 685*mm* from the flume inlet, in order to provide sufficient distance for growth of the turbulent boundary layer in regime C. As regime C was the deepest flow, this was the critical case in estimating the development length of the turbulent boundary layer based on the formula, $\delta = 0.38x\left(\mathrm{Re}_x\right)^{-1/5}$ given in Henderson (1966). Definitions of the parameters stated in this formula are outlined in Section 3.2.1.

In order to ensure uniform flow, a sluice gate was used in each regime (refer to Appendix A). For regimes A and B the sluice-gate was positioned upstream of the PTV window, at a location of $X = 50mm$. The height of the sluice gate was 9*mm* above the channel bed for regime A and 12*mm* for regime B. For regime C the sluice gate was placed downstream of the PTV window at a location of $X = 1860mm$, and adjusted to a height of 6*mm* above the channel bed.

5.2 VISUAL OBSERVATIONS

Dye was injected into flow regime C in order to visualise the turbulent structure of the flow. Figure 5.2a depicts dye injected at the mid-depth of the flow, $300mm$ downstream of the inlet. The image is centred about the midpoint of the flume. The dye was observed to spread rapidly throughout the depth of the flow, indicating the presence of 3D turbulent structures. Furthermore the width of the plume grew steadily with distance from the source.

Figure 5.2b was produced by injecting dye onto the free surface of the flow, $300mm$ downstream of the inlet. Again the image is centred about the midpoint of the flume. In this case the dye was largely confined to the free surface (i.e. it did not spread throughout the depth of the flow). This can be attributed to the lack of vertical turbulent mixing processes at the free surface. It is expected that for large distances downstream, the dye would spread throughout the depth of the flow. Furthermore, the dye was observed to disperse by quasi two-dimensional, turbulent structures at the water surface. The presence of these structures at the free surface is consistent with the observations by Kumar, et al (1998), who defined the structures as spiral eddies.

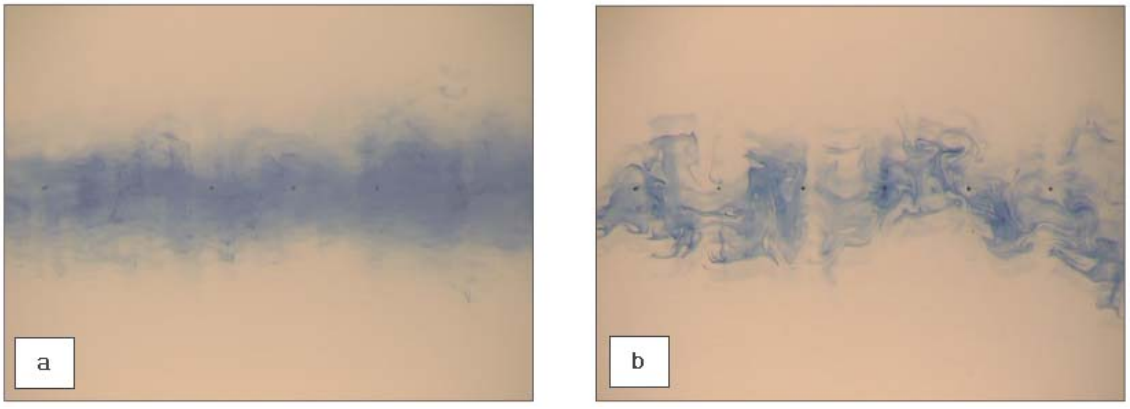

Figure 5.2 - Turbulent structures visualised in flow regime C by dye injected at **(a)** the mid-depth of the flow; and **(b)** the surface of the flow (black points on the bed represent 5cm spacing). Window size approximately 300mm x 170mm. Note: shadowing effects are present in both images (a) and (b).

5.3 TIME-AVERAGED ANALYSIS

PTV provided three-dimensional (x, y, t) arrays of the instantaneous streamwise (u) and spanwise (v) velocity at the surface of the three flow regimes, as depicted schematically in Figure 5.3. The following notation is used to the present the PTV data. Instantaneous velocities consist of a mean (time-averaged) component $\overline{U}$ or $\overline{V}$, and a turbulent fluctuation u' or v'. All mean values were evaluated over eight runs for flow regimes A and B and sixteen runs for regime C. Ensemble averaging notation, $\langle\ \rangle$, is dropped for convenience.

The important parameters used to non-dimensionlise data in the flowing sections include the flow depth (H), cross-sectional mean velocity (U_a), and the global-mean surface velocity (U_s). The global-mean surface velocity was calculated by averaging the PTV evaluated surface velocities over ensemble, time and space. This statistic provided a bulk measure of the surface flow velocity.

The following sections aim to establish that the flow fields were horizontally homogeneous for both the mean velocity and turbulent stress components. This section will also provide an indication of the ability of the PTV system to collate mean velocity and turbulent statistics (i.e. u'_{irms} , TKE, $-\overline{u'v'}$).

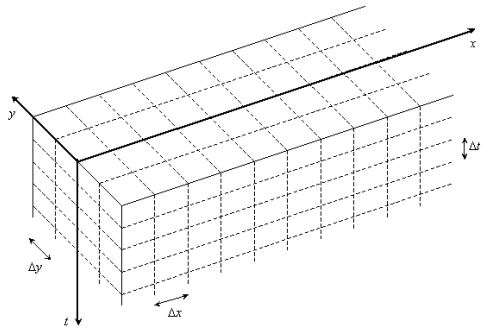

Figure 5.3 – Schematic visualisation of a 3D velocity vector field produced via PTV for one experimental run. The measurement field ranged from y =[-200mm 200mm] and x=[0mm 560mm]. Node spacing: Δx = 10mm, Δy = 10mm, Δt = 0.0833s for flow regime A and Δt = 0.01667s for regimes B and C.

5.3.1 Mean Velocity

The global-mean streamwise surface velocity, U_s, is compared with the cross-sectional averaged velocity, U_a, for each flow regime in Table 5.3. Weitbrecht, et al (2002), states that the Blasius $1/7^{th}$ power law predicts that the cross-sectional averaged velocity is theoretically equal to 0.817 of the surface-velocity (i.e. $U_a = 0.817U_s$). In the present study, flow regime C predicts a value slightly less (-2.1%) than the theoretical value, while regime A predicts a value slightly higher ($+2.4\%$).

This discrepancy may be attributed to particle submergence. The particles were submerged approximately $2mm$ below the water surface, and therefore will sample a velocity more analogous to the cross-sectional averaged velocity for flow regime A ($5mm$ depth), while for regime C ($20mm$ depth) the velocities sampled will be more representative of the surface-velocity. Overall, the surface-velocities obtained by PTV provide a good match with the theoretical prediction, however it should be noted that as the PP particles are partially submerged they will be sampling the surface velocity plus a portion of the sub-surface flow.

The time-averaged velocity profiles, normalised by the surface velocity, U_s, are plotted in Figure 5.4. The coordinate axes have been normalised by the flow depth, H. Figure 5.4a depicts $\overline{U}(x/H)$ and $\overline{V}(x/H)$ averaged over y, and Figure 5.4b depicts the same quantities evaluated in the transverse direction, i.e. $\overline{U}(y/H)$ and $\overline{V}(y/H)$, averaged over x. These figures indicate that the flows are

Table 5.3 - Comparison of PTV evaluated surface velocity (U_s) and cross-sectional mean velocity (U_a).

Flow Regime	U_s (mm/s)	U_a (mm/s)	$\frac{U_a}{U_s}$ (-)
A	1508.4	1262.2	0.837
B	1111.8	913.8	0.822
C	170.9	136.8	0.800

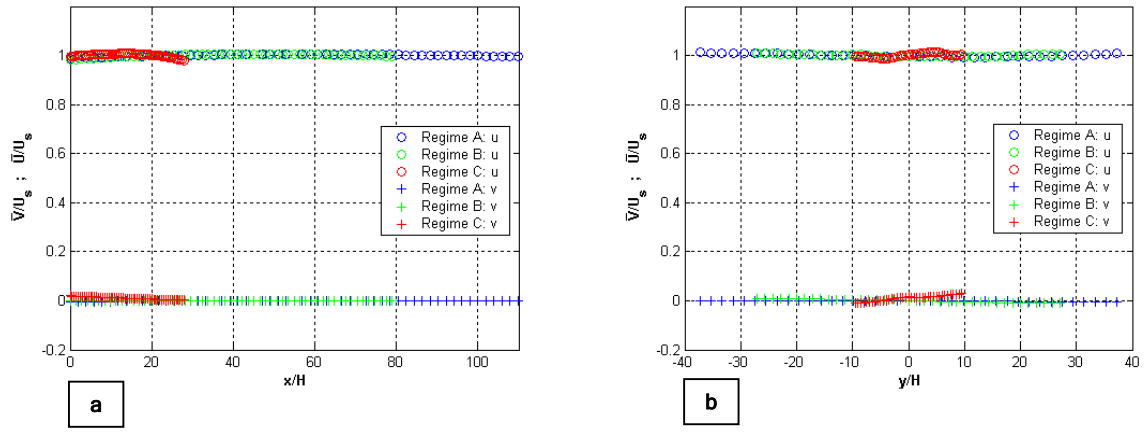

Figure 5.4 - **(a)** $\overline{U}(x/H)$ and $\overline{V}(x/H)$, normalised by U_s averaged over y. **(b)** $\overline{U}(y/H)$ and $\overline{V}(y/H)$, normalised by U_s averaged over x.

predominantly homogeneous and uniform over the flow field to within approximately ±2.5%. The slight departure from uniform flow may be attributed to unavoidable unevenness in the channel bed and variation in the flow discharge. Flow regime C departs from uniform flow more markedly than regimes A and B in the longitudinal direction due to the presence of the backwater-curve from the downstream sluice gate encroaching into the PTV measurement window. The upstream sluice gate used for flow regimes A and B is also more effective in eliminating cross-stream velocity gradients as displayed in Figure 5.4b.

5.3.2 Turbulent Components

The streamwise and spanwise turbulent intensities averaged globally (i.e. over time and space, for all runs) are given in Table 5.4. Values are also stated for the normalised turbulent intensity (u'_{irms}/u_*) evaluated for $z/H = 1$, using the semi-empirical formula stated in Eq. (5.5), where $C_u = 2.3$ and $C_v = 1.63$. This formula has been verified experimentally for open channel flow using LDV (Nezu & Nagakawa, 1993) for regions outside of the viscous sub-layer (i.e. $0.15 \le z/H \le 0.9$). The normalised turbulent intensity components evaluated using PIV at the free-surface of an undisturbed shallow flow by Weitbrecht (2004) are also specified in Table 5.4.

$$\frac{u'_{irms}}{u_*} = C_{u_i} e^{(-z/H)} \tag{5.5}$$

Table 5.4 indicates that the turbulent intensities measured in the present study using PTV are consistently lower than the turbulent intensities estimated using Eq. (5.5), for both the streamwise and spanwise components (c.f. $u'_{rms}/u_* = 0.42$ for regime A, with $u'_{rms}/u_* = 0.85$ from Nezu & Nagakawa, 1993).

The reason for the discrepancy between turbulent intensity measurements in the present study, relative to those predicted by Nezu & Nagakawa (1993), may stem from a number of sources. Firstly it should be noted that the turbulent intensity data of Nezu & Nagakawa (1993) has been extrapolated to the free-surface (i.e. $z/H = 1$) from sub-surface turbulent intensity measurements (i.e. for $0.15 \le z/H \le 0.9$). At the free surface, turbulent velocity fluctuations are likely to be damped and therefore turbulent intensities measured at the free surface will reflect this.

Secondly, the lower turbulent intensity estimates can be attributed to the limited spatial and temporal resolution of the PTV system. Section 4.3.4 states that flow structures greater than approximately $30mm$ can be accurately resolved. The spatial averaging as a result of using interpolation triangles will filter turbulent fluctuations resulting from structures of size less than the resolution of the PTV system. This was also the finding of Weitbrecht (2004), who used a PIV system with similar temporal and spatial resolution to the PTV system used in the present study, and accordingly, the results for $u'_{i\,rms}/u_*$ evaluated in the present study, compare well with the PIV values of $u'_{i\,rms}/u_*$ evaluated by Weitbrecht (2004). This indicates that the spatial averaging of the PTV system has the effect of underestimating turbulent intensity values for regions where the length scales of the turbulent structures are in the order of the system resolution (Weitbrecht, 2002).

Table 5.4 – Comparison of turbulent intensities measured with PTV at the free-surface

Flow Regime	u_* (mm/s)	u'_{rms} (mm/s)	v'_{rms} (mm/s)	$\frac{u'_{rms}}{u_*}$ (-)	$\frac{v'_{rms}}{u_*}$ (-)	$\frac{v'_{rms}}{u'_{rms}}$ (-)
A	79.6	33.2	21.7	0.42	0.27	0.65
B	58.3	26.0	17.6	0.45	0.30	0.68
C	8.5	5.6	3.9	0.66	0.46	0.70
Weitbrecht (2004)	-	-	-	0.45	0.33	0.73
Nezu & Nagakawa (1993)	-	-	-	0.85	0.60	0.71

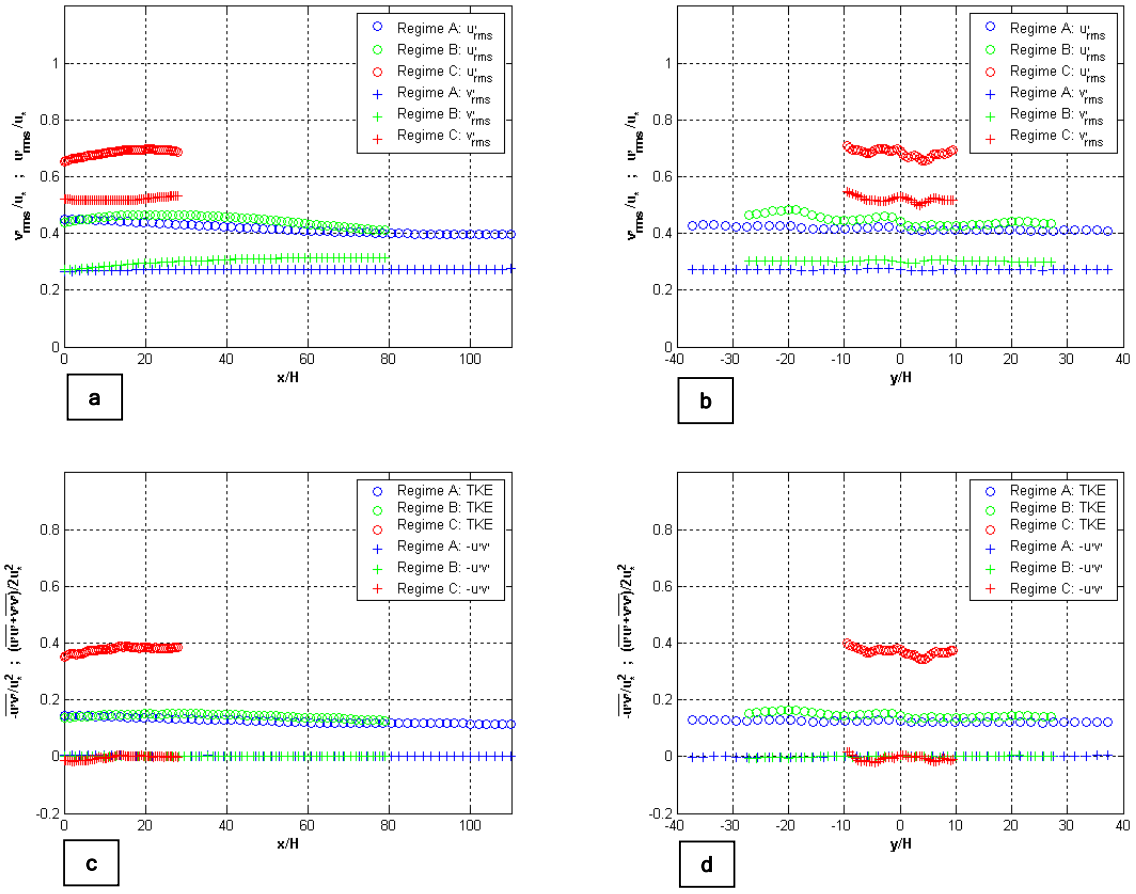

Figure 5.5 – **(a)** $u'_{rms}(x/H)$ and $v'_{rms}(x/H)$ normalised by u_*, averaged over y. **(b)** $u'_{rms}(y/H)$ and $v'_{rms}(y/H)$ normalised by u_*, averaged over x. **(c)** Longitudinal profiles of TKE ($0.5(\overline{u'u'}+\overline{v'v'})$) and Reynolds stress ($-\overline{u'v'}$), normalised by u_*, and averaged over y. **(d)** Transverse profiles of $0.5(\overline{u'u'}+\overline{v'v'})$ and $-\overline{u'v'}$, normalised by u_*, and averaged over x.

Figure 5.5a depicts $u'_{rms}(x/H)$ and $v'_{rms}(x/H)$ averaged over the transverse axis. Figure 5.5b depicts $u'_{rms}(y/H)$ and $v'_{rms}(y/H)$ averaged over the longitudinal axis. The turbulent kinetic energy ($TKE = 0.5\left(\overline{u'u'} + \overline{v'v'}\right)$) and Reynolds stress ($-\overline{u'v'}$) are also plotted in Figure 5.5c and 5.5d respectively. Firstly, these figures show that the turbulence is largely homogeneous over the flow field. Departure from homogeneity (in the order of $\pm 5\%$) may be attributed to flow interaction with the sluice gates, flow disturbances due to the inlet conditions and minor variation in the channel bed and flow discharge. Secondly, Figures 5.5a and 5.5b, indicate that the turbulent intensities for flow regime C are consistently higher than regimes A and B (cf. $u'_{rms}/u_* \approx 0.66$ for regime C and $u'_{rms}/u_* \approx 0.42$ for regime A). It is expected that the normalised turbulent intensity ($u'_{i\,rms}/u_*$) is a universal constant for turbulence in smooth, open-channels (Nezu & Nagakawa, 1993).

The disparity in turbulent intensity between regimes could be attributed to a number of reasons. Firstly, it should be noted that the calculated value of u_* for flow regime C will be less reliable than the shear velocity estimated for regimes A and B, as outlined in Appendix D. The difficulty in estimating u_* for flow regime C could lead to the discrepancy in $u'_{i\,rms}/u_*$ estimates between regimes.

Secondly, the particle sampling depth will contribute to the observed difference in $u'_{i\,rms}/u_*$ between flow regimes A, B and C. As illustrated in Figure 5.6 the sampling depth of the particles in regimes A and B is greater relative to regime C, in which particles sample, approximately, the top 15% of the flow depth. It is expected that if a particle samples a greater proportion of the flow depth, then the particle will be exposed to turbulent fluctuation gradients, which when averaged will lead to a lower estimate of the turbulent intensity. This is reflected in the trends of $u'_{i\,rms}/u_*$ evaluated for the three flow regimes (refer to Figure 5.5a and 5.5b) in which a more representative turbulent intensity, relative to the findings of Nezu & Nagakawa (1993), is approached as the relative particle submergence, d_p/H, decreases. Also the fact that the ratio of v'_{rms}/u'_{rms} is approximately consistent between

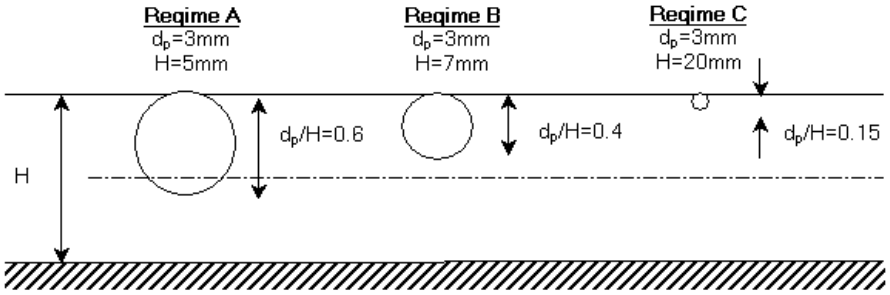

Figure 5.6 - Relative particle submergence (d_p/H) for flow regimes A, B and C, where d_p represents the particle diameter and H denotes the flow height.

regimes (refer to column seven of Table 5.4) indicates that the particle sampling effect filters both u'_{rms} and v'_{rms} equally.

In summary, the turbulent intensities evaluated by the PTV system underestimate the semi-empirical values stated by Nezu & Nagakawa (1993). This effect is believed to stem from the limited resolution of the PTV system, which filters turbulent fluctuations as a result of the velocity interpolation process, and the effect of particle submergence relative to the flow depth. However the ratio of v'_{rms}/u'_{rms} evaluated by the PTV system is directly comparable to the values stated by Nezu & Nagakawa (1993). This indicates that turbulent structures are accurately being resolved by the PTV system, but their absolute intensity is being damped due to the reasons stated above.

To obtain turbulent intensity values closer to those stated by (Nezu & Nagakawa, 1993), the resolution of the PTV system would need to be increased. This could be achieved by using smaller, more densely spaced particles with a higher resolution camera and frame rate. It is recommended that future studies investigate increasing the resolution of the surface PTV system by changing these parameters.

5.4 TIME-HISTORY ANALYSIS

The time-averaged properties outlined in Section 5.3, provided a quantitative measure of the bulk characteristics of turbulence in shallow, uniform shear flows. The following sections present and discuss the probability density function (PDF), autocorrelation and power spectral density (PSD) in order to obtain quantitative information regarding the evolution of turbulence over time and space.

5.4.1 Probability Density Functions

The probability density function for the standardised instantaneous velocity ($\hat{u}_i = (u_i - \overline{U_i})/\sigma_{u_i}$) was evaluated for time-histories at points along the longitudinal centreline (i.e. for $y = 0\,mm$) and transverse centreline (i.e. for $x = 280\,mm$) of the PTV window. Figure 5.7a represents an average of all PDFs evaluated along the longitudinal centreline. A circular marker denotes the streamwise velocity and a cross denotes the spanwise velocity. Accents to denote a standardised variable ($\hat{u}_i$) have been dropped for convenience. All flow regimes have been superimposed, and each PDF represents an ensemble average. In Figure 5.7b the same procedure has been undertaken for time-histories at points along the transverse centreline (i.e. at x=280mm) of the PTV window.

The skewness (Sk_{u_i}) and flatness (Fl_{u_i}) distributions are depicted in Figure 5.7c and 5.7d, for all points along the respective longitudinal and transverse centrelines of the PTV window. Table 5.5 provides a summary of the moments of the PDFs (refer to Section 2.3.2) averaged over time and ensemble for the longitudinal and transverse centrelines only, where $\overline{\hat{u}_i}$ represents the mean of the standardised instantaneous velocity component, $\sigma_{\hat{u}_i}^{\,2}$ denotes the variance of the standardised velocity component, $Sk_{\hat{u}_i}$ the skewness, and $Fl_{\hat{u}_i}$ denotes flatness. All moments are dimensionless and have been estimated using the Trapezoidal rule.

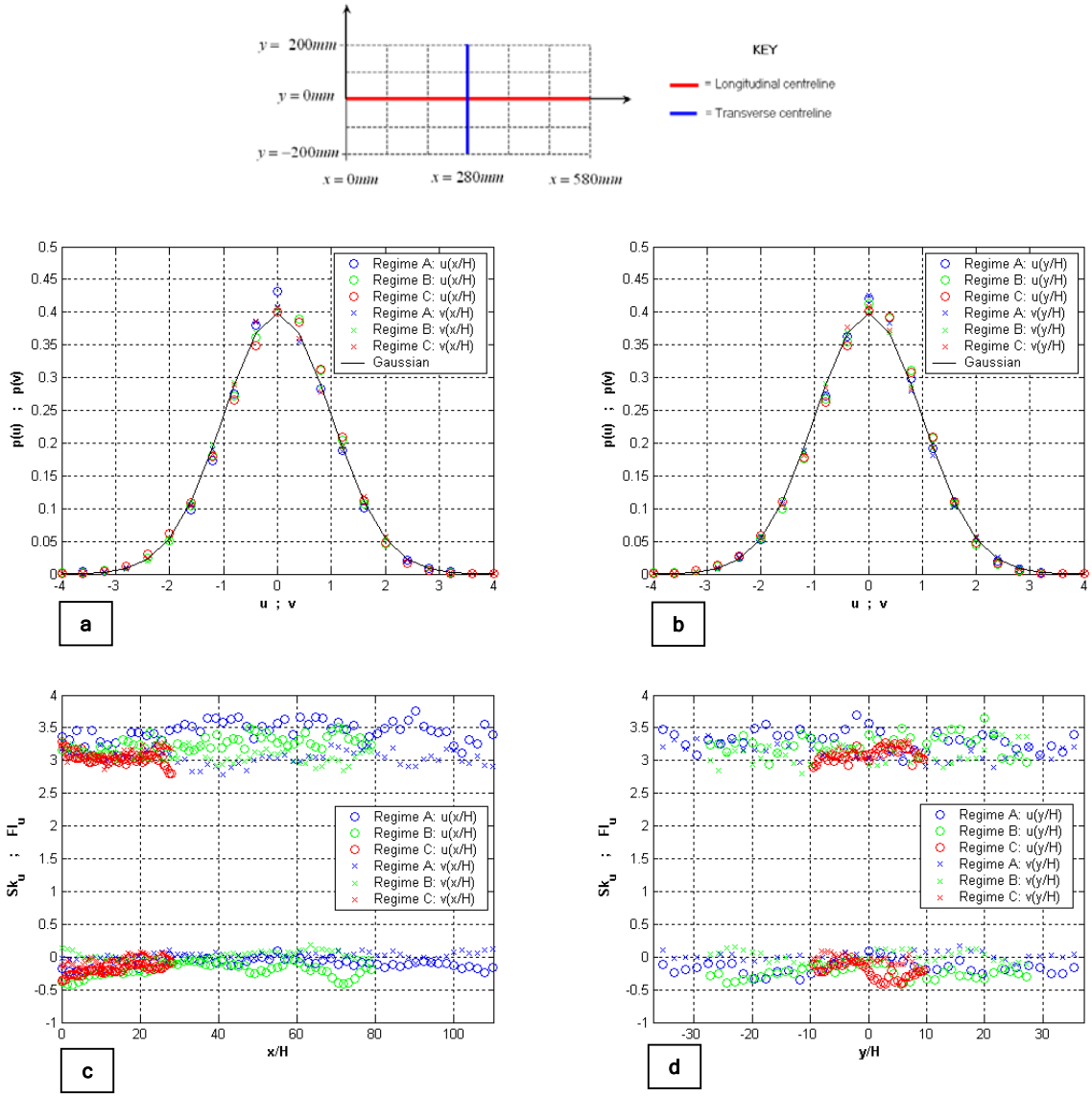

Figure 5.7 -Probability density function (PDF) for $\hat{u}$ and $\hat{v}$ (accents have been dropped for convenience) averaged over the **(a)** longitudinal centreline (i.e. for y=0mm as depicted in the diagram at the top of the figure) and **(b)** transverse centreline (i.e. for x=280mm). Skewness and flatness distributions for $\hat{u}$ and $\hat{v}$ evaluated over the **(c)** longitudinal and **(d)** transverse centrelines.

Table 5.5 - Moments calculated from PDFs evaluated in Figure 5.6. All moments represent a mean over ensemble and space (for the longitudinal and transverse centrelines only), where $\overline{\hat{u}_i}$ = mean of the standardised instantaneous velocity component ($\hat{u}_i$), $\sigma^2_{\hat{u}_i}$ = variance, $Sk_{\hat{u}_i}$ = skewness and $Fl_{\hat{u}_i}$ = flatness.

Flow Regime	$\overline{\hat{u}}$	$\overline{\hat{v}}$	$\sigma^2_{\hat{u}}$	$\sigma^2_{\hat{v}}$	$Sk_{\hat{u}}$	$Sk_{\hat{v}}$	$Fl_{\hat{u}}$	$Fl_{\hat{v}}$
A	0.001	0.000	1.00	1.01	-0.1	0.0	3.4	3.1
B	0.003	0.000	1.00	1.01	-0.2	0.0	3.3	3.1
C	0.001	0.000	1.00	1.01	-0.2	-0.1	3.2	3.2

The plots presented in Figure 5.7a and 5.7b show that the PDF is approximately equivalent when evaluated in the transverse and longitudinal directions, indicating homogeneity across the flow field. Furthermore Figure 5.7c and 5.7d indicate that $p(\hat{u}_i)$ is predominantly Gaussian (as the Gaussian probability distribution is characterised by a skewness of zero and flatness of three). This suggests that the turbulence, sampled by the PP particles submerged partially below the free surface, is essentially random.

However column eight of Table 5.5 indicates that $p(\hat{u})$ is slightly more peaked than the Gaussian distribution (cf. $Fl_{\hat{u}} = 3.4$ for flow regime A), while the spanwise flatness is closer to the Gaussian value of 3. A flatness of greater than three indicates that relatively large excursions from the mean are more probable in the streamwise velocity signal. Such excursions could physically be introduced from intermittent 2D structures at the free surface (e.g. spiral eddies as identified by Kumar, et al, 1998).

5.4.2 Autocorrelation

The temporal autocorrelation function evaluated for the time-history at the midpoint of the flow field (i.e. for the time-history at $u_i'(280mm, 0mm, t)$) is depicted for the streamwise and spanwise fluctuating velocity components in Figure 5.8 for all flow regimes. The temporal autocorrelations depicted in Figure 5.8 represent an ensemble average, and the temporal delay, τ, has been normalised by U_s / H, where U_s is the global-mean surface velocity, and H is the flow depth.

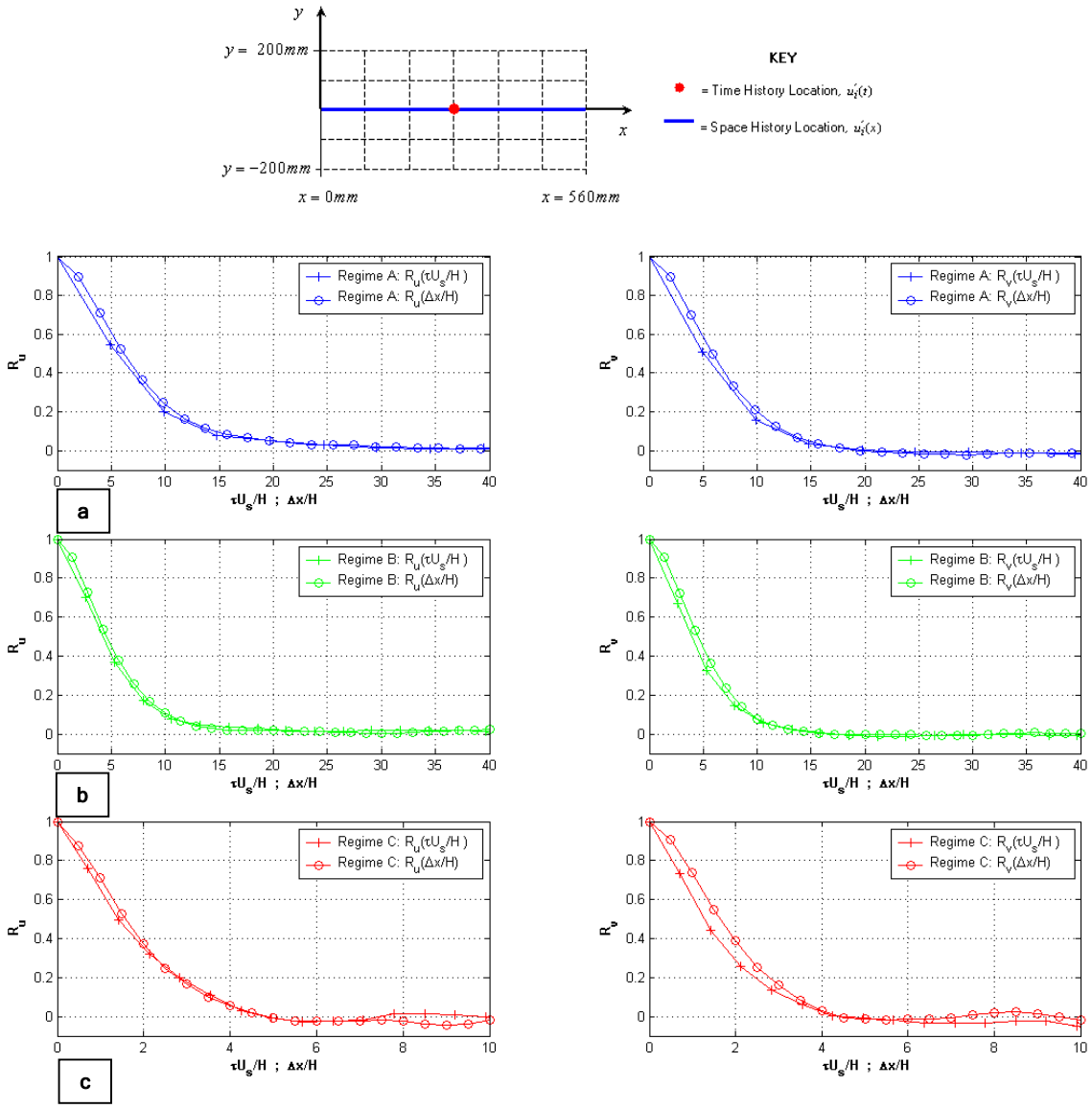

Figure 5.8 – Temporal autocorrelation, $R_{ui}(\tau U_s/H)$, evaluated for time-histories at the midpoint of the flow field, and the spatial autocorrelation, $R_{ui}(\Delta x/H)$, evaluated for space-histories along the longitudinal centreline (as indicated in the diagram at the top of the figure) for the streamwise and spanwise fluctuating velocity components, for flow regimes **(a)** A **(b)** B and **(c)** C

Table 5.6 – Integral time and length scales evaluated from autocorrelation functions displayed in Figure 5.8

Flow Regime	Surface Velocity	Flow Depth	Integral Time Scales		Integral Length Scales				
	U_s (mm/s)	H (mm)	T_u (s)	T_v (s)	L_u (mm)	L_v (mm)	L_u/T_u (-)	$T_u U_s$ (mm)	L_u/H (-)
A	1508.4	5.1	0.025	0.018	38	28	1518	38	7
B	1111.8	7.0	0.034	0.028	39	31	1161	37	6
C	170.9	20.0	0.234	0.174	44	37	188	40	2

The spatial autocorrelation function evaluated for the longitudinal centreline (i.e. for the data-series at $u_i'(x,0,0)$) has also been plotted for the streamwise and spanwise velocities in Figure 5.8 for all regimes. The spatial autocorrelations represent an average over time and ensemble. The spatial delay, Δx, has been normalised by the flow depth for each regime.

The integral time (T_{u_i}) and length scales (L_{u_i}) have been estimated using the trapezoidal rule from the respective temporal and spatial autocorrelations plotted in Figure 5.8. These scales are given in Table 5.6.

Figure 5.8 indicates that $R_{u_i}(\tau U_s / H)$ and $R_{u_i}(\Delta x / H)$ decay relatively rapidly to zero for each flow regime. This indicates that the large-scale structures are correlated only for a short time delay, or spatial increment, after which they are broken down. Columns five and six of Table 5.6 indicate that the large-scale structures turnover faster for flow regimes A and B due to the higher Reynolds number for these flows relative to regime C. Figure 5.8 also indicates that when normalised by the flow velocity and depth, both the temporal, $R_{u_i}(\tau U_s / H)$, and spatial, $R_{u_i}(\Delta x / H)$, autocorrelations collapse for each regime. This is further verified by column eight of Table 5.6, which displays that when the integral length-scale, L_u, is divided by the integral time-scale, T_u, there is close agreement with the surface velocity, U_s. This indicates that Taylor's frozen turbulence hypothesis holds.

Further verification of Taylor's hypothesis can be evaluated by using the autocorrelation function to determine the propagation velocity of the large-scale turbulent structures relative to the bulk propagation of the flow field, as depicted in Figure 5.9. Figure 5.9a displays contour plots of the streamwise autocorrelation, $R_u(\Delta x, \tau)$, as a function of temporal, τ, and spatial delay, Δx, for each flow regime, as defined in Eq. (5.6). Data has been evaluated for the longitudinal centreline only (i.e. $y = 0$). The unevenness of the contour lines for flow regime A and B result from interpolation of the contours. In an effort to verify Taylor's frozen turbulence hypothesis, cross-sections through the

autocorrelation fields of Figure 5.9a are taken at 50*mm* offsets and plotted in Figure 5.9b. The temporal delay that corresponds to the peak autocorrelation for each curve in Figure 5.9b is evaluated and plotted against the spatial offset in Figure 5.9c. The points plotted in Figure 5.9c are compared with the bulk propagation of the flow field (U_s).

$$R_u(\Delta x,\tau)=\frac{\overline{u'(x,t)\,u'(x+\Delta x,t+\tau)}}{\sqrt{\overline{u'(x,t)^2}}\sqrt{\overline{u'(x+\Delta x,t+\tau)^2}}} \tag{5.6}$$

Taylor's hypothesis implies that advection of the flow field is a result of the bulk flow velocity and that turbulent motion does not contribute substantially to advection. This hypothesis holds for the flows considered in the present study, as Figure 5.9c indicates that the large-scale turbulent structures propagate at the velocity of the mean flow field, U_s. Furthermore, Figure 5.9c indicates that the

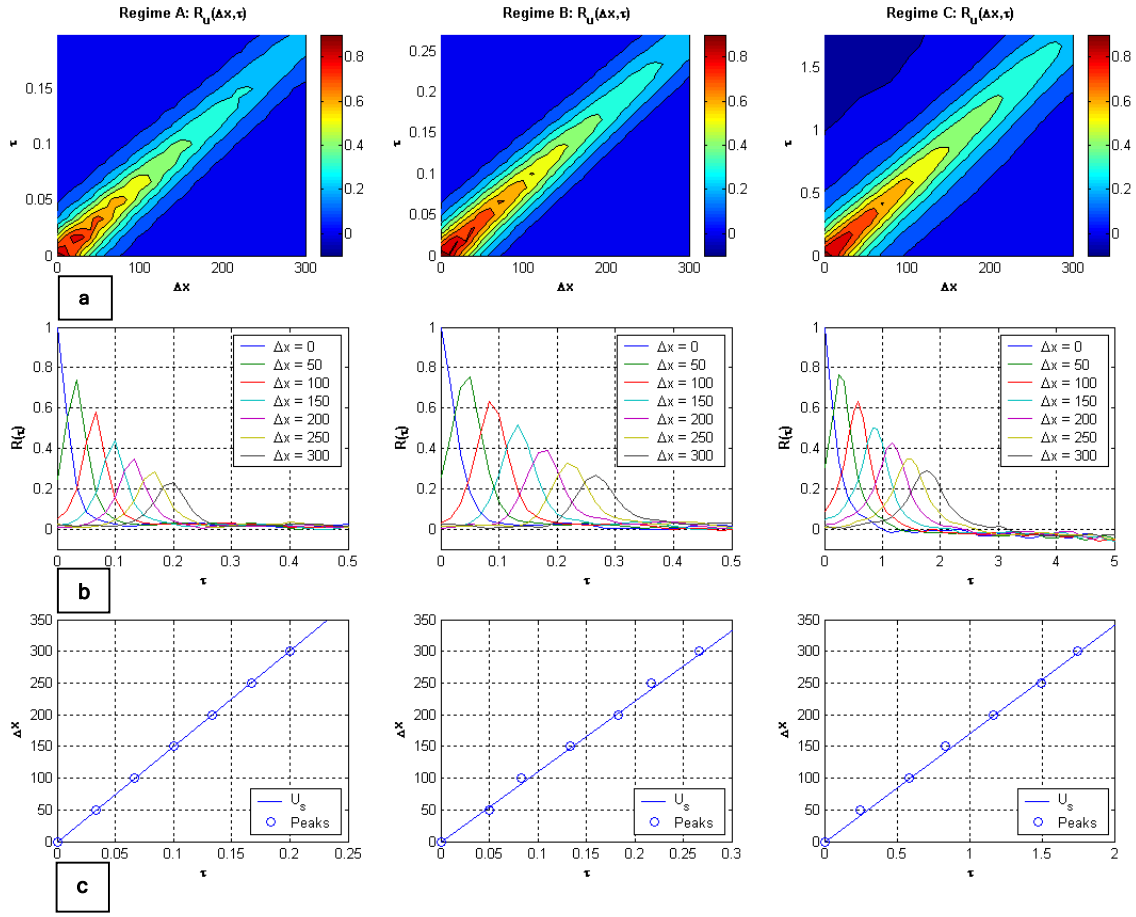

Figure 5.9 - **(a)** Autocorrelation as a function of temporal and spatial delay for flow regimes A, B and C **(b)** Temporal autocorrelation taken at 50mm offsets from the autocorrelation fields in (a) for regimes A, B and C **(c)** Peaks of the temporal autocorrelation at 50mm offsets plotted against the bulk propagation of the flow field (U_s) for regimes A, B and C.

turbulent structures sampled by the PP particles propagate at the free-surface velocity, U_s, and not the cross-sectional mean velocity, U_a.

Figure 5.10 displays the autocorrelation evaluated by v.Carmer (2005) using LDV, for a time-history in a shallow turbulent shear flow at a depth of $z/H = 0.68$. Comparing this data with that obtained at the free-surface in the present study (refer to Figure 5.8) reveals two distinct differences.

Firstly, the autocorrelation for the spanwise velocity, evaluated by v.Carmer (2005), decays much more rapidly than the streamwise velocity autocorrelation. This is attributed to the anisotropic structure of large-scale, sub-surface turbulence. 3D structures that burst from the turbulent boundary layer are stretched in the streamwise direction due to the direction of the mean flow field. This gives rise to hairpin vortices (Nezu & Nagakawa, 1993) that exhibit anisotropy at large wavenumbers (v.Carmer, 2005). However, the structures evaluated at the free-surface in the present study, are predominantly isotropic. This is reflected in the analogous decay of $R_u(\tau U_s/H)$ and $R_v(\tau U_s/H)$ (refer to Figure 5.8), and the length scales evaluated from the autocorrelations functions are approximately equivalent for both the transverse and longitudinal velocity components (cf. $L_u = 44mm \sim L_v = 37mm$ for regime C).

Secondly, Figure 5.10 indicates that the integral length scale evaluated at $z/H = 0.68$ in the streamwise direction ($L_u \approx \overline{U}T_u = 48mm$) is comparable with the flow depth ($H = 51.3mm$). If the results evaluated at the free-surface in the present study are correct, they are in contrast to those verified at z/H=0.68 by v.Carmer

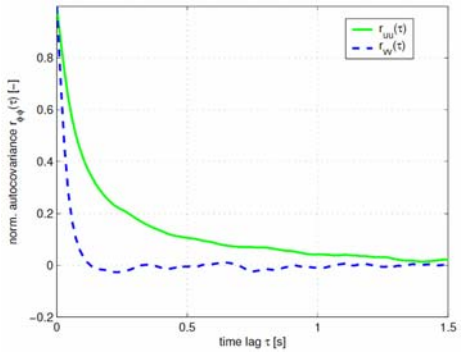

Figure 5.10 - Autocorrelation of streamwise and spanwise velocity components. Data gathered using LDV at a depth of z/H=0.68. Flow parameters: H=51.3mm, Re_H=12075, $\bar{U}_a$=235.4mm/s. Integral time scales: T_u=0.204s, T_v =0.034s. (v.Carmer, 2005)

(2005). At the free-surface turbulent structures are not restricted by the flow depth. Table 5.6 indicates that the integral length scales for both the streamwise and spanwise velocity are comparable for all regimes (i.e. ~35*mm*), and of scale greater than the depth as indicated in column ten of Table 5.6. This implies that the turbulent structures at the free-surface of the flow are not restricted by the flow depth, as is implied for sub-surface 3D turbulence. This finding is consistent with dye visualisation experiments and with the 2D spiral eddies identified by Kumar, et al (1998) at the free surface of a channel flow, which exhibited length scales larger than the flow depth. However it should be noted that the integral length scales evaluated in the present study border on the extent of structures that can be resolved by the PTV system. Therefore the current findings need to be verified with a higher resolution system, before conclusions can confidently be drawn.

5.4.3 Power Spectral Density

The data used to evaluate the autocorrelation functions have also been used to determine the one-dimensional power spectral density, S_{u_i}, for each flow. The power spectral density characterises the distribution of turbulent kinetic energy amongst the various length and time-scales of turbulence. The power-spectral density evaluated in the temporal domain, $S_{u_i}(f)$, for the respective streamwise and spanwise fluctuating velocity components are plotted in Figure 5.11a and Figure 5.11b. Each spectrum represents an ensemble average.

The spectra depicted in Figures 5.11a and 5.11b, exhibit a plateau in the low frequency region, after which a –5/3 power law is observed until the spectra terminates at the Nyquist frequency ($f_{Nyquist} = f_s / 2$, where f_s represents the sampling frequency).

The PSD evaluated in the frequency domain can be converted to the wavenumber domain, by applying Taylor's hypothesis (i.e. $k = 1/\lambda = f/U_s$). The temporal PSD estimates evaluated at the midpoint of the flow field (i.e. Figure 5.11a and 5.11b) converted to the wavenumber domain are displayed in Figure 5.11c for the fluctuating streamwise velocity and in Figure 5.11d for the fluctuating spanwise velocity component. Also plotted in Figures 5.11c and 5.11d are the PSD, evaluated in the spatial

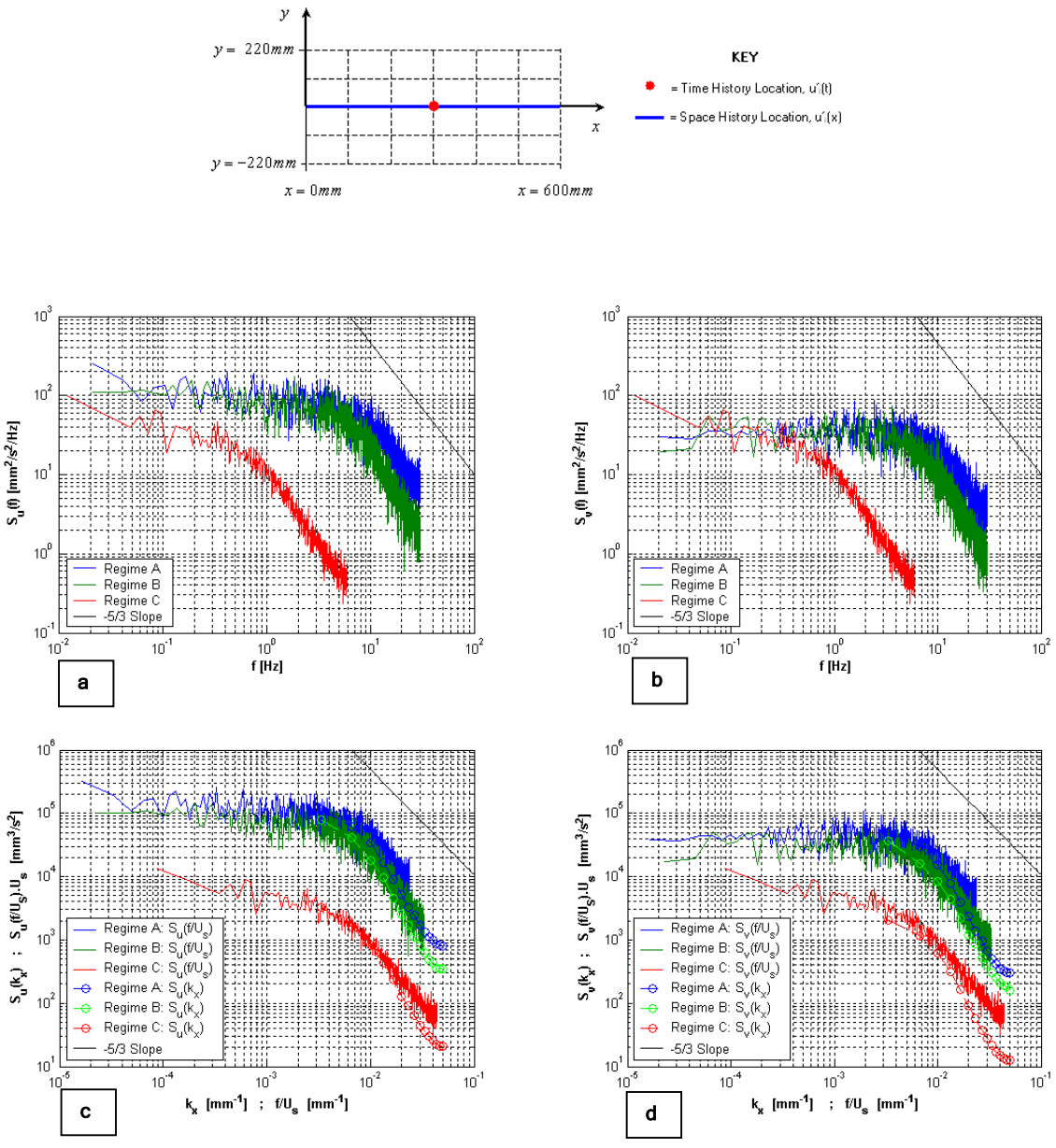

Figure 5.11 - Midpoint temporal power-density spectra, S(f), for the **(a)** streamwise and **(b)** spanwise fluctuating velocity components. The midpoint temporal power-density spectra converted to the wave-number, $S(f/U_s)$, domain has been plotted against and spatial power-density spectra evaluated along the axial line of the x-axis $S(k_x)$ for the **(c)** streamwise and **(d)** spanwise fluctuating velocity components.

domain, $S_{u_i}(k_x)$, for the streamwise and spanwise fluctuating velocity components evaluated along the longitudinal axis, for $y = 0$. Each $S_{u_i}(k_x)$ spectrum represents an average over time, for all runs. Less noise is evident in the spectra evaluated in the spatial domain, as a result of improved averaging.

The spectra evaluated in the spatial domain, $S_{u_i}(k_x)$ as depicted in Figures 5.11c and 5.11d, terminate at a value of $k = 5 \times 10^{-2} mm^{-1}$ which corresponds to the Nyquist wavenumber ($k_{Nyquist} = 1/2\Delta X_s$, where ΔX_s represents the sampling increment). A grid spacing of 10*mm* was used for the velocity interpolation process, however the resolution of the PTV system is only in the order of 30*mm*, as outlined in Section 4.3.2. Therefore the estimates of $S_{u_i}(k_x)$ are expected to be unreliable for wavenumbers greater than the resolution of the PTV system. This is evident in Figures 5.11c and 5.11d, which display that the spectra evaluated in the wavenumber domain depart from the spectra evaluated in the temporal domain at $k \approx 1 \times 10^{-2} mm^{-1}$. However, the spectra evaluated in the temporal domain follow Kolmogorov's –5/3 law to smaller scales implying that the spectra evaluated in the temporal domain is more robust at resolving information at higher wavenumbers. Furthermore, the PSD estimates in the spatial domain do not display the significant plateau region at low wavenumbers that is observed in $S_{u_i}(f/U_s)$. This is due to the limited extent of the data series in the spatial domain, which was not long enough to resolve information at low wavenumbers. In summary, the spectral estimates for data obtained in the spatial domain, are less reliable than the PSD evaluated in the temporal domain, due to the limited length of data available in the spatial domain, and the spatial resolution of the PTV system.

The PSD estimates, depicted in Figures 5.11c and 5.11d, display that the –5/3 law begins at a wavenumber of approximately $k = 7 \times 10^{-3}$ for all regimes. This corresponds to a length scale of $\ell \approx \mathrm{O}(k^{-1}) = 143mm$, which indicates that energy is contained at scales much greater than the flow depth for each regime.

The presence of energy in such large scales could stem from either an inverse energy cascade, in which energy is transferred from small-scales to large-scales, or via direct energy generation at large scales. However, it is unlikely that merging of vortices would occur in a shear flow, which by definition is dominated by 3D turbulence. Therefore possible mechanisms that could produce energy at scales much larger than the flow depth may be the formation of two-dimensional structures at the free surface (i.e. 2D spiral eddies as identified by Kumar, et al, 1998), flow inhomogeneity (i.e. secondary currents), horizontal shear introduced from the sidewalls, bed unevenness or flow interaction with the sluice gates. Again it should be reiterated that the spectral estimates presented in this section need to be verified with a higher resolution system before conclusions regarding the flow structure can be stated with assurance.

5.5 KEY FINDINGS

The previous sections presented results gathered at the surface of shallow, turbulent shear flows using a PTV system. The mean velocity profiles were predominantly homogeneous over the flow field, and the surface velocity evaluated by the PTV system compared well with the theoretical value predicted by the Blasius $1/7^{th}$ power law. However the PTV system provided estimates of turbulent intensity that were lower than the semi-empirical values stated by Nezu & Nagakawa (1993). This was primarily attributed to the limited spatial and temporal resolution of the PTV system.

The PDFs evaluated for the instantaneous velocity components were predominantly Gaussian. The autocorrelation functions evaluated for the longitudinal and transverse fluctuating velocity components indicated that Taylor's hypothesis for frozen turbulence holds for the flows considered in the present study. The integral length scales evaluated from the autocorrelation functions for both the streamwise and spanwise velocity components indicated predominantly isotropic structures at the free-surface, with length scales greater than the flow depth. Finally, the 1D power spectral density estimates for both the longitudinal and transverse velocity components displayed energy at scales much larger than the flow depth after which a -5/3 power was observed to high frequencies / wavenumbers.

6.0 Results II: Analysis of a Shallow Turbulent Wake Flow

This chapter presents and discusses results obtained from a shallow, turbulent wake flow generated in the laboratory. Section 6.1 outlines the experimental programme, and Section 6.2 provides a qualitative description of the wake visualised by dye injection. In Section 6.3, time-averaged fields are presented and discussed. Section 6.4 presents the probability density function, autocorrelation and power spectral density in order to obtain quantitative information regarding the flow structure. Finally, Section 6.5 considers the flow evolution in space, and Section 6.6 summaries the key experimental results.

6.1 EXPERIMENTAL PROGRAMME

In order to analyse the dynamics of quasi two-dimensional turbulent structures in shallow flows, a single isolated cylinder, with diameter greater than the flow depth, was introduced into a uniform, shallow shear flow. The resulting flow was a shallow, vortex street type wake and the purpose of analysing such a flow was to characterise the near and intermediate wake regions of a shallow VS wake flow by utilising time-averaged statistics, probability density functions (PDF), autocorrelation and power spectral density (PSD).

6.1.1 Experimental Regime

One circular cylinder constructed from smooth, steel pipe, with diameter 60.4*mm*, was used for all experimentation. Testing outlined in Appendix E indicated that cylinders of diameter greater than 60.4*mm* introduced significant secondary disturbances into the ambient flow, due to wake interaction with the flume boundaries. As a result cylinders with diameter greater than 60.4*mm* were not considered.

Table 6.1 - Ambient flow parameters for shallow turbulent wake experimentation

Cylinder Diameter	Flow Depth	Cylinder Diameter	Channel Slope	Mean Velocity	Shear Velocity	Friction Coefficient	Re_H	Re_D	Fr
D (mm)	H (mm)	D/H (-)	S (rad)	U_a (mm/s)	u_* (mm/s)	c_f (-)	(-)	(-)	(-)
60.4	20.0	3.0	0.0025	136.8	8.5	0.0077	2736	8262	0.31

The ambient flow conditions are summarised in Table 6.1, where *D* denotes the cylinder diameter and $\mathrm{Re}_D = U_a D/\upsilon$. Definitions for all other flow parameters listed in Table 6.1 are published in Section 5.1.1. The base flow was identical to the subcritical flow regime C (refer to Section 5.1.1).

It was initially intended to analyse the wake generated behind a cylinder introduced into the supercritical flows of regime A and B (refer to Section 5.1.1). However, as illustrated in Figure 6.1, the cylinder caused large disturbances to the free surface when introduced into a supercritical flow. Reflections from the uneven water surface and splashing from the wake meant that the polypropylene particles used for PTV were unable to be resolved for the supercritical flow regimes.

6.1.2 Coordinate System & PTV Measurement Window

The longitudinal distance downstream from the cylinder that could be analysed was constrained by the longitudinal extent of the flume and the effect of the backwater curve generated by the downstream sluice-gate. In order to increase the downstream distance available, the cylinder was placed in two locations on the channel bed. The first, position A, was situated on the centreline of the flume, 385*mm* from the leading edge of the channel bed (refer to Figure 6.2a). The second location, position B, was also situated on the centreline of the flume, but 685*mm* from the leading edge of the channel bed. The PTV window was centred about the midpoint of the channel bed and fixed for both cylinder positions. By separately analysing the wakes generated from placing the cylinders at positions A

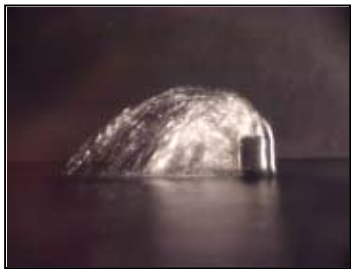

Figure 6.1- Wake resulting from a 20mm diameter cylinder placed in a shallow, supercritical flow

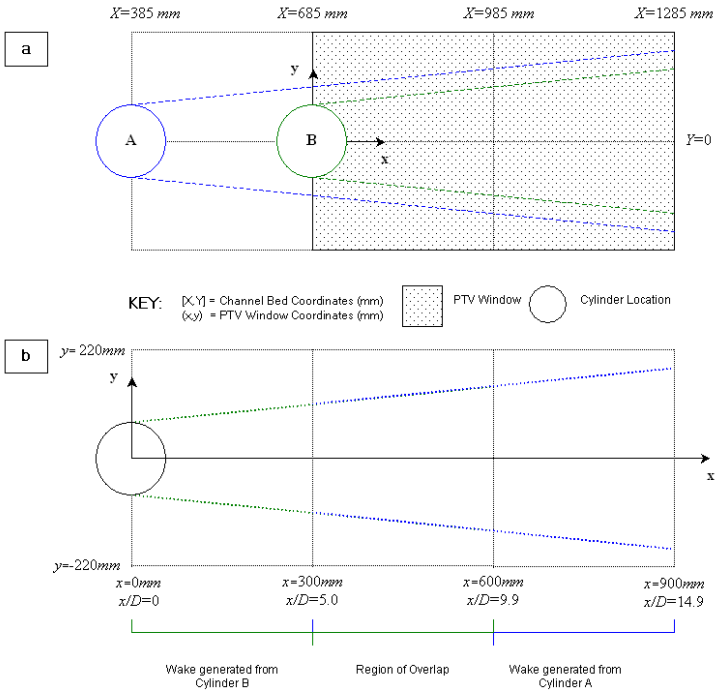

Figure 6.2 - **(a)** Illustration of the circular cylinder located at position A and B. The position and extent of the PTV window is depicted as the shaded area. **(b)** Illustration of the coordinate system and analysis window available by superimposing PTV data gathered from the cylinders located at positions A and B. Cylinder diameter = 60.4mm.

and B, the total measurement plane extended 900*mm* in the *x*-direction and ±220*mm* in the *y*-direction, with a 300*mm* overlap between the PTV analysis windows (refer to Figure 6.2b).

The inherent difficulty with using this method was that the turbulent boundary layer was not fully developed for the cylinder placed in position A. However testing outlined in Appendix F concluded that the large-scale instabilities, which were generated by the circular cylinder, reorganised the flow structure in the wake region irrespective of the boundary layer development. Therefore the mean-flow and turbulent statistics in the wake region were not significantly affected by using the experimental setup outlined in Figure 6.2.

As outlined in Section 3.4.3, v.Camer (2005) states that for a shallow wake flows, the transition between the near wake and intermediate wake region occurs at a distance of $x/\ell_M \approx 10$ to 20 from the midpoint of the circular cylinder (where ℓ_M is the integral wake length scale, $\ell_M = (\sqrt{\pi/8}HD)^{1/2}$).

This transition region corresponds to $x/D \sim 7$ for the VS wake generated in the present study, when using $x/\ell_M = 15$. Therefore analysis is restricted in the present study to the *near wake* region, i.e. $0 \le x/D \lesssim 7$, and the *intermediate wake* region, which extends over the portion of the PTV window that spans $7 \lesssim x/D \le 14.9$. It should be noted that these scales are order of magnitude estimates only. Due to the limited extent of the PTV analysis window analysis of the *far wake* region, in which large-scale structures have effectively disintegrated under the influence of bed friction, was unable to be observed.

6.1.3 Sampling Parameters

Twelve runs were completed for each cylinder position, resulting in 24 runs in total. Each flow was seeded with approximately 900 particles per frame and the frame rate was set at 20*Hz*. The sampling frequency was increased relative to flow regime C (refer to Section 5.1.2) due to the velocity gradients generated in the wake behind the circular cylinder. Eight hundred frames could be captured before particles amassing on the downstream sluice gate started to intrude to within 100*mm* of the PTV measurement window. This enabled a sampling duration of forty seconds, which as depicted in Figure 6.7b, captured approximately ten full shedding cycles of the vortex street wake. Such a time-period was sufficient to calculate meaningful time-averaged quantities. The time-averaged streamwise velocity, evaluated at the midpoint of the PTV window, deviated by a maximum of $\pm 1.25\%$ between the twelve experimental runs. This indicated that the experimental runs were repeatable, and ensemble averaging was viable.

6.2 VISUAL OBSERVATIONS

Figure 6.3 displays still frame images of the wake generated by the 60.4*mm* diameter cylinder, placed in a base flow with the hydraulic parameters listed in Table 6.1. The wake was observed to be a von Karman vortex-street, and this is reflected in the wake stability parameter: $S_{ws} = c_f D/H = 0.023$ (refer to Figure 3.7).

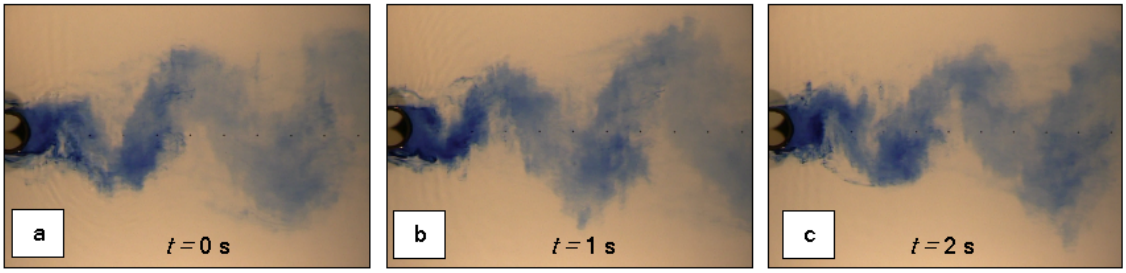

Figure 6.3 – Flow visualisation of the wake generated in the lee of a 60.4mm cylinder at time intervals of **(a)** zero seconds **(b)** one second and **(c)** two seconds. Flow depth H=20mm, D=60.4mm, S_{ws}=0.023. Each image has dimensions of approximately 550mmx450mm

Visual observations of the wake were consistent with the findings of v.Carmer (2005). Vortices were observed to periodically roll up in a re-circulation region that extended for approximately one cylinder diameter downstream from the midpoint of the circular cylinder. The vortices were subsequently swept downstream and rotated clockwise when shed from the top-side ($y > 0$) of the cylinder and counter-clockwise when shed from the bottom-side of the cylinder ($y < 0$). Furthermore, the wake was observed to spread laterally with distance downstream.

6.3 TIME-AVERAGED ANALYSIS

PTV provided three-dimensional arrays of streamwise and spanwise velocity at grid points located at 10*mm* node separation (refer to Figure 6.4). As described in Section 4.3.2.3, time-averaged fields were calculated using triangulation limits of 60*mm*. The following sections present and discuss the time-

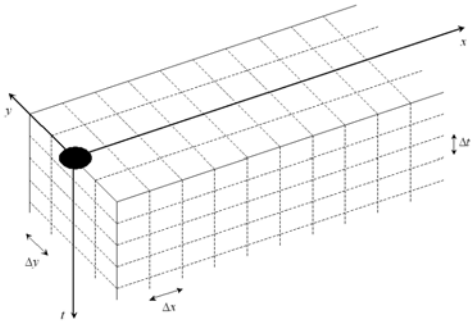

Figure 6.4 – Schematic visualisation of 3D vector field used for analysis of the wake generated behind a circular cylinder. The midpoint of the cylinder is located at x=0, y=0. The measurement field ranged from y/D=[-3.6 3.6] x/D=[0 14.9] and t/ Δt =[0 800]. Node spacing: Δx = 10mm, Δy = 10mm, Δt = 0.05s. Cylinder diameter: D=60.4mm.

averaged velocity and turbulent stress components in order to quantify and gain insight into the near wake and intermediate regions of a shallow vortex street flow.

Due to low particle seeding in the re-circulation zone, i.e. $x/D < 2$, this region is excluded from analysis. Furthermore, due to the effect of the backwater curve from the downstream sluice gate, data was only analysed for longitudinal distances of $x/D \leq 12$.

6.3.1 Time Averaged Fields

Figure 6.5a and 6.5b depict the time-averaged fields for the respective streamwise and spanwise velocity components, normalised by the free-stream surface velocity, U_s. The transverse and longitudinal axes have been normalised by the cylinder diameter, D. These fields have been generated for each run, by averaging the history of instantaneous velocity at each grid point over time. An ensemble average over twelve such fields is then evaluated. Furthermore, data obtained from cylinders located at positions A and B (refer to Figure 6.2) have been superimposed. Figure 6.5c and Figure 6.5d have been generated using a similar procedure, for the respective streamwise and spanwise turbulent intensity fields, normalised by the shear velocity, u_*. Finally, Figure 6.5e and 6.5f depict fields of turbulent kinetic energy, $0.5(\overline{u'u'} + \overline{v'v'})$, and the Reynolds stress component, $-\overline{u'v'}$. As previously mentioned, it is expected that velocity magnitudes are not correct in the re-circulation region, i.e. for $x/D \lesssim 2$, due to low particle densities. However the overall trends (or patterns) are expected to be correct, and therefore data ranging $x/D = 0$ to 2 has been included in this section.

Figure 6.5a displays the expected disturbed flow regions for a turbulent plane wake (refer to Figure 3.5). Two sidewise regions of disturbed and accelerated flow are apparent about the shoulders of the cylinder, and a velocity deficit is apparent in the wake region. Furthermore a region of low velocity (i.e. a re-circulation zone) and stagnation point is located immediately downstream of the cylinder. The time-averaged spanwise velocity field (Figure 6.5b) displays a region of negative transverse velocity at $[x/D \quad y/D] \approx [1.5 \quad 0.5]$ and a region of positive transverse velocity at

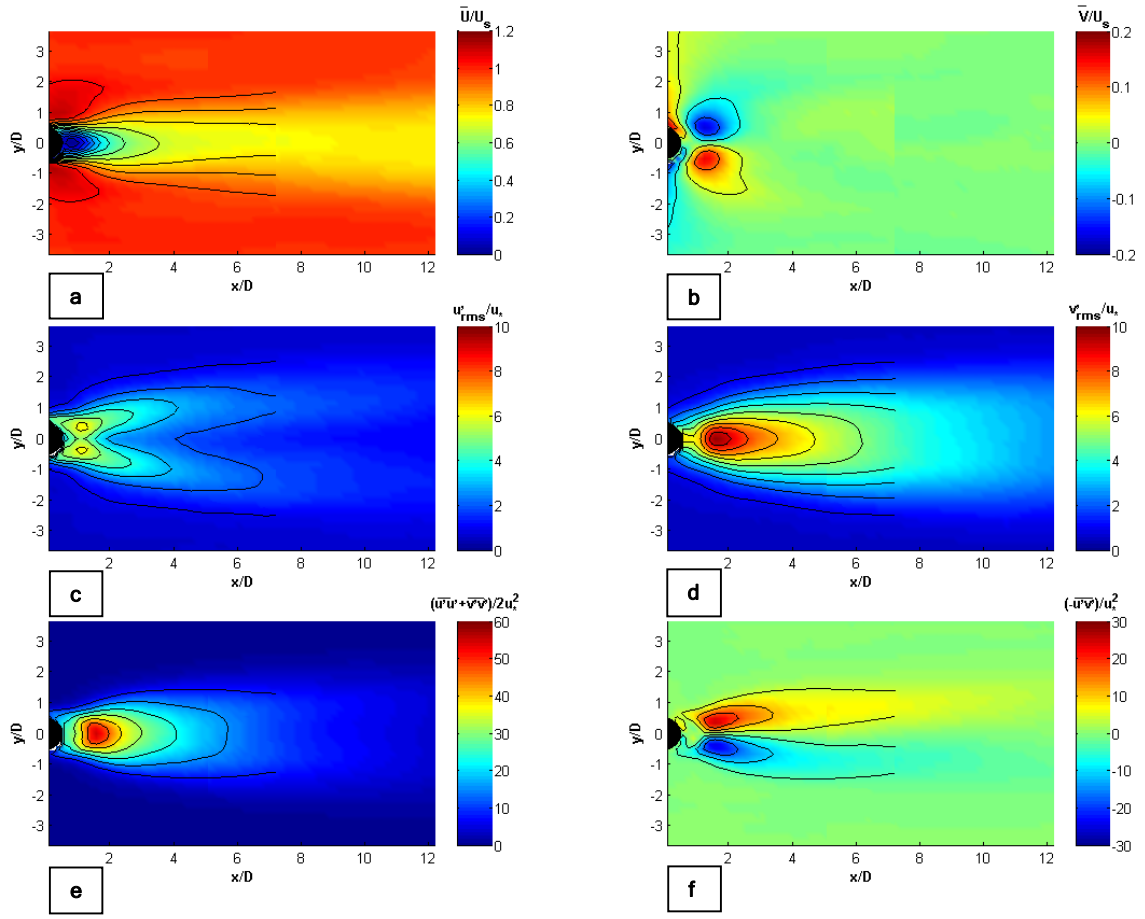

Figure 6.5 -Time and ensemble averaged fields for **(a)** $\overline{U}$ **(b)** $\overline{V}$ **(c)** u'_{rms} **(d)** v'_{rms} **(e)** TKE **(f)** $-\overline{u'v'}$. Data obtained from cylinders located at position A and B have been superimposed. Contours are depicted for data from the cylinder at position B only (refer to Figure 6.2b), at 0.1 intervals for (a) and (b); 1.0 intervals for (c) and (d); and intervals of 10 for (e) and (f).

$[x/D \quad y/D] \approx [1.5 \quad -0.5]$. These regions suggest the point at which the free shear layers are being alternately rolled up to form discrete large-scale 2D structures.

The streamwise turbulent intensity (Figure 6.5c) displays a double peak, whilst the spanwise turbulent intensity (Figure 6.5d) exhibits only one maximum located on the longitudinal centreline. These findings are in close agreement with the trends of streamwise and spanwise turbulent intensity evaluated by Akilli & Rockwell (2002) over the range $x/D = 0$ to 3.

The TKE field (Figure 6.5e) is dominated by fluctuations in the transverse velocity component, and it is clear that the majority of TKE is generated over the region $0 < x/D \lesssim 5$, due to the transverse shear

generated by the circular cylinder. The Reynolds stress (Figure 6.5f) is zero along the cylinder centreline, which demonstrates that u' and v' are not correlated for *y/D*=0. Furthermore the Reynolds stress displays absolute maximums for regions just downstream of the re-circulation region ($x/D \simeq 1.5$) where production of 2D turbulence is greatest due to the roll up of the shear layers into discrete vortices.

6.3.2 Time-Averaged Profiles

Figure 6.6a and 6.6b plot the respective mean velocity and turbulent intensity components evaluated along the cylinder centreline, $y/D = 0$. The ambient level of streamwise turbulent intensity evaluated from flow regime C (refer to Table 5.4) is plotted in Figure 6.6b for comparison. Figure 6.6c, 6.6.d, 6.6e and 6.6f plot cross-sections for the respective $\overline{U_i}$, $-\overline{u'v'}$, u'_{rms} and v'_{rms} components, at designated values of *x/D*.

Figure 6.6a shows that $\overline{U}$ increases towards the background surface velocity with increasing distance form the cylinder centreline, but appears to stabilise at approximately $0.8\overline{U}/U_s$. $\overline{V}$ is zero for all *x/D* due to cancellation of the periodic transverse velocity signal as a result of the averaging process (refer to Figure 6.7b).

The transverse profiles of $\overline{U}$ depicted in Figure 6.6c appear self-similar with respect to *x/D*. Indeed, Balachandar & Tachie (2001), and v.Carmer (2005) proved that the profiles of $\overline{U}(y/D)$ are independent of downstream position when normalised by the velocity deficit parameter, U^+, and half wake-width, y^+ (refer to Section 3.4.3 for definitions of these parameters). The time-averaged spanwise velocity profiles of Figure 6.6c, display a negative transverse velocity for *y/D*>0, whilst a positive transverse velocity is indicated for *y/D*<0. This characterises entrainment of ambient fluid into the wake.

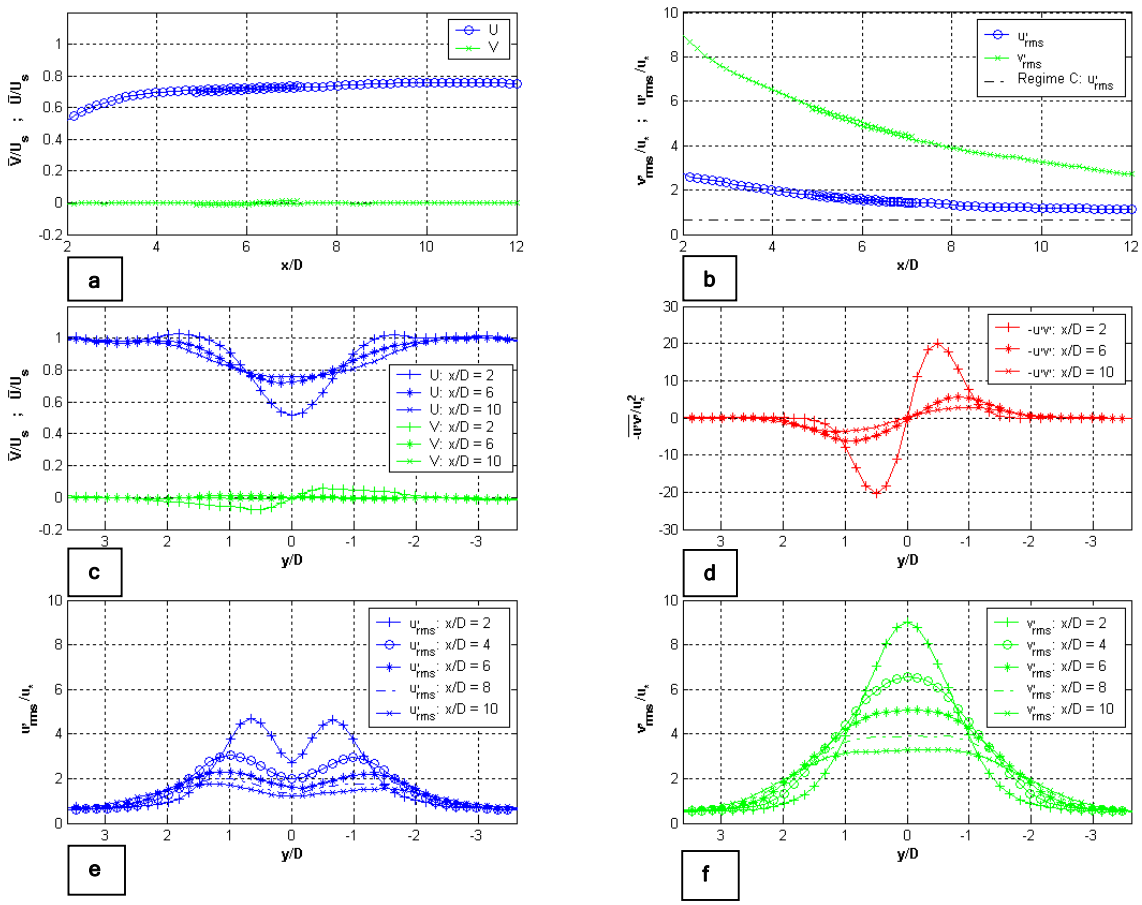

Figure 6.6 - **(a)** Centreline $\overline{U}$ and $\overline{V}$, normalised by U_s **(b)** Centreline u'_{rms} and v'_{rms}, normalised by the shear velocity **(c)** Cross-sections of $\overline{U}$ and $\overline{V}$, normalised by U_s, plotted for designated values of x/D. Cross-sections of **(d)** $-\overline{u'v'}$ **(e)** u'_{rms} and **(f)** v'_{rms}, normalised by the shear velocity, plotted for designated values of x/D.

Figure 6.6b indicates that there is strong anisotropy between the turbulent intensity components. The spanwise turbulent intensity is approximately three times greater than the streamwise intensity at $x/D = 2$, which is directly comparable to the magnitude of $v'_{rms}/u'_{rms} = 3$ evaluated by v.Carmer (2005) for a shallow VS flow with $S_{ws} = 0.07$, at $x/D = 2$. The streamwise intensity decays much more rapidly than the spanwise intensity, however both are expected to reach the ambient level of turbulent intensity far downstream, as the large 2D coherent structures (2DCS) are stabilised by the effects of bed friction. Figure 6.6e displays a double peak in the streamwise turbulent intensity measured at transverse locations across the wake. The transverse profiles of both turbulent intensity components also appear to be self-similar with respect to the downstream position.

The Reynolds stress component, $-\overline{u'v'}$, represents transport of momentum by turbulence, and is depicted in Figure 6.6d. This figure is consistent with Figure 6.5f, in which $-\overline{u'v'} = 0$ for the cylinder centreline, and absolute maximums are displayed in regions where alternately rotating streets of 2DCS propagate above and below the cylinder centreline. Figure 6.6d displays that the rate of decay of $-\overline{u'v'}$ is greatly diminished over the region *x/D*=6 to 10. This indicates that the near field is characterised by a strong exchange of momentum between the mean flow and 2D turbulence. However, in the intermediate field of the wake, the 2D turbulence has effectively stabilised but is still gradually decaying under the influence of bed friction.

6.4 TIME-HISTORY ANALYSIS

The features outlined in Section 6.3 are evident only from the averaging process, and are not indicative of the instantaneous flow. The following sections present and discuss the probability density function (PDF), autocorrelation function and power spectral density (PSD), in order to provide a quantitative description of the evolution of flow structure over time. As outlined in Section 4.3.2.3, for time-history analysis, no limits were set on the interpolation triangles in order to provide a continuous time-series.

6.4.1 Raw Velocity Signals

Figure 6.7a and 6.7b depict the respective streamwise and spanwise velocity signals evaluated at $x/D = 5$, $y/D = 0$ for Run C3B10 (where C3 denotes a cylinder of diameter three times the flow depth, B denotes the cylinder location, refer to Figure 6.2, and the numeral 10 denotes the tenth experimental run out of twelve). Each time-history contained 800 frames (i.e. a 40 second sampling interval) and the average for each time-history is plotted as a dashed line. These figures provide an indication of the raw time-histories evaluated at a point in a shallow vortex street wake.

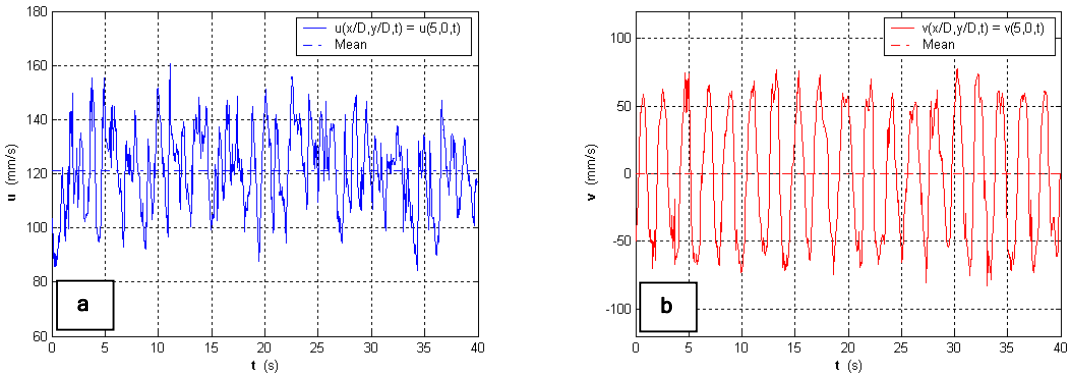

Figure 6.7 -Time histories for the **(a)** streamwise and **(b)** spanwise velocity evaluated at x/D=5, y/D=0 for RunC3B10. Sampling frequency = 20 Hz.

In Figure 6.7b strong, low frequency, oscillations about a mean value of zero are present for the spanwise velocity component. This strong periodic signal is characteristic of the cyclic vortex shedding process, displayed in Figure 6.3. Approximately ten full shedding cycles are captured over the forty-second sampling interval (where one full cycle accounts for the shedding of two counter-rotating vortices).

6.4.2 Probability Density Functions

The following sections provide information on how the probability density function (PDF) for instantaneous streamwise and spanwise velocity changes with respect to position in the wake of a shallow VS flow.

6.4.2.1 Centreline Profiles

Figure 6.8a and 6.8b depict the probability density functions for the respective standardised streamwise and spanwise velocity components ($\hat{u}_i = (u_i - \overline{U_i})/\sigma_{u_i}$) evaluated for time-histories at points along the cylinder centreline. These figures are plotted as 2D surfaces where the *x*-axis denotes the longitudinal coordinate normalised by the cylinder diameter (x/D) and the *y*-axis denotes the standardised velocity component, $\hat{u}_i$. The accent, ^, has been dropped for convenience in Figure 6.8. The *z*-axis denotes the probability of the standardised instantaneous velocity, $p(\hat{u}_i)$. Each field represents an ensemble average. Cross-sections through the fields of Figure 6.8a and 6.8b at various

locations of x/D are displayed in Figure 6.8c and 6.8d respectively. Finally, the skewness and flatness for the streamwise and spanwise velocity are depicted in Figure 6.8e and 6.8f respectively as a function of *x/D*.

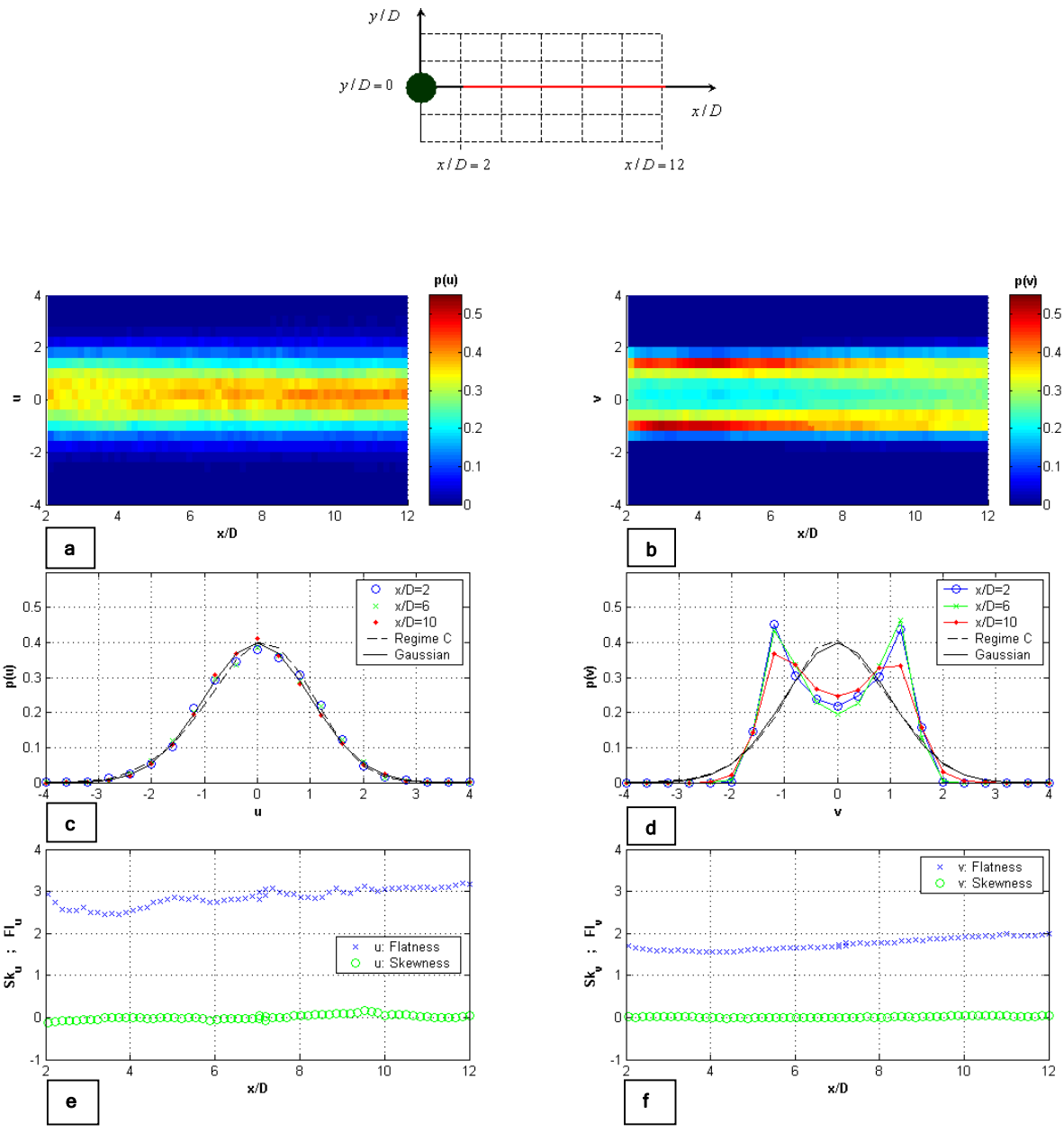

Figure 6.8 - PDF fields evaluated for time-histories at points along the cylinder centreline (i.e. y/D=0, x/D=2 to 12, as indicated in the diagram at the top of the figure) for the standardised **(a)** streamwise velocity and **(b)** spanwise velocity. Cross-sections taken through the PDF fields are displayed for the streamwise velocity in **(c)** and for the spanwise velocity in **(d)** for designated values of x/D. The skewness and flatness of the PDFs are displayed in **(e)** for the streamwise velocity and in **(f)** for the spanwise velocity. The PDF for the case of no topographical forcing (regime C) is also plotted in (c) and (d).

The double peak and flatness of less than three, displayed in the PDF for the spanwise velocity component (refer to Figure 6.8d and 6.8f) is characteristic of a strong periodic signal (Bendat & Piersol, 2000). Such periodicity is introduced from the cyclic shedding of 2DCS in the lee of the circular cylinder. A periodic signal is absent in the PDF for the streamwise velocity component, which is predominantly Gaussian when evaluated along the cylinder centreline (refer to Figure 6.8a and 6.8c). Figure 6.8e indicates that the PDF for the streamwise velocity component approaches the background flatness of $Fl = 3.2$, evaluated from flow regime C (refer to Table 5.2), with increasing distance downstream. The skewness for both the longitudinal and transverse components is effectively zero over the range $2 < x/D < 12$, for data evaluated along cylinder centreline.

Interestingly, Figure 6.8b and 6.8d displays that $p(\hat{v})$ is approximately uniform over the range *x/D*=2 to 7, which corresponds to the near wake region as defined by the integral wake length scale (refer to Section 3.4.3). However, Figure 6.8b displays that for $x/D \gtrsim 7$ the PDF for the spanwise velocity component displays a strong double peak, but the peaks decay with *x/D*. This indicates that the strong modulation in the spanwise velocity signal is increasingly damped for $x/D \gtrsim 7$. Therefore this region, i.e. $x/D \gtrsim 7$, represents the intermediate wake field, in which the presence of 2DCS dominate the flow, but their rates of growth are diminished by the effects of bed friction. It is expected that for large distances downstream, $p(\hat{v})$ would become Gaussian as the 2DCS are dissipated and random 3D turbulence dominants.

6.4.2.2 Transverse Profiles

Figure 6.9a displays the PDF for time-histories of standardised *streamwise* velocity evaluated at points along the *y*-axis at locations of $x/D = [2 \quad 6 \quad 10]$. Cross-sections are taken through the PDF fields of Figure 6.9a are at locations of $y/D = [0 \quad 1.5 \quad 3]$, and depicted in Figure 6.9b. Figure 6.9c displays the skewness and flatness distributions along the y-axis at locations of $x/D = [2 \quad 6 \quad 10]$. Figure 6.10 plots the PDF for the standardised *spanwise* velocity in the same form as Figure 6.9.

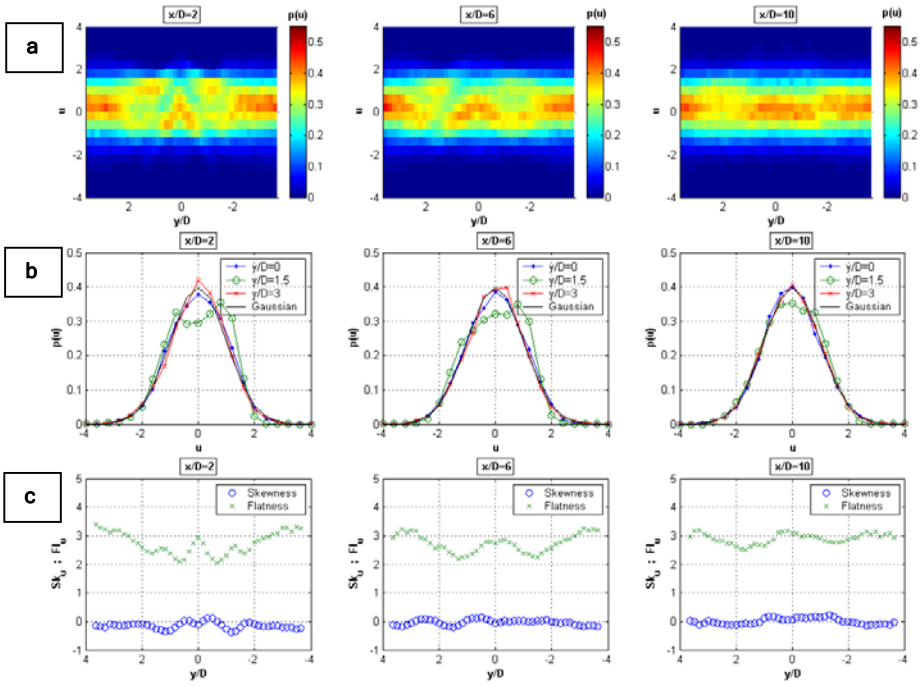

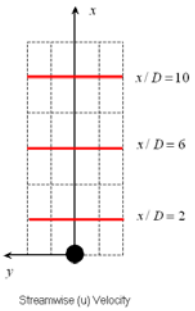

Figure 6.9 - **(a)** PDF fields of the standardised streamwise velocity evaluated for time-histories at points along the y-axis at locations of x/D=2, x/D=6 and x/D=10. **(b)** Cross-sections are taken through the PDF fields of (a) for designated values of y/D. **(c)** Skewness and flatness distributions along the y-axis at locations of x/D=2, x/D=6 and x/D=10.

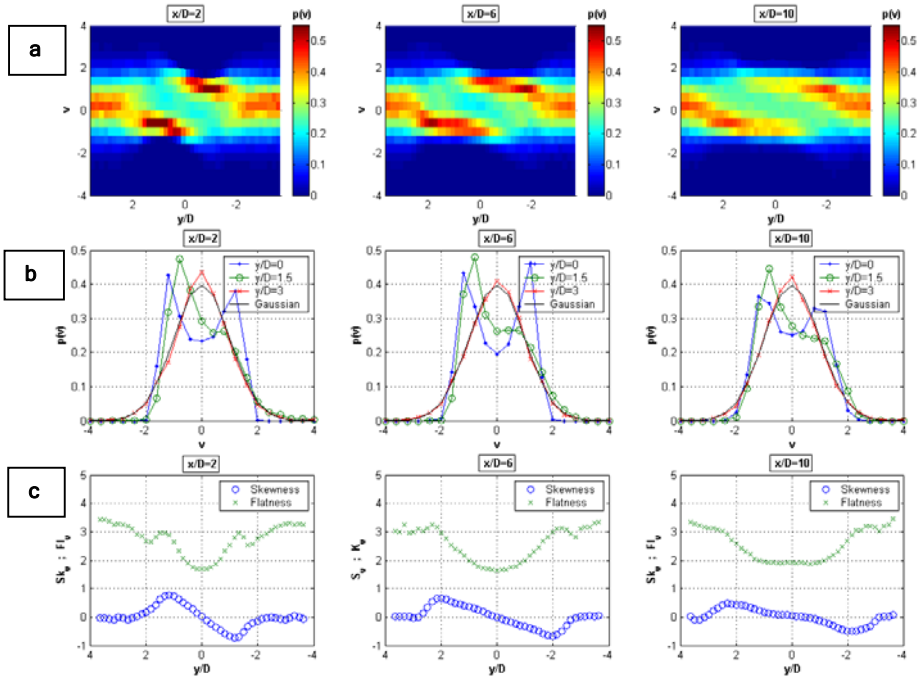

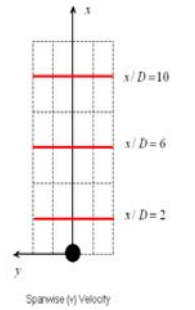

Figure 6.10 - **(a)** PDF fields of the standardised spanwise velocity evaluated for time-histories at points along the y-axis at locations of x/D=2, x/D=6 and x/D=10. **(b)** Cross-sections are taken through the PDF fields of (a) for designated values of y/D. **(c)** Skewness and flatness distributions along the y-axis at locations of x/D=2, x/D=6 and x/D=10.

The PDF for the longitudinal velocity component, depicted in Figure 6.9a and 6.9b, is predominantly Gaussian for the cylinder centreline, as described in Section 6.4.2.1, and also in regions outside of the disturbed wake region (i.e. for $-3 \lesssim y/D \lesssim 3$). These findings suggest that for *y/D*=0 the cancelling effect of the alternately rotating eddies above and below the cylinder centreline result in a predominantly Gaussian distribution of $p(\hat{u})$. However for regions aside from *y/D*=0, Figure 6.9c indicates that $p(\hat{u})$ is non-Gaussian and is characterised by asymmetry and a flatness of less than three. This indicates that aside from *y/D*=0, periodicity is introduced into the streamwise velocity signal as a result of the propagating street of alternately rotating 2D structures.

Figure 6.10a and 6.10b depict that $p(\hat{v})$ resembles a Gaussian distribution for regions outside the disturbed wake region (i.e. for $-3 \lesssim y/D \lesssim 3$), where random 3D turbulence dominates. For the cylinder centreline a double peak is evident in $p(\hat{v})$, as described in Section 6.4.2.1. However strong asymmetry is evident in the PDF for the spanwise velocity component for regions aside from *y/D*=0 (refer to Figure 6.10c). Figure 6.10c, indicates that for *y/D*>0, the PDF is positively skewed, and negatively skewed for *y/D*<0. This finding also indicates the presence of a counter-rotating street of vortical structures that propagate above and below the cylinder centreline.

6.4.3 Autocorrelation

The autocorrelation provides information on large-scale turbulent structures, and is evaluated for the fluctuating velocity components in the following sections. Section 6.4.3.1 considers the temporal autocorrelation function evaluated on the cylinder centreline and Section 6.4.3.1 considers the autocorrelation function at transverse cross-sections through the wake field.

6.4.3.1 Centreline Profiles

Figure 6.11a and 6.11b depict the autocorrelation function evaluated for time-histories at points along the cylinder centreline, $y/D = 0$, for the streamwise and spanwise velocity respectively. These figures are plotted two-dimensional surface plots, where the *x*-axis denotes the longitudinal coordinate

normalised by the cylinder diameter (x/D) the *y*-axis the autocorrelation lag (τ) and the *z*-axis the autocorrelation coefficient ($R_{u_i}(\tau)$). Each figure represents an ensemble average, and data from cylinders setup at position A and B are superimposed. Figure 6.11c and 6.11d depict cross-sections taken through the fields of 6.11a and 6.11b at specified values of x/D. The autocorrelation function evaluated for flow regime C (i.e. for the case of no topographical forcing, refer to Section 5.4.2) is plotted for comparison in Figures 6.11c and 6.11d.

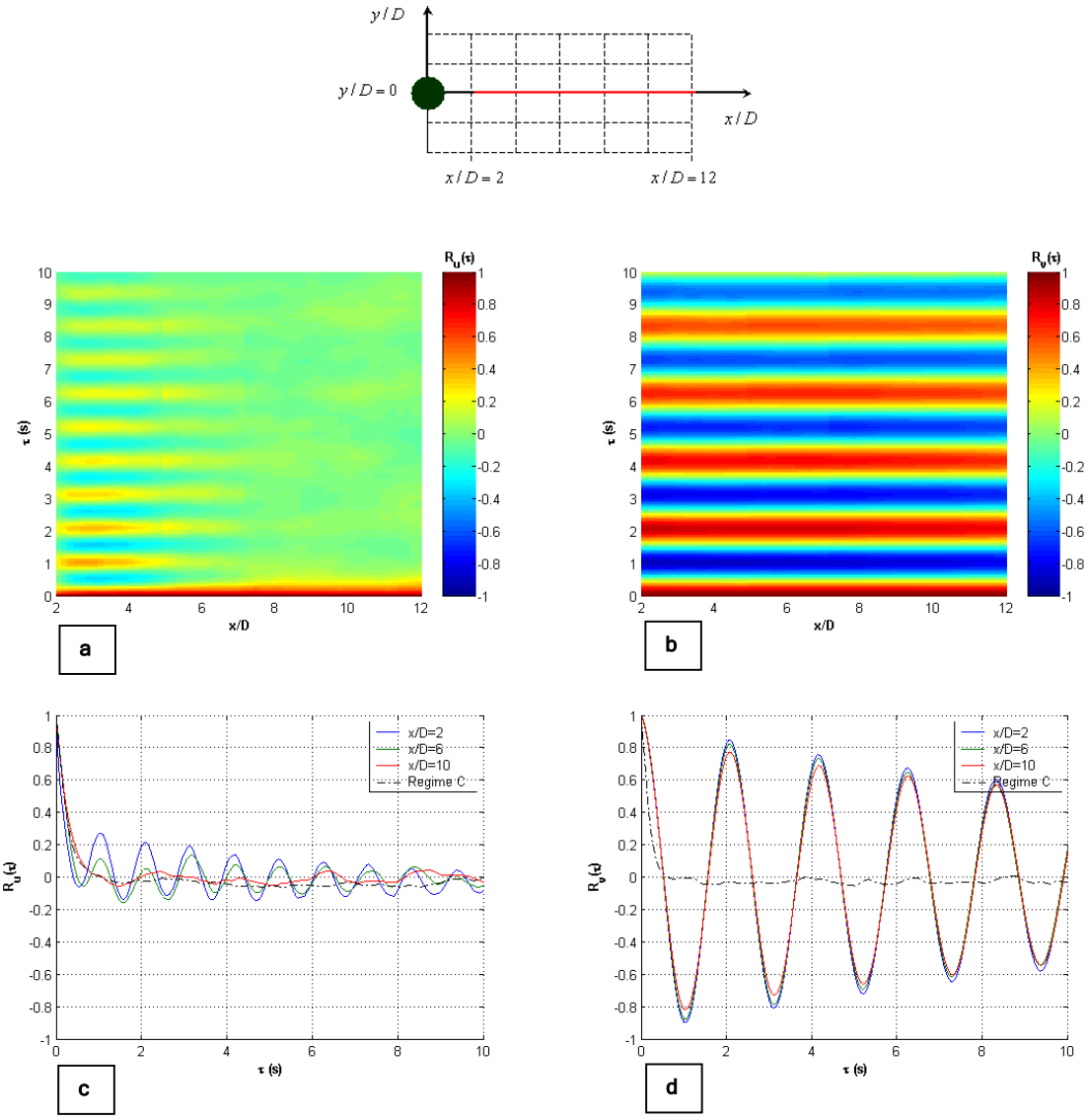

Figure 6.11 – Autocorrelation field evaluated for points along the cylinder centreline (as depicted in the diagram at the top of the figure) for the instantaneous **(a)** streamwise velocity and **(b)** spanwise velocity. Cross-sections taken through the autocorrelation fields are displayed for the streamwise velocity in **(c)** and for the spanwise velocity in **(d)** for designated values of x/D. The autocorrelation for the case of no topographical forcing (Scenario C) is also plotted in (c) and (d).

Figure 6.11b and 6.11d indicate that the transverse autocorrelation, $R_v(\tau)$, displays strong periodicity for all x/D. This modulation characterises the oscillatory motion of the wake generated behind the circular cylinder. The streamwise velocity autocorrelation, $R_u(\tau)$, is initially periodic but with a lower correlation coefficient relative to the transverse case. This indicates that, for *y/D*=0, there is more energy contained in the transverse fluctuations. The streamwise autocorrelation is rapidly damped with increasing x/D (refer to Figure 6.11c), and the frequency of the oscillations is approximately double that of the transverse case. These findings are consistent with autocorrelation functions evaluated along the cylinder centreline by v.Carmer (2005) for a shallow vortex-street flow.

6.4.3.2 Transverse Profiles

Figure 6.12a displays the *streamwise* autocorrelation evaluated for time-histories at points along the *y*-axis, at locations of $x/D = [2 \quad 6 \quad 10]$. Each field represents an ensemble average over twelve runs. Cross-sections have been taken through the fields of Figure 6.12a at designated values of *y/D* and plotted in Figure 6.12b, assuming that the fields plotted in 6.12a are symmetrical about *y/D*=0. The autocorrelation for the *spanwise* velocity component is displayed similarly in Figure 6.13.

The streamwise autocorrelation, $R_u(\tau)$ evaluated for the cylinder centreline (refer to Figure 6.12a and 6.12b) corresponds to the findings in Section 6.4.3.1, in which the centreline autocorrelation oscillates at a frequency that corresponds to twice the frequency of the spanwise autocorrelation. However, away from the cylinder centreline, e.g. *y/D=1*, there is strong correlation in the longitudinal velocity component, that oscillates with the same frequency as $R_v(\tau)$. It is assumed that along the cylinder centreline, coherence in the streamwise velocity signal is damped due to interference from to the counter-rotating street of vortices shed above and below *y/D*=0. However for regions aside from the cylinder centreline, $-0.5 < y/D < 0.5$, coherent structures with the same sense of rotation are free to propagate downstream, without interference. This finding is reaffirmed in the strong correlation between u and v for $-0.5 \gtrsim y/D \gtrsim 0.5$, and the rapid decay of $R_u(\tau)$ for *y/D*=0.

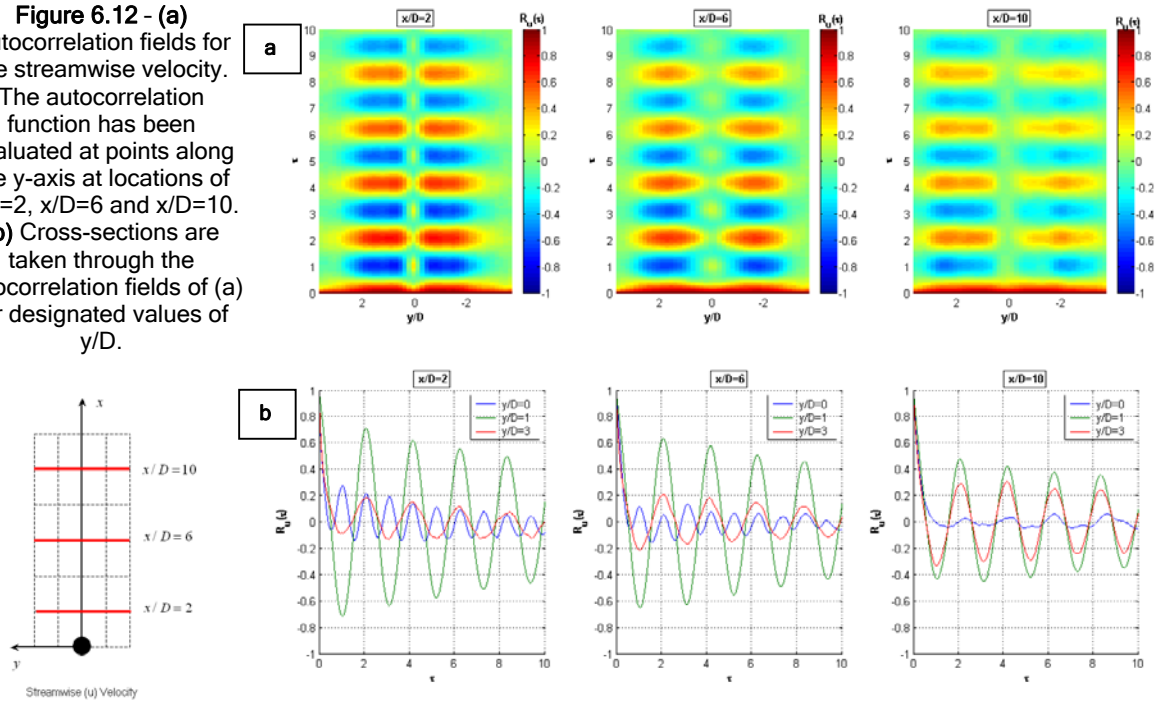

Figure 6.12 - (a) Autocorrelation fields for the streamwise velocity. The autocorrelation function has been evaluated at points along the y-axis at locations of x/D=2, x/D=6 and x/D=10. **(b)** Cross-sections are taken through the autocorrelation fields of (a) for designated values of y/D.

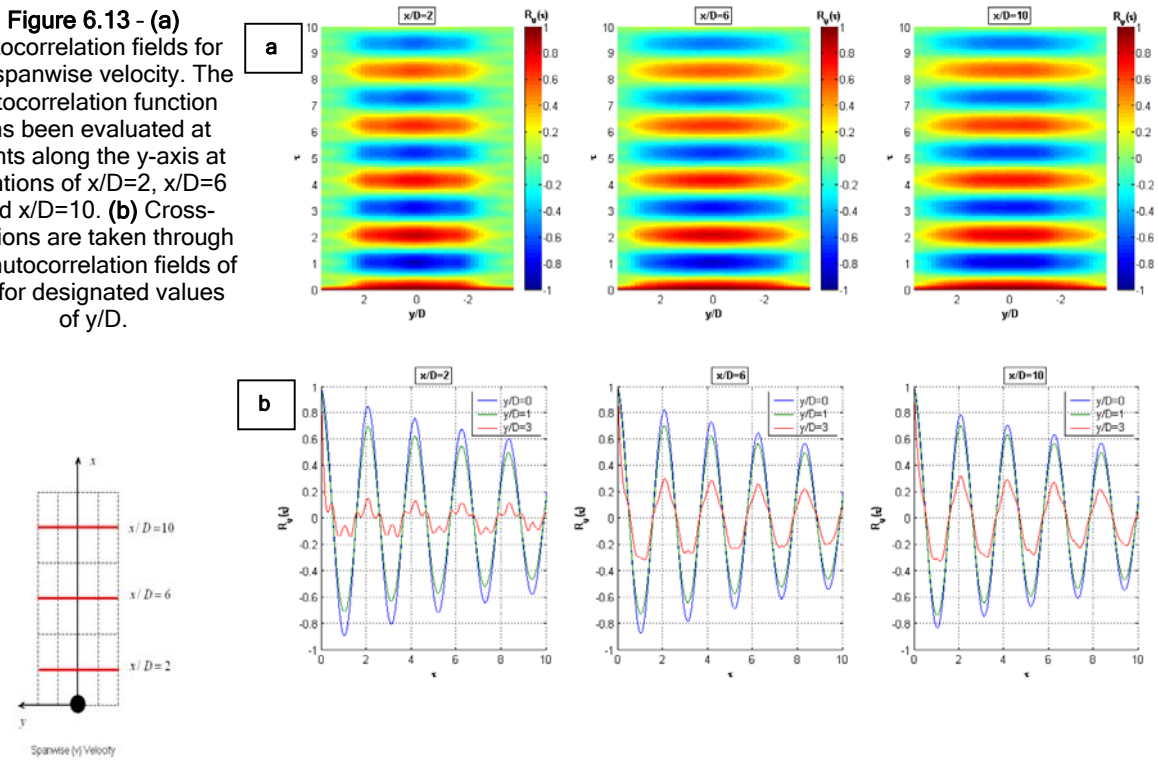

Figure 6.13 - (a) Autocorrelation fields for the spanwise velocity. The autocorrelation function has been evaluated at points along the y-axis at locations of x/D=2, x/D=6 and x/D=10. **(b)** Cross-sections are taken through the autocorrelation fields of (a) for designated values of y/D.

$R_v(\tau)$ is strongly correlated for all *y/D* within the extent of the wake (i.e. for $-3 \lesssim y/D \lesssim 3$). This suggests that the strong sweeping motion of the wake in the lateral direction dominates the transverse velocity signal. Furthermore the transverse extent over which there is strong periodicity in $R_v(\tau)$ increases with *x/D*. This indicates that the large-scale structures are increasing laterally with distance downstream.

6.4.4 Power Spectral Density

The power spectral density (PSD) is used to provide information on the energy composition of the various scales that make up turbulent motion. In the following sections the PSD is estimated for the fluctuating transverse and longitudinal velocity components at various locations in the shallow VS wake.

6.4.4.1 Centreline Profiles

Figures 6.14a and 6.14b depict the PSD evaluated for time-histories at points along the cylinder centreline ($y/D = 0$) for the longitudinal and transverse velocity components respectively. These figures are also plotted as two-dimensional surface plots, with the *x*-axis representing the longitudinal coordinate normalised by the cylinder diameter, x/D, the *y*-axis the Strouhal number, $St = fD/U_a$, and the *z*-axis the natural logarithm of the power spectral density, $\log_e(S_{u_i})$. Figure 6.14c and 6.14d depict cross-sections taken through the fields of 6.14a and 6.14b at specified values of x/D. Also plotted in Figures 6.14c and 6.14d are the background PSD for the ambient flow (i.e. flow regime C as described in Section 5.1) as well as the theoretical -5/3 and –3 power laws that characterise the respective cascade of 3D and 2D turbulence to small scales (refer to Figure 3.3).

The PSD for the transverse velocity component (refer to Figures 6.14b and 6.14d) is characterised by a pronounced peak at a Strouhal number of 0.21, which is in agreement with the Strouhal number evaluated by v.Carmer (2005) for a shallow VS wake. This peak characterises the frequency at which 2DCS are cyclically shed from the cylinder. The peak energy level decays with increasing x/D, implying that the energy contained in the 2DCS is dissipating with distance downstream. This also

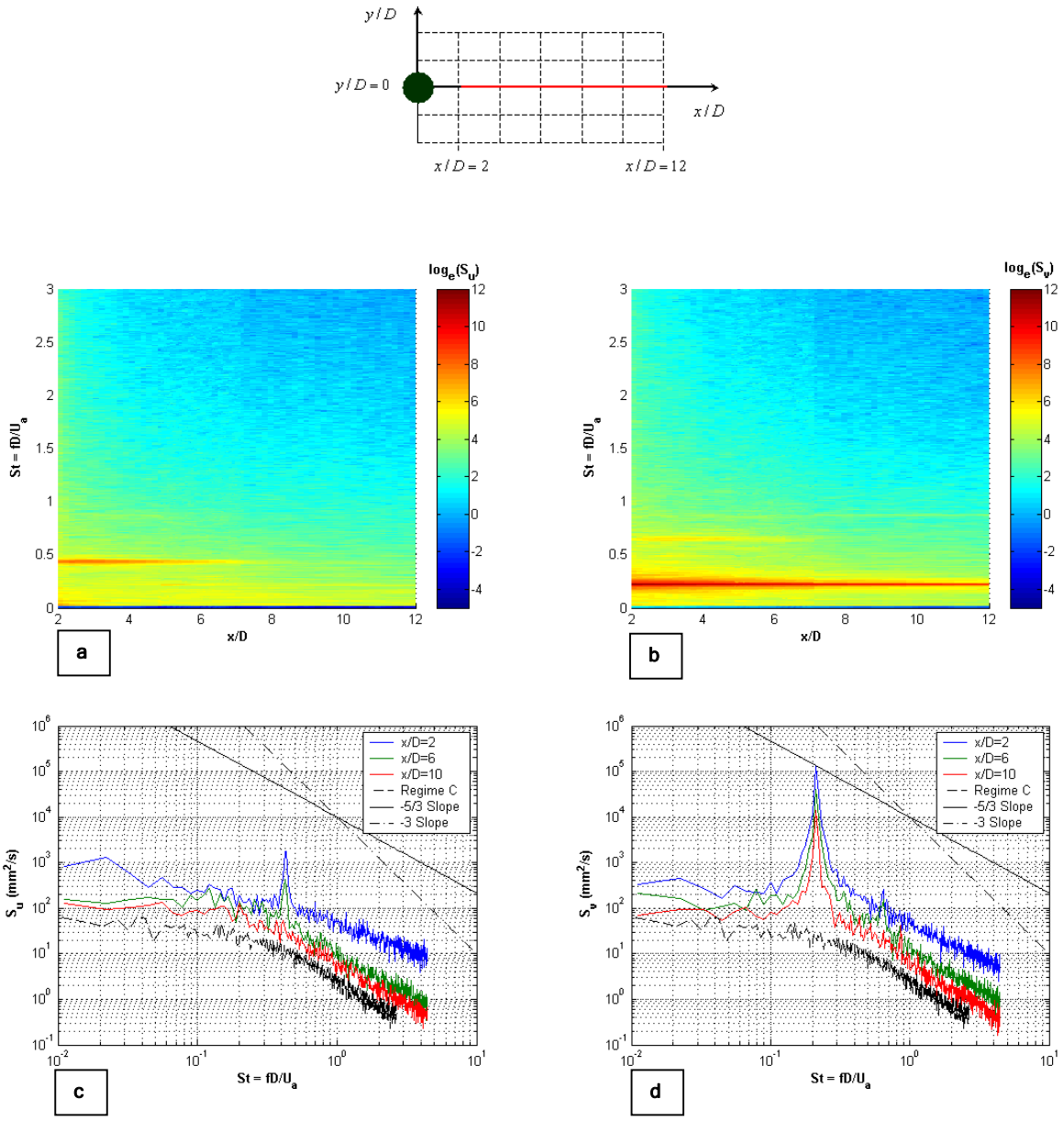

Figure 6.14 - Power spectral density fields evaluated for time-histories points along the cylinder centreline (as depicted in the diagram at the top of the figure) for the instantaneous **(a)** streamwise velocity and **(b)** spanwise velocity. Cross-sections taken through the PSD fields are displayed for the streamwise velocity in **(c)** and for the spanwise velocity in **(d)** for designated values of x/D. The PSD for the case of no topographical forcing (Scenario C) is also plotted in (c) and (d).

suggests that transfer of energy into the 2DCS (i.e. an inverse energy cascade) is absent. Indeed, v.Carmer (2005) concluded that for shallow VS wakes, neighbouring vortices with the same sense of rotation are separated by regions of ambient fluid entrainment, effectively preventing any merging of vortices. Furthermore, the entire PSD distributions, depicted in Figures 6.14c and 6.14d, are observed to decrease towards the ambient level with increasing *x/D*. This reaffirms that energy, generated due to lateral shear induced by the circular cylinder, is being dissipated with increasing downstream distance.

The PSD for the longitudinal velocity component (refer to Figures 6.14a and 6.14c) displays a peak at $St = 0.43$, which decays at approximately *x/D*=7. The peak in S_u corresponds to a frequency of approximately twice the dominant Strouhal number of 0.21 depicted in the spanwise PSD distribution. This finding is consistent with the periodicity of the streamwise autocorrelation evaluated along the cylinder centreline (refer to Section 6.5.3.1). A secondary peak in the PSD estimate for the spanwise velocity component is observed in Figure 6.14b. This peak corresponds to $St \simeq 0.65$ and also decays at approximately *x/D*=7. This peak was also displayed in the PSD estimate of v.Carmer (2005) for a shallow VS flow measured at *x/D*=2, refer to Figure 3.8.

It is postulated that the peaks only evident between $2 \lesssim x/D \lesssim 7$, are characteristic of the highly disturbed flow in the near wake region, which was estimated to extend over a longitudinal distance of $0 \lesssim x/D \lesssim 7$ (refer to Section 6.1.2). However for $x/D \gtrsim 7$ the wake is characterised only by a Strouhal number of 0.21 evident in S_v. This suggests that for $x/D \gtrsim 7$ the wake has partially stabilised and is characteristic of the intermediate wake region identified by v.Carmer (2005). In this region 2DCS are predominant, but these structures decay with downstream distances due to the dissipative effects of bed friction.

A –5/3 law to high frequencies is observed in both Figure 6.14c and 6.14d, implying energy dissipation via a vertically sheared 3D turbulence. However for $x/D = 2$ the –5/3 law is not as

definitive and a –1 law is observed for S_u. This suggests that Kolmogorovs's –5/3 law may not hold for the highly disturbed flow close to the circular cylinder, i.e. for $x/D \lesssim 2$.

6.4.4.2 Transverse Profiles

Figure 6.15a displays the power spectral density for the time-history of the *streamwise* velocity evaluated at points along the *y*-axis at locations of $x/D = [2 \quad 6 \quad 10]$. Figure 6.15b plots cross-sections through the fields of Figure 6.15a at locations of $y/D = [0 \quad 1 \quad 3]$. The PSD for the *spanwise* velocity component is plotted in Figure 6.16 in the same form as Figure 6.15.

Two strong peaks are observed in Figure 6.15a. The first peak corresponds to the periodic shedding of eddies as a von Karman vortex street, at a Strouhal number of 0.21. This peak is not evident along the cylinder centreline, and therefore indicates that a periodically shed street of coherent vortical structures is only observed in the streamwise velocity for regions aside from *y/D*=0. A secondary peak exists at *St*=0.43, but is observable only over a localised region that extends over $-1 \lesssim y/D \lesssim 1$. The energy contained in the structures represented by *St*=0.43 rapidly decays, and the peak is scarcely evident at a downstream distance of *x/D*=10. This suggests that these structures are only distinguishable in the near wake region, and therefore characterise secondary instability in the near-wake region.

Figure 6.16a displays a strong peak at *St*=0.21, and a secondary peak at approximately twice this frequency, which is not observable on the cylinder centreline. Energy in the secondary peak is also observed to rapidly decay with downstream distance, and reaffirms that the structures represented by *St*=0.43, are only evident in the near wake region. However in the intermediate field, i.e. for *x/D*=10, the PSD for both velocity components is dominated by a peak at *St*=0.21 only. This indicates that in the intermediate wake region, the VS wake has stabilised, and is dominated by the coherent street of large-scale vortical structures.

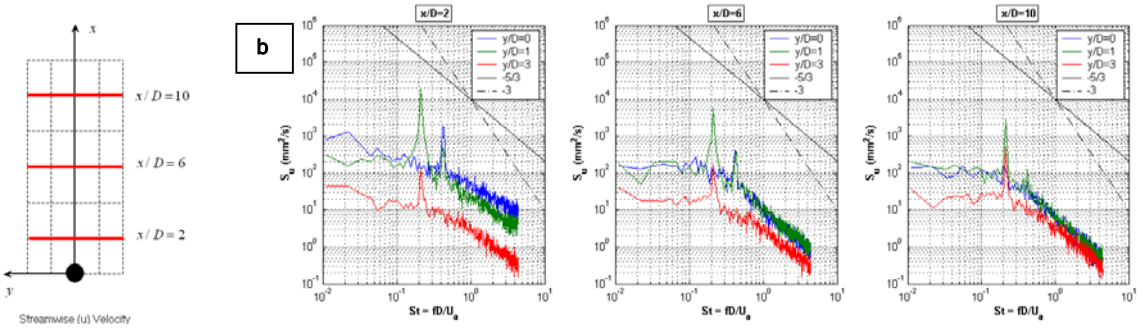

Figure 6.15 - **(a)** PSD fields for the streamwise velocity component. The PSD has been evaluated at points along the y-axis at locations of x/D=2, x/D=6 and x/D=10. **(b)** Cross-sections are taken through the PSD fields of (a) for designated values of y/D.

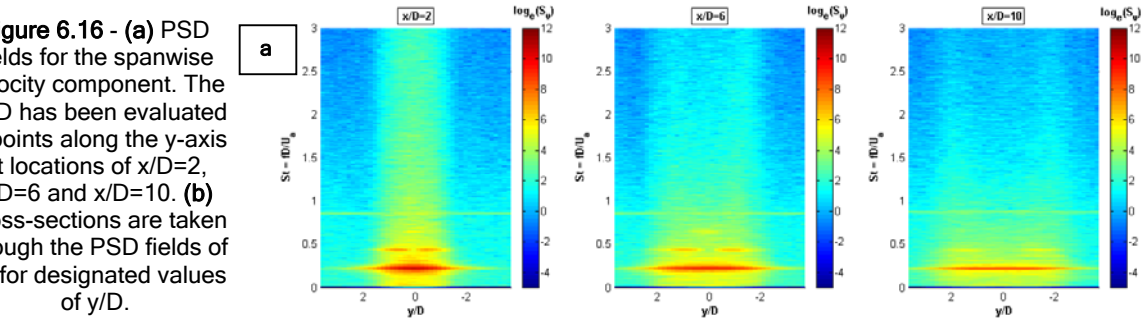

Figure 6.16 - **(a)** PSD fields for the spanwise velocity component. The PSD has been evaluated at points along the y-axis at locations of x/D=2, x/D=6 and x/D=10. **(b)** Cross-sections are taken through the PSD fields of (a) for designated values of y/D.

With regard to the smaller-scale structures, a –5/3 law is evident in the PSD estimates of Figures 6.15b and 6.16b. This suggests that vertically sheared 3D turbulence provides the mechanism for energy dissipation from the large-scale structures generated by lateral shear. Furthermore, Figures 6.15a and 6.16a indicate that the energy distribution is broadening and decaying with increasing *x/D*, indicating that the coherent structures are dissipating energy and dispersing laterally with distance downstream.

6.5 SPACE-HISTORY ANALYSIS

One of the benefits of PTV lies in its ability to provide spatial resolution of the longitudinal and transverse velocity components. The following sections utilize this ability by considering the flow evolution in space.

From Figure 6.6a, it is assumed that the mean flow is predominantly homogeneous (to within $\pm 5\%$) in the longitudinal direction, at a non-dimensional downstream distance of $6 \le x/D \le 12$. This enabled analysis to proceed in the spatial domain, as $\overline{U_i}(x)$ used to calculate the fluctuating component $u_i'(x) = u_i(x) - \overline{U}_i(x)$ was approximately constant for space-histories evaluated over $6 \le x/D \le 12$. However, it is clear from Figure 6.6b that the components of turbulent intensity (u_{irms}') are not homogeneous in the longitudinal direction between $6 \le x/D \le 12$. Indeed, v.Carmer (2005) concluded

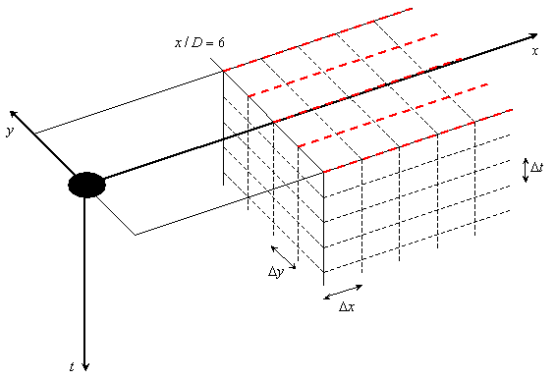

Figure 6.17 - Schematic visualisation of the 3D vector field used for analysis of the wake generated behind a circular cylinder (located at x=0, y=0) in the spatial domain. Streamwise and spanwise data series were obtained in the longitudinal (x) direction for fixed values of y (indicated by the red dotted lines). The field ranged from y/D=[-3.62 3.62] x/D=[6 12] and t/ Δt =[0 800]. Node spacing: Δx = 10mm, Δy = 10mm, Δt = 0.05s. Cylinder diameter: D=60.4mm.

that the turbulence field behind a shallow VS wake with $S_{ws} = c_f D/H = 0.07$, can not be regarded as homogeneous and isotropic until *x/D*>25. Despite this, the following analysis will provide information on the ability of the PTV system to collate space-history information in a quasi-homogeneous flow field.

The following sections analyse space-histories for the streamwise and spanwise velocity components obtained in the longitudinal (x) direction for fixed values of y, as depicted in Figure 6.17. The node spacing in the longitudinal direction was $\Delta x = 10mm$, enabling 36 data points to be collected for each space-history. In the temporal domain, 800 frames were available with node spacing at $\Delta t = 0.05s$.

6.5.1 Raw Signals

Figure 6.18a and Figure 6.18b depict the respective streamwise and spanwise velocity signals evaluated along the cylinder centreline ($y/D = 0$) for $x/D = 6$ to $x/D = 12$ from Run C3A10. Three time frames have been superimposed at a temporal increment of 0.5 seconds. Each curve represents a "snapshot" in time, of the velocity profile along the centreline of the wake generated by the circular cylinder.

The peaks of Figure 6.18b are observed to track downstream with time, which suggests that a large-scale turbulent structure is being swept downstream and is being resolved effectively by the PTV

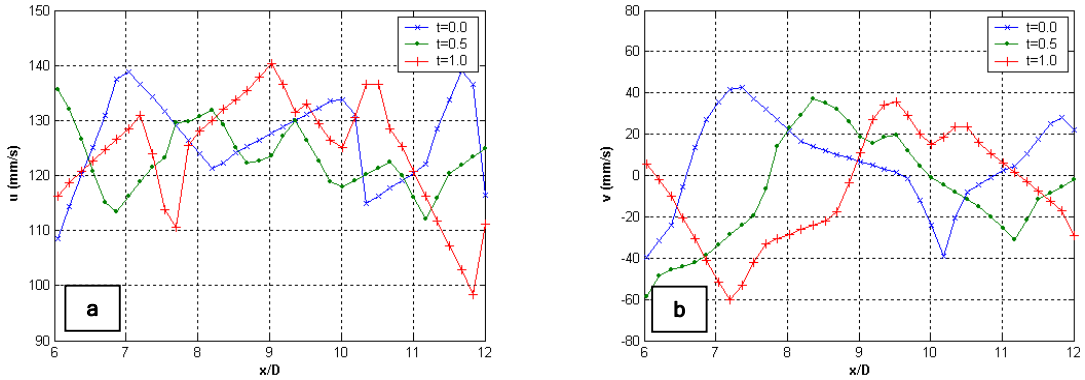

Figure 6.18 - **(a)** Streamwise and **(b)** spanwise velocity signals evaluated from Run C3A10 along the cylinder centreline (y/D=0) for x/D=6 to 12. Three time frames are superimposed.

system. No small-scale fluctuations are evident in the velocity signals of Figure 6.18, and only relatively large-scale oscillations about a mean value are evident. This can be attributed to the spatial averaging as a result of the PTV interpolation process, which effectively removes any information on structures less than the resolution of the PTV system (which is in the order of 20*mm*). Therefore the space-history information is only expected to provide information on large-scale turbulent fluctuations.

To determine the speed at which the structure evident in Figure 6.18 is being swept downstream, the autocorrelation as a function of temporal and spatial delay (refer to Eq.6.1) was evaluated for data along the longitudinal centreline of run C3A10.

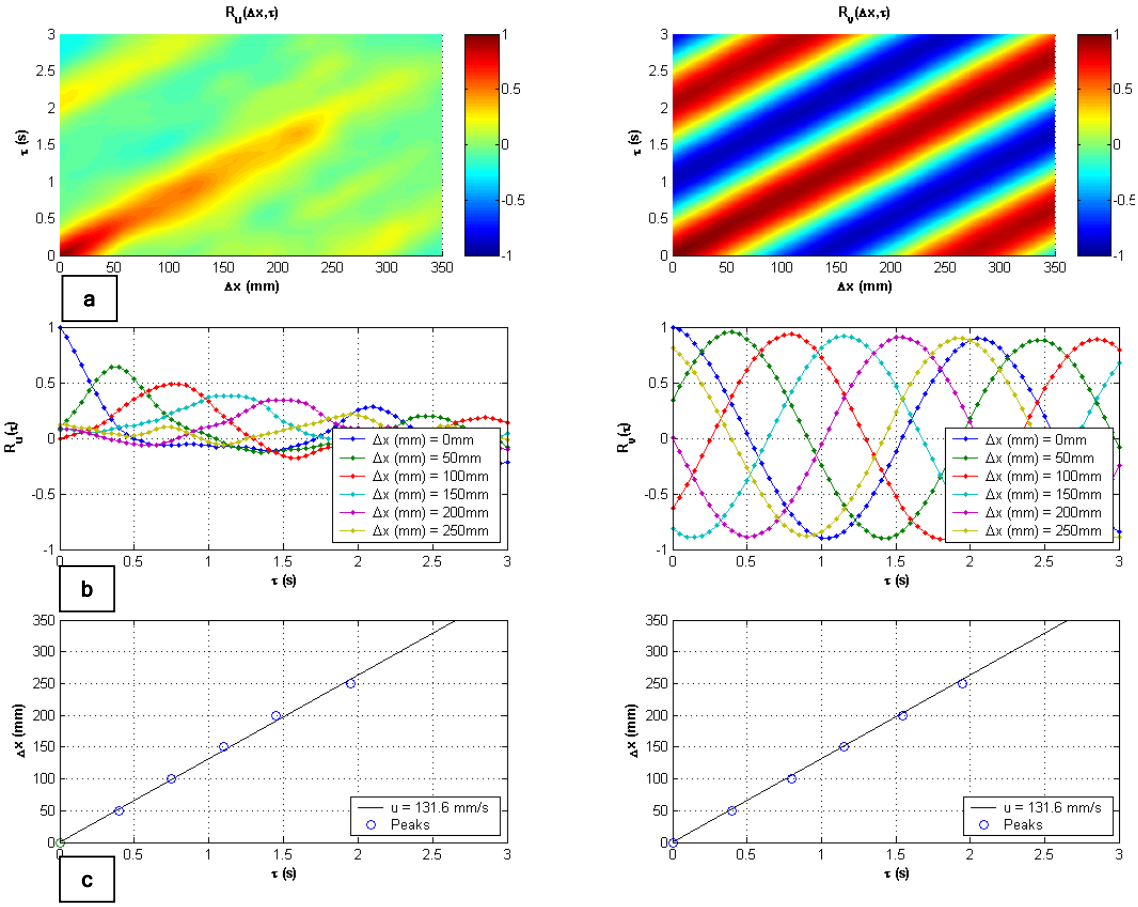

Figure 6.19 – **(a)** Autocorrelation as a function of temporal and spatial delay, evaluated for data along longitudinal centreline for streamwise and spanwise fluctuating velocity components of Run C3A10 **(b)** Cross-sections taken through the autocorrelation fields of (a) at 50mm offsets **(c)** The temporal delay corresponding to the peaks of the temporal autocorrelation in (b) plotted against U=131.6mm/s.

$$R_{u_i}(\Delta x,\tau)=\frac{\overline{u_i'(x,t)\,u_i'(x+\Delta x,t+\tau)}}{\sqrt{\overline{u_i'(x,t)^2}}\sqrt{\overline{u_i'(x+\Delta x,t+\tau)^2}}} \tag{6.1}$$

Figure 6.19a depicts that $R_v(\Delta x,\tau)$ is strongly correlated for all Δx, however the correlation decays relatively rapidly for $R_u(\Delta x,\tau)$. The values of τ that correspond to the peaks of $R_{u_i}(\tau)$ plotted in Figure 6.19b, are plotted in Figure 6.19c. This figure indicates that a structure is propagating along the cylinder centreline at a velocity of 131.6*mm/s*. This velocity corresponds to $0.77U_s$ which is approximately the value of the centreline velocity deficit, at the surface, over the region *x/D*=6 to 12 (refer to Figure 6.6a). This suggests that the turbulent structure is advected by approximately the speed of the mean surface flow, and therefore Taylor's frozen turbulence hypothesis holds over the region *x/D*=6 to 12 for large-scale turbulent structures.

6.5.2 Probability Density Functions

Figure 6.20a and 6.20b depict the probability density function evaluated for space-histories for the respective standardised streamwise and spanwise instantaneous velocity components. For a fixed value of y/D, the PDF has been evaluated for space-history data in the longitudinal domain over the range $6\le x/D\le 12$. This is repeated for each signal over 800 time frames, and averaged. Figure 6.20c and 6.20d depict slices taken at locations of $y/D=[0\ \ 1\ \ 2\ \ 3]$ through the respective PDF fields of Figure 6.20a and 6.20b. Finally, Figure 6.20e and 6.20f depict the distribution of skewness and flatness along the transverse axis, for the PDFs plotted in Figure 6.20a and 6.20b.

Both the PDF evaluated for the standardised streamwise and spanwise velocity is analogous to the PDF evaluated in the temporal domain, as outlined in Section 6.4.2. This is expected as the PDF is averaged over the temporal domain, and therefore is effectively providing an average of the PDF published in Figures 6.9 and 6.10 for data over the region $6\le x/D\le 12$. Figure 6.20a and 6.20b indicated that $p(\hat{u})$ is close to Gaussian with some imbedded disturbance visible in the plots of

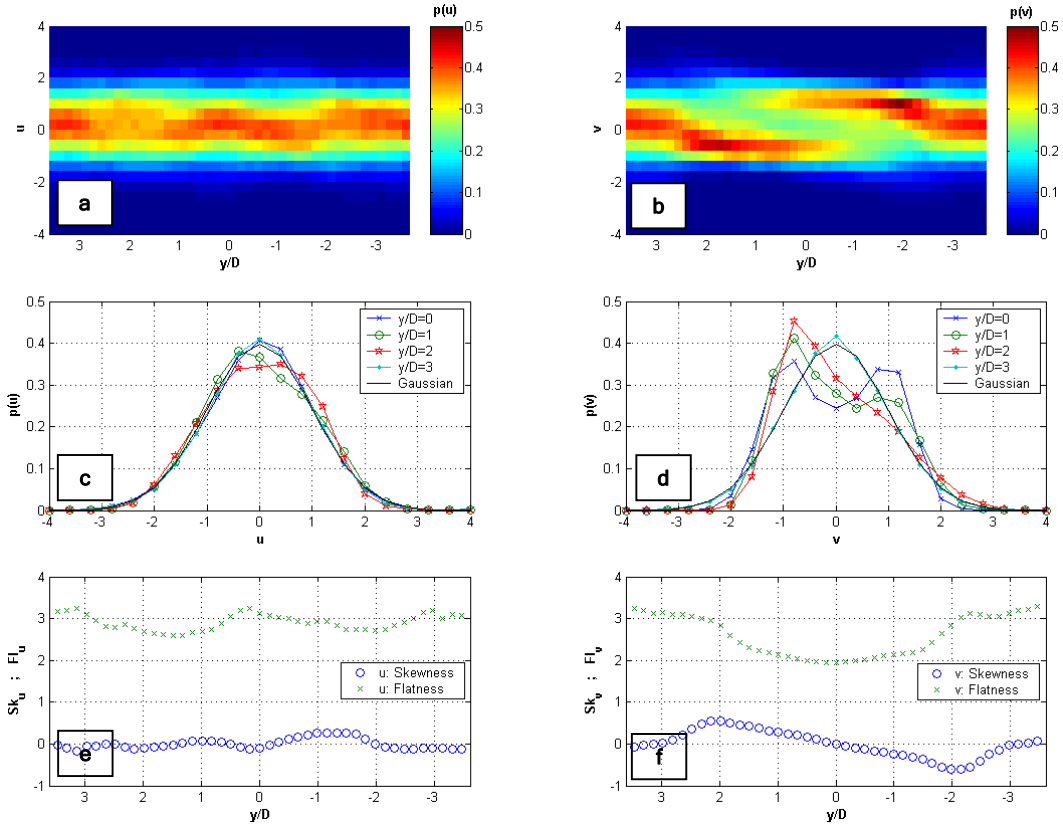

Figure 6.20 - PDFs evaluated for space histories of the standardised instantaneous **(a)** streamwise and **(b)** spanwise velocities. Cross-sections are taken through the fields of (a) and (b) for designated values of y/D, and depicted for the **(c)** streamwise and **(d)** spanwise velocity. Skewness and flatness distributions as a function of the transverse coordinate for the **(e)** streamwise and **(f)** spanwise velocity.

skewness and flatness. However $p(\hat{v})$ is strongly asymmetric and non-homogeneous with respect to the transverse coordinate.

6.5.3 Autocorrelation

Figure 6.21a and 6.21b depict the autocorrelation fields evaluated for space-histories of the respective streamwise and spanwise fluctuating velocity components. For a fixed value of y/D, the autocorrelation function has been evaluated in the longitudinal domain (i.e. $x/D=6$ to $x/D=12$), with a spatial delay of $\Delta x=10mm$. This is repeated for each signal over 800 time frames, and averaged. Figure 6.21c and Figure 6.21d depict slices taken at locations of $y/D=[0\ \ 2]$ through the respective autocorrelation fields of Figure 6.21a and Figure 6.21b. In Figure 6.21c and 6.21d, $R_{u_i}(\tau\overline{U}/D)$ evaluated for the cylinder centreline, and averaged over $6\le x/D\le 12$ has been plotted

for comparison with $R_{u_i}(\Delta x/D)$ evaluated for y/D=0. A value of $\overline{U}=131.6mm/s$ has been used to represent the propagation of the flow field in accordance with Section 6.5.2.

Typically, the autocorrelation function only provides reliable information over $\tau/T_s \lesssim 0.3$ (Nikora, 2005) where τ denotes the delay (temporal or spatial) and T_s denotes the total sampling period or space. The unreliable estimates of the autocorrelation coefficient for $\tau/T_s \gtrsim 0.3$ results from the zero padding introduced by the MATLAB correlation routine. As a result $R_{u_i}(\Delta x/D)$ plotted in Figure 6.21 is only reliable over the range $0<\Delta x/D \lesssim 1.8$, and Taylor's hypothesis holds with reasonable agreement over this range. For larger delays the autocorrelation in the spatial domain departs from $R_{u_i}(\tau\overline{U}/D)$ due to unreliable estimates of the autocorrelation coefficient over $\Delta x/D \gtrsim 1.8$.

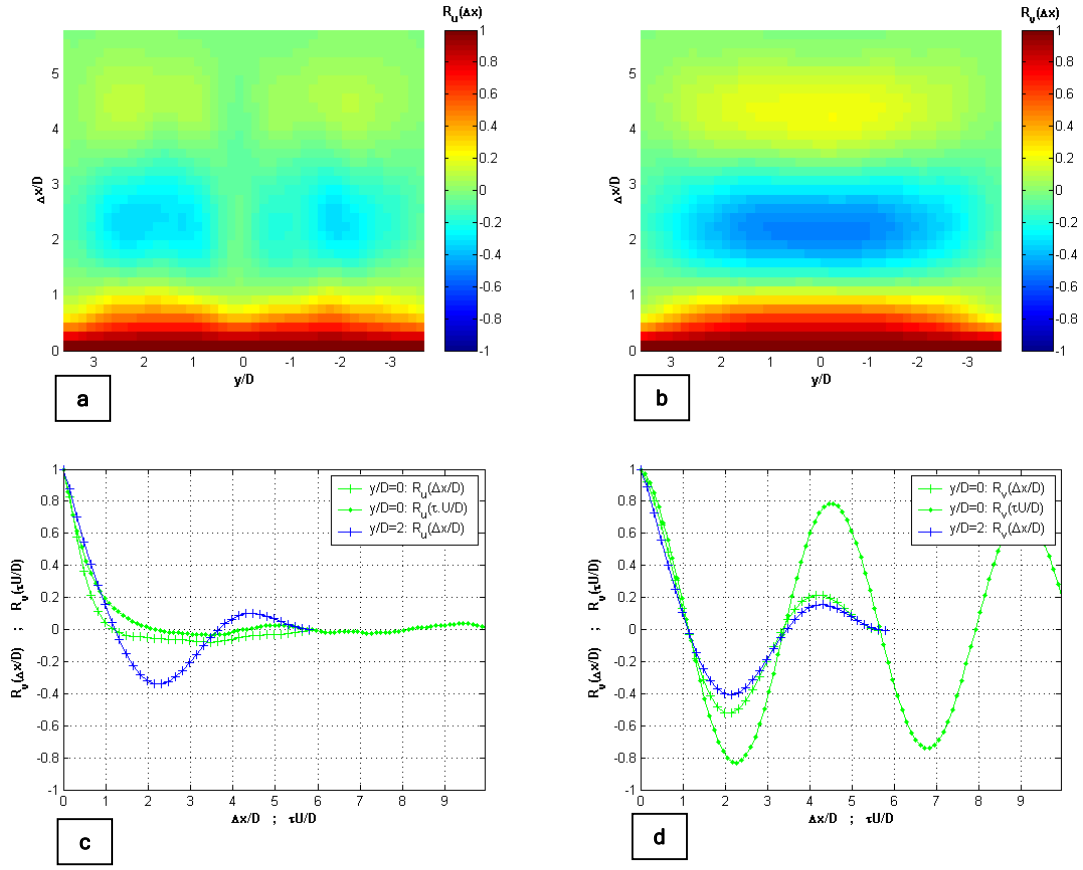

Figure 6.21 – Autocorrelation function evaluated for space histories of the fluctuating **(a)** streamwise and **(b)** spanwise velocity components. Cross-sections are taken through the fields of (a) and (b) for designated values of y/D, and depicted for the **(c)** streamwise and **(d)** spanwise velocity.

The autocorrelation evaluated in the spatial domain also displays that large-scale structures are not correlated along the cylinder centreline, however there is strong correlation between $R_u(\Delta x/D)$ and $R_v(\Delta x/D)$ for regions outside $-0.5 < y/D < 0.5$. This is consistent with the findings of the temporal autocorrelation presented in Section 6.4.3.

6.5.4 Power Spectral Density

Figure 6.22a and 6.22b depict the power spectral density (PSD) field for the respective stream-wise and cross-stream fluctuating velocity components. For a fixed value of y/D, the PSD has been evaluated in the longitudinal domain (i.e. $x/D = 6$ to $x/D = 12$), with a spatial sampling increment of $\Delta x = 10mm$. This is repeated for each signal over 800 time frames, and averaged. Figures 6.22c and 6.22d depict slices taken at locations of $y/D = [0\ \ 2]$ through the respective PSD fields of Figure 6.22a and 6.22b

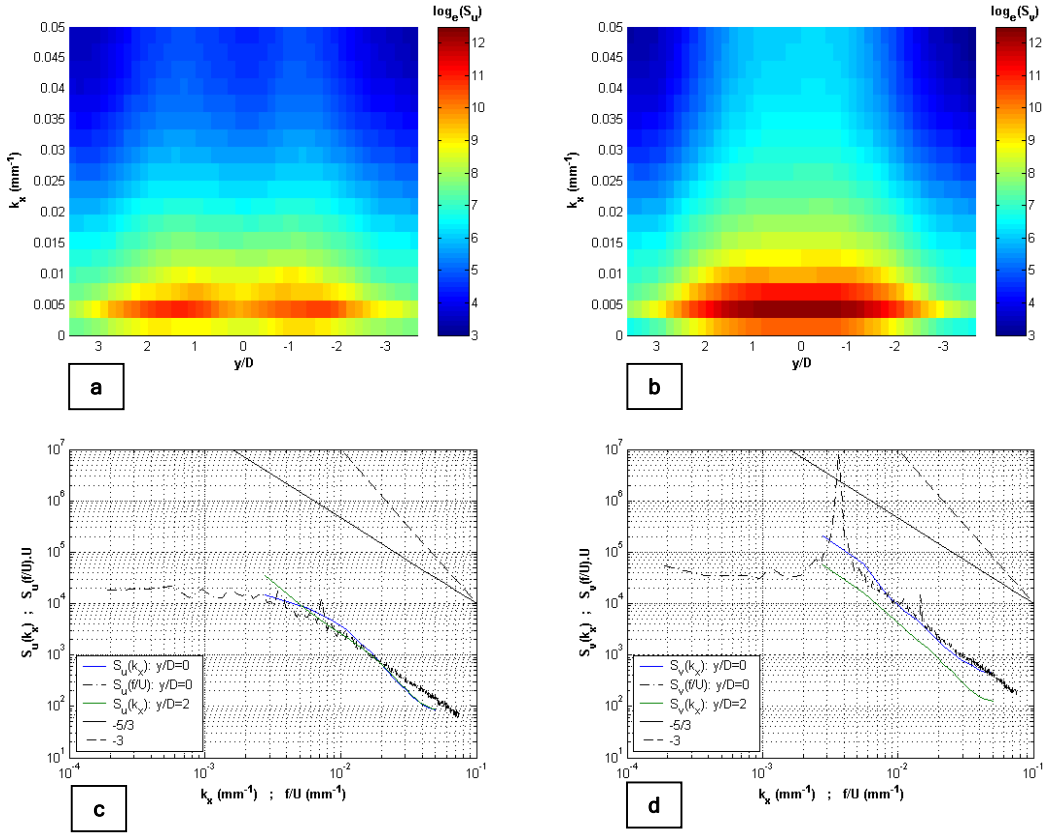

Figure 6.22 - PSD evaluated for space histories of the fluctuating **(a)** streamwise and **(b)** spanwise velocity components. Cross-sections are taken through the fields of (a) and (b) for designated values of y/D, and depicted for the **(c)** streamwise and **(d)** spanwise velocity.

No peak in $S_v(k_x)$ is evident in Figure 6.22d, which is a strong characteristic of $S_v(f/\overline{U})$. This is attributed to the limited sampling length of the space-history, which is not long enough to resolve a full shedding cycle. Furthermore Figure 6.22c indicates that $S_u(k_x)$ departs from $S_u(f/\overline{U})$ at high wavenumbers. This is due to the limited spatial resolution of the PTV system, which is unreliable in determining small-scale structures in the space domain.

In summary, the spectra evaluated in the spatial (or wavenumber) domain are inconclusive, and less reliable than the spectra evaluated in the temporal (or frequency) domain, due to the limited sampling length and resolution of the PTV system in the spatial domain.

6.6 SUMMARY

The previous sections have presented time-averaged, time-history and space-history analysis of a vortex street wake generated by a circular cylinder in a shallow flow. Due to the limited longitudinal extent of the experimental flume, analysis was restricted to the near-wake and intermediate-wake regions only. The transition between the near wake and intermediate wake was expected to occur at a non-dimensional downstream distance of x/D~7, however it must be noted that this scale is an order of magnitude estimate only.

The time-averaged velocity profiles indicated the expected disturbed flow regions for a turbulent plane wake. Two sidewise regions of disturbed and accelerated flow were apparent about the shoulders of the cylinder, and a velocity deficit was apparent in the wake region. The turbulent intensity profiles indicated that the wake was strongly influenced by fluctuations in the transverse direction, and both turbulent intensity components displayed maximums in the near wake region. Furthermore, the Reynolds stress term, $-\overline{u'v'}$, displayed an absolute maximum which corresponded to the location at which the free shear layers were being alternately rolled up to form discrete large-scale structures. In the intermediate field, the rate of decay of the turbulent stress components was greatly diminished as the 2DCS generated by the circular cylinder were dissipated under the effects of bed friction.

The probability density function was evaluated for the time-histories of the transverse and longitudinal velocity components at various locations downstream of the circular cylinder. Strong asymmetry was evident in the PDF for the spanwise velocity component for all regions apart from the cylinder centreline and outside the disturbed wake region. The PDF for the longitudinal velocity component displayed a predominantly Gaussian distribution for the cylinder centreline and for regions outside the disturbed wake. Aside from these regions, the PDF for the longitudinal velocity component displayed an asymmetry and a flatness of less than three.

The autocorrelation function was strongly correlated in time for the transverse velocity and streamwise velocity components, which indicated the presence of organised large-scale 2D structures. Along the cylinder centreline $R_u(\tau)$ was rapidly damped with increasing x/D and the frequency of the oscillations was approximately double that of the transverse case. This indicated that along the cylinder centreline, coherent structures were less prominent due to the effect of the counter-rotating streets of vortices shed above and below $y/D=0$.

The 1D power spectral density was also calculated at various locations in the wake behind the circular cylinder. The large-scale (low frequency) flow structure was dominated by an alternately rotating street of 2DCS. These structures were characterised by a Strouhal number of 0.21. Secondary peaks in the PSD estimates at successive Strouhal numbers of 0.42, 0.65 were also evident in the near wake region. It is postulated that structures represented by these peaks characterise secondary instability in the near-wake region. No evidence of energy transfer from small-scale structures to the 2DCS was evident in the PSD estimates. Regarding the small-scale flow structure, a clear –5/3 power law was observed to high frequencies, indicating energy dissipation via 3D turbulence. However close to the cylinder, i.e. $x/D<2$, a –1 law is observed in the streamwise PSD.

Section 6.6 examined the flow evolution in space. It was concluded that the large-scale structures propagated at the mean surface flow velocity along the centreline of the cylinder. This indicated that

Taylor's hypothesis will hold for the large-scale 2D structures. However, further analysis in the spatial domain was inconclusive due to the limited sampling length of space-histories and the limited resolution of the PTV system in the spatial domain.

7.0 Conclusions

The goal of this study was to investigate the mean flow and turbulent properties at the surface of shallow flows. The study considered two flow regimes. The first regime consisted of one subcritical flow and two supercritical plane, uniform, shallow turbulent shear flows. Secondly a mechanism that produced large-scale, quasi two-dimensional turbulent structures was introduced into the shallow turbulent shear flows in the form of an isolated single cylinder. The resulting flow was a shallow vortex street wake.

7.1 MEASUREMENT TECHNIQUES

All flows were generated in an experimental flume that could be tilted over variable bed slopes. The channel bed had dimensions of 1970*mm* (length) x 974*mm* (width). Due to the limited longitudinal extent of the flume, sluice gates had to be implemented to ensure uniform flow conditions. Velocity fields were evaluated at the surface of the shallow flows, over a 600*mm* x 440*mm* window, using a particle tracking velocimetry (PTV) system. This system consisted of a mechanically driven particle dispenser that distributed 2-3*mm* polypropylene (PP) particles at the flow surface. The particles were partially submerged, and therefore sampled the surface flow and a portion of the sub-surface flow. A high-speed digital video camera was used to capture images of the seeded flow illuminated by a halogen light source. Finally, velocity fields were generated from the digital images using Streamline 5.0 PTV software (Nokes, 2005b).

The resolution of the PTV system was restricted by the particle seeding and particle response time to flow structures. It was estimated that flow structures of the order of 20*mm* and greater could be resolved. Accordingly, the PTV system underestimated turbulent intensity values, relative to the semi-empirical values stated by Nezu & Nagakawa (1993), for the shallow shear flow regimes as these flows exhibited flow depths of 20*mm* and less. However the ratio of v'_{rms}/u'_{rms} evaluated by the PTV

system was directly comparable to the values stated by Nezu & Nagakawa (1993), which indicated that turbulent structures were accurately being resolved by the PTV system, but their absolute intensity was being damped due to the limited resolution. For the shallow wake flow regime, the turbulent intensities were well represented by the PTV system, as this flow was dominated by large-scale 2D flow structures with length scales greater than the resolution of the PTV system.

7.2 SHALLOW SHEAR FLOWS

Analysis of the shallow, turbulent shear flows indicated that the surface velocities evaluated by the PTV system compared well with the theoretical value predicted by the Blasius $1/7^{th}$ power law, and the mean velocity and turbulent stress profiles were predominantly homogeneous over the flow field. The probability density function was evaluated for the instantaneous velocity components, and closely represented a Gaussian distribution. Analysis of the autocorrelation function evaluated in both the temporal and spatial domains confirmed that Taylor's frozen turbulence hypothesis held. The integral length scales were evaluated from the autocorrelation functions and indicated the presence of predominantly 2D isotropic turbulent structures at the free surface with length-scales greater than the flow depth. This finding was consistent with dye visualisation experiments and research by Kumar, et al (1998) who defined such large-scale structures at the free surface as spiral eddies. The 1D power spectral density (PSD) estimates indicated that energy was contained in structures with dimensions much greater than the flow depth, after which a –5/3 law was observed to smaller frequencies / wavenumbers.

7.3 SHALLOW VORTEX STREET WAKE FLOW

Due to the limited longitudinal extent of the flume, analysis of the shallow turbulent wake flow regime was restricted to the near-wake and intermediate wake regions, as defined by v.Carmer (2005). Furthermore only one cylinder of diameter 60.4*mm* was considered, as cylinders with greater diameter introduced secondary disturbances into the flow due to wake interaction with the flume boundaries. The type of wake that resulted from the 60.4*mm* diameter cylinder was a von Karman vortex street,

which was characterised by the periodic shedding of two-dimensional coherent structures (2DCS) in the lee of the cylinder.

The turbulent stress fields evaluated for the von Karman vortex street wake indicated that the near-field region was strongly influenced by momentum exchange between the mean flow and 2D turbulence. In the intermediate field, the rate of decay of the turbulent stress components greatly diminished as the 2DCS were both stabilised and dissipated through the influence of bed friction.

The PDF was evaluated at various locations in the VS wake, and indicated strong periodicity in the transverse velocity signals. The PDF for the streamwise velocity component was characterised by a Gaussian distribution along the cylinder centreline, and for regions outside the disturbed wake region. The autocorrelation was strongly modulated for both velocity components for regions either side of the cylinder centreline, indicating the existence of large-scale 2DCS in the disturbed wake region. Interestingly, the streamwise autocorrelation function evaluated along the cylinder centreline, was rapidly damped relative to the spanwise autocorrelation and oscillated at a frequency that was approximately twice the period of the $R_v(\tau)$. It is suggested that coherence in the streamwise velocity signal is damped on the cylinder centreline due to the counter-rotating street of vortices shed above and below the longitudinal centreline. However for regions either side of the cylinder centreline coherent structures with the same sense of rotation are free to propagate downstream, without interference

Spectral analysis of the fluctuating velocity components indicated that the majority of energy was contained in the large-scale (low frequency) structures, represented by a Strouhal number of 0.21. No evidence of energy transfer from small-scale structures to the 2DCS was evident in the power spectral density (PSD) estimates. Indeed a clear –5/3 power law was observed to high frequencies, indicating energy dissipation via 3D turbulence. Secondary peaks at Strouhal numbers of 0.42 and 0.65 were also

present in the near-wake region. This suggested that the highly disturbed flow in the near-wake region introduced secondary instabilities into the VS wake flow.

7.4 AREAS FOR FUTURE INVESTIGATION

This project has provided information on the large-scale turbulent structures present at the surface of a shallow turbulent wake flow and shallow shear flows. However information regarding the small-scale turbulence was restricted by the limited resolution of the PTV system. It is recommended that future studies investigate methods to increase the resolution of the PTV system by using smaller, more densely spaced particles (e.g. hollow glass micro-spheres) in conjunction with a higher resolution camera and increased sampling frequency. Illumination of the particles with a laser or white light sheet should be considered in order to provide PTV measurements at subsurface locations. This would also allow validation of the results gathered via PTV with an LDV system.

This study has also indicated the potential of PTV to resolve information in the spatial, or wavenumber, domain. Increasing the spatial resolution of the PTV system by implementing the measures stated above would enable turbulence to be analysed more robustly in wavenumber space.

Other points of interest raised in this study was the existence of short-lived, quasi-2D structures at the surface of shallow, shear flows. Kumar, et al (1998) suggested a mechanism that generates these structures, however further investigation into the conditions (i.e. flow depths) in which these structures prevail as well as their contribution to the turbulent energy spectrum is warranted. Regarding the shallow VS wake flow, the transition from the intermediate to far-field wake has yet to be distinguished, and the spectral characteristics within the re-circulation region have not been considered. Finally, the wake behind a cylinder placed in a supercritical flow was not able to be analysed during this study and hence provides an area for future investigation.

8.0 References

Akilli, H., A. Akar, et al. (2004). "Flow characteristics of circular cylinders arranged side-by-side in shallow water." Flow Measurement and Instrumentation **15**: 187-197.

Akilli, H. and D. Rockwell (2002). "Vortex formation from a cylinder in shallow water." Physics of Fluids **14**(9): 2957-2967.

Balachandar, R., S. Ramachandran, et al. (2000). "Characteristics of shallow turbulent near wakes at low Reynolds numbers." Journal of Fluids Engineering **102**: 302-308.

Balachandar, R. and M. F. Tachie (2001). "A study of boundary layer-wake interaction in shallow open channel flows." Experiments in Fluids **30**: 551-521.

Ballard, C. E. (2004). The dynamics of free surface gravity currents in lock exchange flows. Civil Engineering, University of Canterbury. **ME Thesis**.

Bendat, J. S. and A. G. Piersol (2000). Random data: analysis and measurement procedures, John Wiley & Sons, Inc.

Brennen, C. E. (2005). Fundamentals of multiphase flow, Cambridge University Press.

Carrasco, A. and C. A. Vionnet (2004). "Separation of scales on a broad, shallow turbulent flow." Journal of Hydraulic Research **42**(6): 630-638.

Chen, D. and G. H. Jirka (1995). "Experimental study of plane turbulent wakes in a shallow water layer." Fluid Dynamics Research **16**: 11-41.

Corbis (2005). Corbis stock photography and pictures [Online]. Available: http://www.corbis.com.

Danilov, S. D. and D. Gurarie (2000). "Quasi-two-dimensional turbulence." Physics-Uspekhi **43**(9): 863-900.

Dyke, M. v. (1982). An album of fluid motion, Parabolic Press.

Etter, D. M. (1993). Engineering problem solving with matlab.

Frisch, U. (1995). Turbulence: the legacy of A. N. Kolmogorov. Cambridge, Cambridge University Press.

Glickman, T. S., Ed. (2000). Glossary of meteorology, American Meteorological Society.

Hearn, G. E. and A. V. Metcalfe (1995). Spectral analysis in engineering concepts and cases, Arnold.

Henderson, F. M. (1966). Open channel flow, The Macmillian Company.

Hinze, J. (1975). Turbulence, McGraw Hill, Inc.

Jirka, G. H. (2001). "Large scale flow structures and mixing processes in shallow flows." Journal of Hydraulic Research **39**(6): 567-573.

Kennedy, J. B. and A. M. Neville (1986). "Basic statistical methods for engineers and scientists."

Kirkgoz, M. S. and M. Ardichoglu (1997). "Velocity profiles of developing and developed open channel flow." Journal of Hydraulic Engineering **123**(12): 1099-1105.

Kumar, S., R. Gupta, et al. (1998). "An experimental investigation of the characteristics of free-surface turbulence in channel flow." Physics of Fluids **10**(2): 437-455.

Lesieur, M. (1990). Turbulence in fluids: stochastic and numerical modeling, Kluwer Academic Publishers.

Lloyd, P. M. and P. K. Stansby (1997). "Shallow-water flow around model conical islands of small side slope." Journal of Hydraulic Engineering **123**(12).

Mathieu, J. and J. Scott (2000). An introduction to turbulent flow, Cambridge University Press.

Nadaoka, K. and H. Yagi (1998). "Shallow-water turbulence modeling and horizontal large-eddy computation of river flow." Journal of Hydraulic Engineering **124**(5): 493-500.

NASA (2005). Visible Earth Website [Online]. Available: http://visibleearth.nasa.gov/.

Nezu, I. and H. Nakagawa (1993). Turbulence in open-channel flows, A.A. Balkema.

Nikora, V. I. (2005). Personal Correspondence.

Nikora, V. I. and D. G. Goring (2001). "Extended self-similarity in geophysical and geological applications." Mathematical Geology **33**(3): 251-271.

Nokes, R. (2005a). Imagestream version 4.00: operation manual, University of Canterbury.

Nokes, R. (2005b). Streamline version 5.00: operation manual, University of Canterbury.

Nokes, R., S. Blackett, et al. (2003). "Design, performance and application of a generalised optimisation-based particle tracking velocimetry system." In preparation.

Paret, J. and P. Tabeling (1998). "Intermittency in the two-dimensional inverse cascade of energy: experimental observations." Physics of Fluids **10**(12): 3126-3136.

Plew, D. (2005). The hydrodynamic effects of long line mussel farms. Civil Engineering, University of Canterbury. **PhD Thesis**.

Pope, S. B. (2000). Turbulent flows, Cambridge Universtiy Press.

Raffel, M., C. Willert, et al. (1998). Particle image velocimetry: a practical guide. Berlin, Springer.

Rajagopalan, S. and R. A. Antonia (2005). "Flow around a circular cylinder - structure of the near wake shear layer." Experiments in Fluids **38**: 393-402.

Rummel, A. C., S. A. Socolofsky, et al. (2005). "Enhanced diffusion from a continuous point source in shallow free-surface flow with grid turbulence." Physics of Fluids **17**(7).

Rutgers, M. A. (1998). "Forced 2D turbulence: experimental evidence of simultaneous inverse energy and forward enstrophy cascades." Physical Review Letters **81**(11): 2244-2247.

Sirovich, L. and S. Karlsson (1997). "Turbulent drag reductions by passive mechanisms." Nature **388**(21): 753-755.

Tennekes, H. and J. L. Lumley (1972). A first course in turbulence, The MIT Press.

Uijttewaal, W. and G. H. Jirka (2001). Experiments on shallow flow turbulence. Proceedings 3rd. Int. Symp. Environ. Hydr., Tempe, USA.

Uijttewaal, W. and G. H. Jirka (2003). "Grid turbulence in shallow flows." Journal of Fluid Mechanics **489**: 325-344.

Uijttewaal, W. S. J. and R. Booij (2000). "Effects of a shallowness on the development of free-surface mixing layers." Physics of Fluids **12**(2): 392-402.

v.Carmer, C. F. (2005). Shallow turbulent wake flows: momentum and mass transfer due to large-scale coherent vortical structures. Institute for Hydromechanics, University of Karlsruhe. **PhD Thesis**.

v.Carmer, C. F. and G. H. Jirka (2001). On turbulence and transport in shallow wake flows. Proceedings 29th. IAHR Congress, Beijing China. **B**:80-86.

v.Carmer, C. F., V. Weitbrecht, et al. (2001). On the genesis and fate of large coherent vortical structures in turbulence shallow wake flows. Proceedings 3rd. Int. Symp. Environ. Hydr., Tempe, USA.

Warhaft, Z. (2002). "Turbulence in nature and the laboratory." PNAS **99**: 2481-2486.

Weitbrecht, V. (2004). Influence of dead-water zones on the dispersive mass transport in rivers. Institute for Hydromechanics, Universtiy of Karlsruhe. **PhD Thesis**.

Weitbrecht, V., G. Kühn, et al. (2002). "Large scale PIV measurements at the surface of shallow water flows." Flow Measurement and Instrumentation **13**: 237-245.

Zdravkovich, M. (1997). Flow around circular cylinders. Vol 1: Fundamentals. New York, Oxford University Press Inc.

APPENDIX A

This appendix details the method used to determine the channel bed slope.

A.1 PROCEDURE

A survey level and staff was used to ensure the bed was level, as well as to establish the required bed slope. The channel bed was firstly set to zero degrees with a spirit level, and survey levels were then taken at the nine points as outlined in Figure A.1a. Fine adjustment of the channel bed was then achieved by manipulating the four screw jacks situated at the four corners of the flume. Adjustment continued until the level readings at each of the nine points differed by a maximum of $\pm 0.5mm$.

To set the bed slope, the channel bed was tilted to the desired channel slope with a hydraulic jack situated underneath the base of the flume. Fine adjustments were then made with the screw jacks until the elevations at in each transverse cross-section differed by a maximum of $\pm 0.5mm$. Finally, the bed slope was calculated by averaging the three level measurements at $x = 40$ (denoted z_1 as depicted in Figure Ab) and at $x = 1930$ (denoted z_2). The drop in elevation, $z_3 = z_1 - z_2$, was then used to calculate the true bed slope, $S = \tan^{-1}(z_3 / L)$, where L was the longitudinal distance between the inlet and outlet of the channel (i.e. $1890mm$). The measurement accuracy of the survey level was approximately $\pm 0.5mm$ over the elevation difference between the inlet (z_1) and outlet (z_2) of the flume.

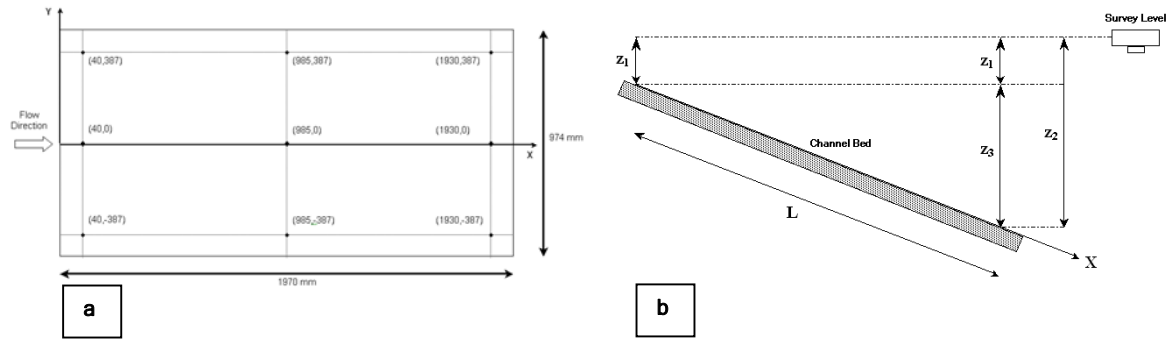

Figure A.1 - **(a)** Coordinate system and survey level points (all units in millimetres, diagram not to scale). **(b)** Schematic of survey set-up indicating vertical elevation notation.

APPENDIX B

Preliminary testing indicated a non-uniform velocity distribution for flows established in the shallow flow flume. This appendix details the techniques used to ensure near-uniform velocity distributions.

B.1 LONGITUDINAL VELOCITY AND DEPTH PROFILES

Subcritical and supercritical flows with the parameters listed in Table B.1 were established in the shallow flow flume. The depth profiles evaluated along the longitudinal centreline of the channel bed (refer to Figure B.1 for an outline of the coordinate system) are depicted in Figure B.2a and B.2b as red lines. Velocity profiles are also evaluated over the PTV measurement window for $y \simeq -125$, $y = 0$, and $y \simeq 125$, and displayed as red lines in Figure B.2c for the supercritical flow and in B.2d for the subcritical flow.

In Figure B.2a, the depth is decreasing with increasing longitudinal distance downstream, and this trend is reflected in the supercritical velocity profiles (the red lines in Figure B.2c). In Figure B.2b and B.2d, the same trends are observed for the subcritical flow case. It is clear from these plots that the "in situ" flow conditions were not uniform and homogeneous in the longitudinal direction for both the supercritical and subcritical flow cases.

To create uniform flow conditions, a sluice gate was constructed out of Perspex. The sluice gate was attached to a steel bar, which spanned the width of the flume, and could be raised and lowered to the desired gate elevation. For the testing outlined in this appendix, the sluice gate was placed $50mm$ downstream from the flume inlet, with a gate opening of $15mm$, for supercritical conditions, and $110mm$ upstream of the flume outlet, with a gate opening of $11mm$, for sub-critical conditions.

The depth profiles evaluated along the longitudinal centreline of the channel bed are detailed in Figure B.2a and B.2b as blue lines. Velocity profiles evaluated over the PTV measurement window are displayed as blue lines in Figure B.2c for the supercritical flow and in B.2d for the subcritical flow

It is evident from Figure B.2 that predominantly uniform longitudinal depth and velocity profiles, to within $\pm 5\%$, resulted from the implementation of the sluice gate for both supercritical and subcritical cases. By taking an ensemble average over eight or more runs, the departure from uniform flow was further decreased to $\pm 2.5\%$.

B.2 TRANSVERSE VELOCITY PROFILES

The red line of Figure B.3 represents the transverse velocity distribution evaluated at the X=985mm for a shallow subcritical flow with the hydraulic parameters listed in Table B.2. From this plot it is clear that a non-uniform transverse velocity profile was present This was due to the outlet pipe, leading into the upstream header basin, generating a jet of water towards the true right of the flume. Consequently preliminary PTV data indicated faster velocities occurring on the true right of PTV measurement window. The non-uniform transverse velocity profile was not present in the supercritical flow cases as the upstream sluice gate removed any inconsistency from the inlet conditions.

To eliminate this problem, a porous baffle and honeycomb flow stabilisers were placed within the upstream header basin, to negate the effects of the jet resulting from the outlet flow. The baffle and flow stabilisers reduced the transverse flow error to ± 2.5% as seen in the blue line depicted in Figure B.3.

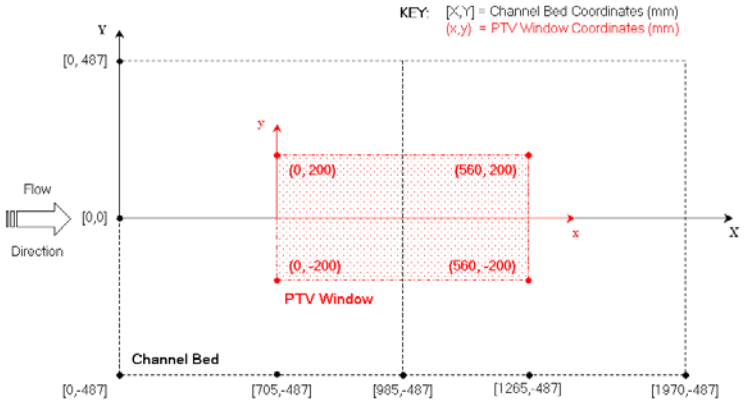

Figure B.1 - Illustration of the coordinate system for the channel bed and PTV measurement window.

Table B.1 - Flow parameters for testing carried out on supercritical (Runs#5A and #5B) and subcritical flows (Runs#6A and #6B) with and without a sluice gate

Run	Flow Type	Sluice Gate	Flow Rate Q (l/s)	Bed Slope S (-)	Flow Depth* H (mm)	U_a(+) (mm/s)	Re_H(+) (-)	Fr(+) (-)
Run#5A	Supercritical	Yes	6.26	1.00	9.1	706.3	6427.1	2.4
Run#5B	Supercritical	No	6.26	1.00	10.8	595.1	6427.1	1.8
Run#6A	Subcritical	Yes	6.34	0.10	33.7	193.2	6509.2	0.3
Run#6B	Subcritical	No	6.34	0.10	20.3	320.7	6509.2	0.7

* Flow depth is based on an average across the longitudinal centreline

(+) $U_a = Q/A$, $Re_H = U_a H/\upsilon$, $Fr = U_a/\sqrt{gH}$

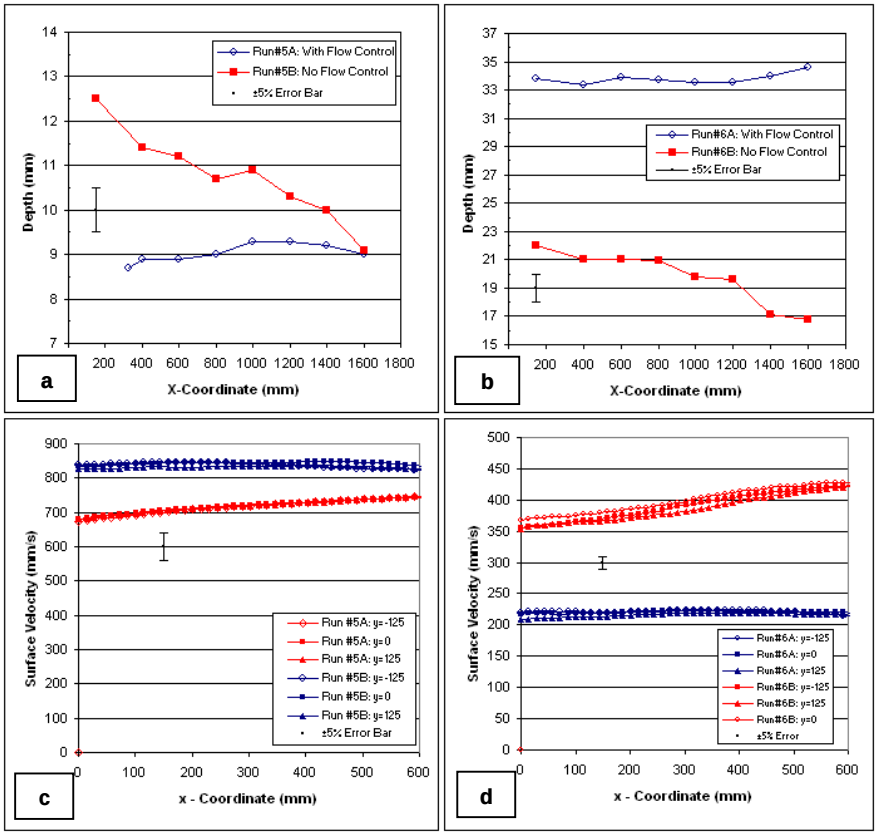

Figure B.2 – Depth profiles along the longitudinal (X) axis of the channel for the **(a)** supercritical flow case and **(b)** for the subcritical flow case outlined in Table A.1. Velocity profiles along the longitudinal (x) axis of the PTV window for the **(c)** supercritical flow case and **(d)** for the subcritical flow case outlined in Table A.1.

Table B.2 – Flow parameters for testing carried out on supercritical (Runs#5A and #5B) and subcritical flows (Runs#6A and #6B) with and without a sluice gate

Run	Flow Type	Sluice Gate	Flow Rate Q (l/s)	Bed Slope S (-)	Flow Depth* H (mm)	U_a (+) (mm/s)	Re_H (+) (-)	Fr (+) (-)
Run#1D	Subcritical	Yes	2.72	0.001	20	139.6	2792.6	0.3

* Flow depth is based on an average across the longitudinal centreline

(+) $U_a = Q/A$, $\mathrm{Re}_H = U_a H/\upsilon$, $Fr = U_a/\sqrt{gH}$

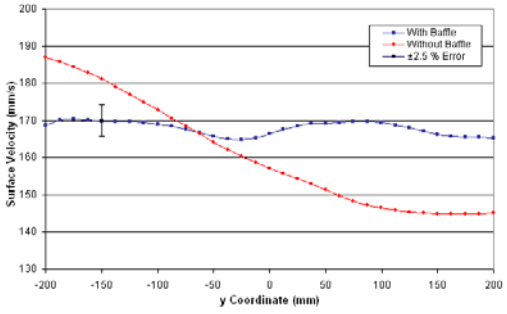

Figure B.3 – Velocity profiles along the transverse (y) axis of the PTV window for Run#1D. Flow parameters are outlined in Table A.2.

APPENDIX C

This appendix provides an outline of the methods used to optimise particle tracking costing strategies in Streamline 5.0, and also describes the costing strategies used in the present study.

C.1 OPTIMISATION OF COSTING STRATEGIES

Research by Nokes, et al (2003) outlined a number of non-dimensional parameters that could be used to optimise the performance of each costing strategy for use in a given flow. The non-dimensional parameters relevant to the costing strategies used in the present study are outlined below.

C.1.1 Distance Costing

The distance costing strategy is based on the assumption that particles move only a short distance between frames, relative to their inter-particle spacing. This strategy matches a particle in one frame to the particle in the next frame that is the shortest distance away from the original particle. A non-dimensional number (ρ_d) that relates particle displacement between frames to the inter-particle spacing is defined in Eq. (C.1), where U represents a typical velocity scale, Δt the time step between frames and ρ denotes the number of particles per unit area.

$$\rho_d = \frac{U\Delta t}{\left(1/\rho\right)^{1/2}} \tag{C.1}$$

The distance costing performs poorly for $\rho_d > 1$ and improves in performance as ρ_d tends towards 0.

C.1.2 Correlation Costing

The correlation costing strategy is a more complex strategy than the distance costing, and essentially is based on comparing particle patterns, within a user defined window, over two consecutive frames. This is accomplished by calculating the cross-correlation of particle intensities over two subsequent frames, within the user-defined window. Flows that contain significant velocity gradients place more demand on the correlation costing. Accordingly, a non-dimensional number, θ_c, that captures the effect of velocity gradients is defined in Eq. (C.2), where S represents a typical scale for velocity gradients in the flow, d_p is the typical particle diameter and W_c is the linear dimension of the user-defined correlation window.

$$\theta_c = \frac{W_c}{d_p} S\Delta t \tag{C.2}$$

The correlation costing performs poorly for $\theta_c > 1$ and improves in performance as θ_c tends towards 0. Two other factors affect the performance of the correlation costing. The first is the density parameter, ρ_c as defined in Eq. (C.3), that measures the number of particles in the correlation window. The second, denoted as C, in Eq. (C.4) is a measure of the proportion of the correlation window that is covered with particles.

$$\rho_c = \rho W_c^{\,2} \tag{C.3}$$

$$C = \rho \frac{\pi}{2} d_p^{\,2} \tag{C.4}$$

Nokes, et al (2003) found that provided $\theta_c < 1$, the correlation costing performs best when ρ_c exceeds approximately 10, and C is less than approximately 0.5.

C.1.3 Space-Average Velocity Costing

The space-average velocity costing is a match-based costing that relates the velocity of the particle of interest to the velocities of surrounding particles within a user-defined window An estimate of the number of particles in the user-defined window is denoted ρ_s and evaluated by Eq. (C.5), where ρ denotes the particle density as before and W_s is the linear dimension of the user-defined window. If matches within the user-defined window are incorrect then the velocity estimates within the window will be also be incorrect. A non-dimensional parameter that measures the percentage of correct to incorrect matches is denoted R_b (refer to Eq. (C.6)) which defines the ratio of the fraction of incorrect matches, F, to the fraction of correct matches, T.

$$\rho_s = \rho W_s^{\,2} \tag{C.5}$$

$$R_b = \frac{F}{T} \tag{C.6}$$

The optimum values for these non-dimensional numbers for the application of space average velocity costing is $\rho_s \sim 10$, $T \sim 1$ and $R_b < 1$. The values for F and T are difficult to quantify, but can be estimated from the observation of PTV matches after the implementation of state-based costing strategies (Ballard, 2004).

C.1.4 Recent Velocity Costing

The recent velocity costing is a matching based costing that uses the match of a particle in the previous frame to estimate the particle position in the next frame. A non-dimensional number used to evaluate the performance of the recent velocity costing are T and R_b as defined in Section C.1.3 as well as A_r, defined in Eq. (C.7), where A is a typical acceleration scale of the flow.

$$A_r = \frac{A\Delta t}{U} \tag{C.7}$$

The recent velocity costing performs most effectively when $T \sim 1$, $R_b < 1$ and $Ar < 0.03$.

C.1.5 Path Length Costing

The path-length costing removes particle paths whose length falls below a user-defined threshold. No evaluation of the performance of this strategy has been carried out. However for the present study this costing performed well to remove erroneous matches and also proved useful in removing matches found within agglomerated particles.

C.2 COSTING STRATEGIES

Costing strategies were selected based on the non-dimensional parameters outline in Section C.1, in combination with a process of trial and error. This section outlines the costing strategies used to track particles in the shallow shear flow and shallow turbulent wake regimes. For parameters used in each costing strategy refer to archived data at the University of Canterbury.

C.1.1 Shallow Shear Flow Regime

Since the all flows in this regime were plane, uniform flows (i.e. no significant velocity gradients) distance costing and recent velocity costing strategies proved sufficient for particle tracking purposes.

C.1.2 Shallow Turbulent Wake Regime

The shallow wakes created in the lee of an isolated cylinder required more complex costing strategies in order to track particles. Firstly a distance plus correlation costing was used to provide a first estimate of the particle tracks. Secondly a space average costing was used to refine particle matches and finally a combination of recent velocity and path length costings were employed. The recent velocity and path length costing proved reliable in removing erroneous particle tracks within agglomerated particles.

APPENDIX D

This appendix outlines the method used to obtain shear velocity and friction factor estimates for flow regime C.

The shear velocity, u_*, and Darcy-Weisbach friction factor, f, for each shallow, turbulent shear flow regime is displayed in Table D.1. The shear velocity was evaluated according to: $u_* = \sqrt{gRS}$, where R is the hydraulic radius and S is the channel slope. The friction factor was evaluated according to: $f = 8(u_*/U_a)^2$, where U_a is the cross-sectional mean velocity.

Table D.1 - Hydraulic parameters for flow regimes A, B and C.

Flow Regime	Slope S (rad)	Mean Velocity Ua (mm/s)	Depth H (mm)	Hydraulic Radius R (m)	Shear Velocity u* (mm/s)	Friction Factor f (-)
A	0.1280	1262.2	5.1	5.0	79.6	0.0318
B	0.0500	913.8	7.0	6.9	58.3	0.0326
C	0.0025	136.8	20.0	19.2	21.7	0.2018

Table D.1 indicates that the friction factor for flow regime C is a factor of approximately seven times greater than the friction factors calculated for Scenarios A and B. Furthermore a friction factor of 0.2 would correspond to a fully rough surface (Henderson, 1966), which is clearly incorrect.

The error in the friction factor calculation for flow regime C is believed to stem from errors in the channel bed slop calculation. The channel slope for regime C was determined to be 0.0025, which means that the elevation difference between the inlet and outlet of the flume is approximately 4.7*mm*. The elevation measurement accuracy of approximately $\pm 0.5mm$ leads to an error of $\pm 11\%$ in the slope calculation for regime C. Furthermore the tolerance in the channel bed was only $\pm 0.5mm$, leading to additional error in the channel slope calculation. These errors are consequently carried onto the estimates of the shear velocity and friction factor for regime C.

However, the error in the calculation of bed slope for regimes A and B was minimal (i.e. $\pm 0.5\%$). Therefore a more representative value of the friction factor for regime C was obtained by using an average roughness height, ε, obtained from flow regimes A and B using the Moody diagram. As the surface of the channel bed was the same for each regime, it is assumed that ε is a constant. The method for calculating the renewed friction factor for flow regime C is outlined on the following page.

From the Reynolds number ($\mathrm{Re}_{4R} = 4RU_a/\upsilon$) and friction factor for regimes A and B, an average relative roughness of ε=0.0001 was determined from the Moody diagram. Using this relative roughness parameter in conjunction with the Reynolds number ($\mathrm{Re}_{4R} = 10426$) evaluated for regime C yields a friction factor of f=0.0310 from the Moody diagram. The corresponding shear velocity, $u_* = U_a\sqrt{f/8}$, and friction coefficient, $c_f = f/4$, for regime C were recalculated based on f=0.0310 (refer to Table D.2).

Table D.2 - Re-evaluated hydraulic parameters for flow regime C.

Flow Regime	Friction Factor	Friction Coefficient	Mean Velocity	Shear Velocity
	f (-)	c_f (-)	Ua (mm/s)	u_* (mm/s)
C	0.0310	0.0078	136.8	8.5

APPENDIX E

Initial PTV testing indicated difficulties in obtaining turbulent intensity estimates for cylinders of diameter greater than three times the depth ($D > 60.4mm = 3H$). As is indicated in Figure E.1b, the the turbulent stress components, evaluated along the cylinder centreline for an 169.4*mm*=8.5*H* cylinder, deviate markedly when data obtained for cylinders at position A and B are superimposed (refer to Figure 6.2). Furthermore, this deviation was not localised to locations along the cylinder centreline, but evident over the whole PTV measurement field. However for the 3*H* cylinder, the turbulent intensity components plotted along the cylinder centreline (Figure E.1b) compared well with similar data obtained by v.Carmer (2005), plotted in Figure E.2. The following sections details an investigation carried out to determine the cause of the inconsistency.

E.1 EFFECT OF FLOW STRAIGHTENERS

Flow straighteners, as depicted in Figure 4.3, were used in all experiments carried out for the shallow turbulent wake regime. It was postulated that the disturbed flow that results upstream of a cylinder placed in a uniform flow (i.e. region (i) in Figure 3.5) was interacting with the flow straighteners when the cylinder was placed upstream at Position A (refer to Figure 6.2). To establish if this interaction contributed to the discrepancy between turbulent intensity measurements, three experimental runs were repeated for the 3*H* and 8.5*H* cylinders setup in Position A and B, with and without the presence of flow straignteners. The base flow was identical to flow regime C (refer to Table 5.1). The results from this investigation are displayed in Figure E.1, where FS denotes the experimental runs with flow straighteners, and NO FS, denotes experimental runs without the presence of flow straighteners.

Figure E.1a shows that the streamwise and spanwise turbulent intensity, u'_{irms}, evaluated for the 3*H* cylinder, are not affected by the presence of flow straighteners. Figure E.1b displays that the spanwise turbulent intensity evaluated along the centreline of the 8.5*H* cylinder located at Position A improves without the presence of flow straighteners. This suggests that flow straighteners effected the upstream flow conditions for the large cylinder case, which consequently affected flow conditions downstream of the cylinder. However the trends in the streamwise and spanwise turbulent normal stress components for the 8.5*H* cylinder still did not correspond to data obtained for the 3*H* cylinder, and turbulent intensity data obtained by v.Carmer (2005) plotted in Figure E.2.

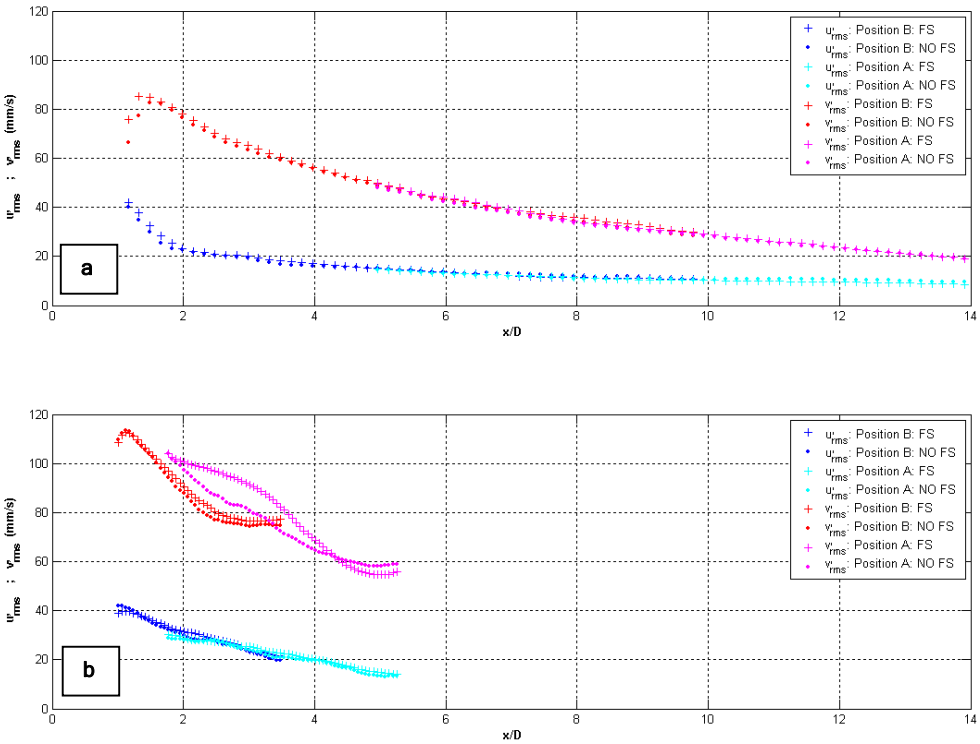

Figure E.1 (a) Streamwise and spanwise turbulent intensity components evaluated along the cylinder centreline for the 3H cylinder. **(b)** Streamwise and spanwise turbulent intensity components evaluated along the cylinder centreline for the 8.5H cylinder. Results obtained from cylinders located at positions A and B and each curve represents an ensemble average over three experimental runs.

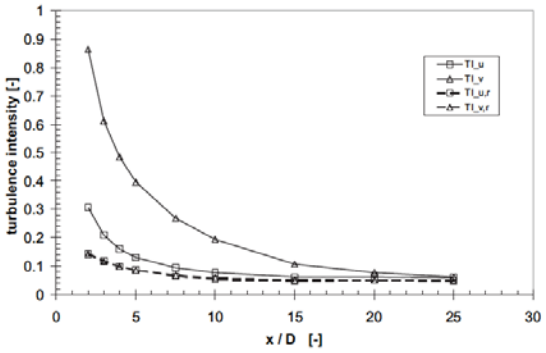

Figure E.2 - Turbulent intensity, normalised by U_a, evaluated along the cylinder centreline, using LDV, for a shallow VS flow with S_{sw}=0.07. $u_i'_{rms}/U_a$ is denoted as TI_{ui} (v.Carmer, 2005).

E.2 BLOCKAGE RATIO

The effect of the blockage ratio was secondly considered as a source of error. The blockage ratio is defined as the ratio of the cylinder diameter relative to the flume width. Cylinders of 3*H*, 4*H*, 5*H*, 6*H* and 8.5*H* were introduced into the flow and experimental runs were repeated three times. The base flow was identical to Scenario C (refer to Table 5.1). The turbulent intensity distribution along the cylinder centreline for each cylinder is plotted in Figure E.3, and the blockage ratio for each cylinder is listed in Table E.1.

Figure E.3b indicates that as the blockage ratio increases, a disturbance in the $u'_{i\,rms}$ is induced at ~x/D=5, and the spanwise turbulent intensity evaluated for the cylinder located at Position A deviates more markedly from the data obtained from the cylinder located at Position B. It is assumed that for blockage ratios greater than approximately 6%, the disturbed flow due to the presence of the circular cylinder is interacting with the sidewalls, and or, the downstream sluice gate, so as to introduce secondary disturbances into the flow. Indeed, Chen & Jirka (1995) stated that the ambient flow rate required adjustment for experiments with high blockage ratios, due to the increase in ambient velocity due to body displacement. As a result of these findings, analysis was restricted to flow around a 3H=60.4mm cylinder only.

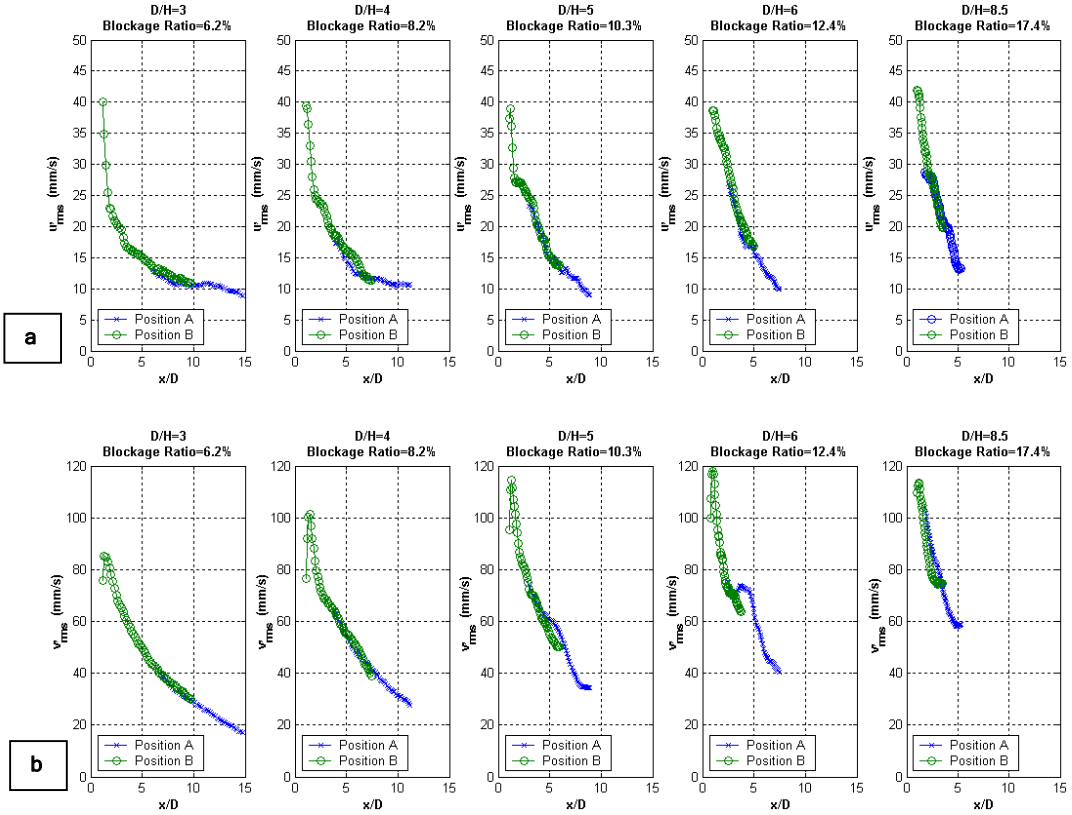

Figure E.3 - Turbulent intensity evaluated along the centreline of the PTV window for blockage ratios: 6.2%, 8.2%, 10.3%, 12.4% and 17.4%. **(a)** Plots the longitudinal turbulent intensity component and **(b)** plots the transverse turbulent intensity component.

Table E.1 - Cylinder diameters and blockage ratios for the cylinders used is the blockage ratio testing outlined in Section E.2.

Cylinder Diameter (D/H)	Cylinder Diameter (mm)	Flume Width (mm)	Blockage Ratio (%)
3.0	60.4	974	6.2
4.0	80.0	974	8.2
5.0	100.4	974	10.3
6.0	120.4	974	12.4
8.5	169.4	974	17.4

APPENDIX F

The development length of the turbulent boundary layer based on the formula, $\delta = 0.38x\left(U_a x/\upsilon\right)^{-1/5}$ (refer to Section 3.2.1 for definitions of the parameters in this equation), occurs at a distance of X~480mm from the channel inlet, for flow regime C (refer to Table 5.1, for the hydraulic parameters of regime C). However as outlined in Section 6.1.2, the circular cylinder was to be placed at X=385mm, in order to increase the downstream distance from the cylinder that could be analysed. To see if placing the circular cylinder in a transitional turbulent boundary layer had an affect on the mean-flow and 1D power spectral density estimate the following testing was carried out.

F.1 EXPERIMENTAL SETUP

In the following analysis capitals [X Y] are used to denote the coordinate axis for the channel bed, whilst lower case [x y] denote the coordinate axis for the PTV window (refer to Figure 5.1 for outline of the coordinate system).

A 120mm cylinder was used in the three experimental setups outlined in Figure F.1, and the base flow was identical to flow regime C (refer to Table 5.1, for the hydraulic parameters of this flow). Figure F.1a illustrates the "fundamental setup", in which the cylinder was located at [X Y]=[685 0], with the PTV window spanning a distance x/D=0 to 5 diameters downstream of the cylinder. This fundamental setup was used to compare the effect of:

i) Shifting the cylinder upstream to [X Y]=[385 0] into the transitional boundary layer, as well as shifting the PTV window upstream as illustrated in Figure F.1b.
ii) Shifting the cylinder upstream to [X Y]=[385 0] into the transitional boundary layer, as illustrated in Figure F.1c, but leaving the PTV window at the same location as the "fundamental setup".

Comparing the mean velocity profiles over the PTV windows, as well as the power spectral density at a location of [x/D y/D]=[3 0] for each setup illustrated in Figure F.1, would provide an indication if the structure of the wake was altered by placing the cylinder in a transitional turbulent boundary layer.

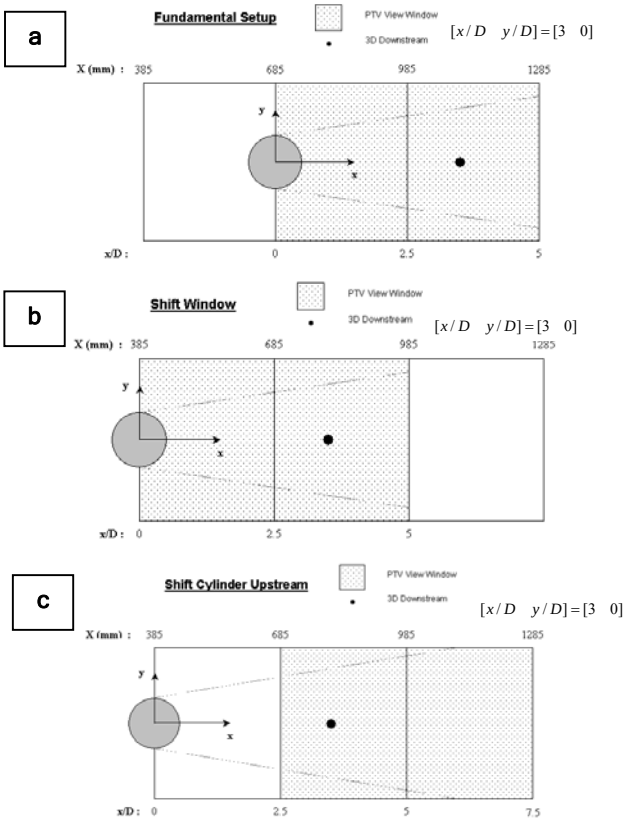

Figure F.1 - Experimental setups for transitional boundary layer testing (a) Fundamental setup: PTV window spans from [X Y]=[685 1285], cylinder located at X=685mm. (b) The PTV window is shifted upstream as well as the circular cylinder to a location of X=385mm (c) The cylinder is shifted upstream to X=385mm, but the PTV window is left in the same location as depicted in (a).

F.2 RESULTS

Figure F.2a and F.2b illustrate the mean longitudinal velocity profile, (i.e. $\overline{U}(x/D)$ for *y/D*=0) and mean transverse velocity profile evaluated at three diameters downstream of the cylinder (i.e. $\overline{U}(y/D)$ for *x/D*=3) for each setup illustrated in Figure F.1. For Figure F.2a it is expected that data obtained for *x/D*<2 is unreliable due to low particle density in this region, as explained in Section 4.3.2.3. However all other regions collapse with reasonable agreement. This implies that placing the cylinder in at [*X Y*]=[385 0], does not significantly influence the mean velocity profiles.

Figure F.2c plots the 1D power spectral density estimates for the transverse velocity component evaluated at [*x/D y/D*]=[3 0] for the experimental setups illustrated in Figure F.1. All PSD estimates collapse for each experimental setup, and the Strouhal number ($St=fD/U_a$) is in agreement with the value stated by v.Carmer (2005) for a shallow VS wake. This indicates that placing the cylinder in a transitional boundary layer does not influence the 1D PSD estimates.

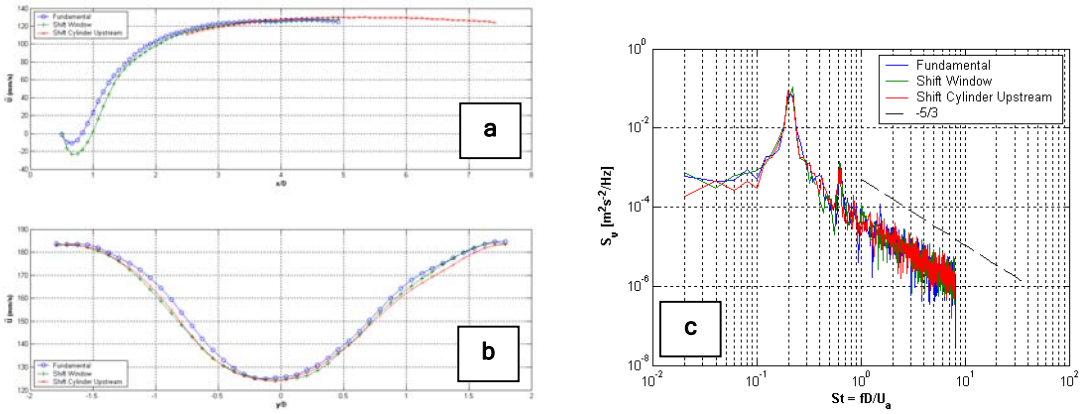

Figure F.2 – **(a)** Time-averaged streamwise velocity profile evaluated along the centreline of the PTV window, for the three experimental setups illustrated in Figure F.1 **(b)** Time-averaged streamwise velocity profile evaluated over the transverse axis of the PTV window, at x/D=3 for the three experimental setups illustrated in Figure F.1 **(c)** 1D power spectral density estimates for the transverse velocity component evaluated at a distance of [x/D y/D]=[3 0] for the experimental setups illustrated in Figure F.1.

In conclusion the testing outlined in this appendix illustrates that placing the circular cylinder in a transitional boundary (i.e. at [*X Y*]=[385 0]) does not significantly alter the mean flow and PSD estimates relative to a cylinder placed in a developed turbulent boundary layer (i.e. at [*X Y*]=[685 0]). This may be attributed to large-scale instabilities, which are generated by the circular cylinder, reorganising the flow structure irrespective of the boundary layer development. However it should be noted that prior testing outlined in Appendix E indicates that the turbulent intensity estimates are effected for cylinders with a blockage ratio of >6%.

APPENDIX G

This appendix presents the Kolmogorov and generalised structure functions evaluated from data obtained for the shallow shear flow and shallow wake flow regimes. Due to time constraints, these functions were not rigorously analysed and are therefore presented in this appendix for reference purposes.

G.1 SHALLOW TURBULENT SHEAR FLOWS

G.1.1 Generalised Structure Functions

Figure G.1a presents the generalised structure functions of order n=1 to 4, evaluated in the *temporal domain* for flow regimes A, B and C (refer to Section 5.1). Figure G.1b plots the power law exponent, ζ_n , against the order of the structure function, n, for flow regimes A, B and C. Each structure function

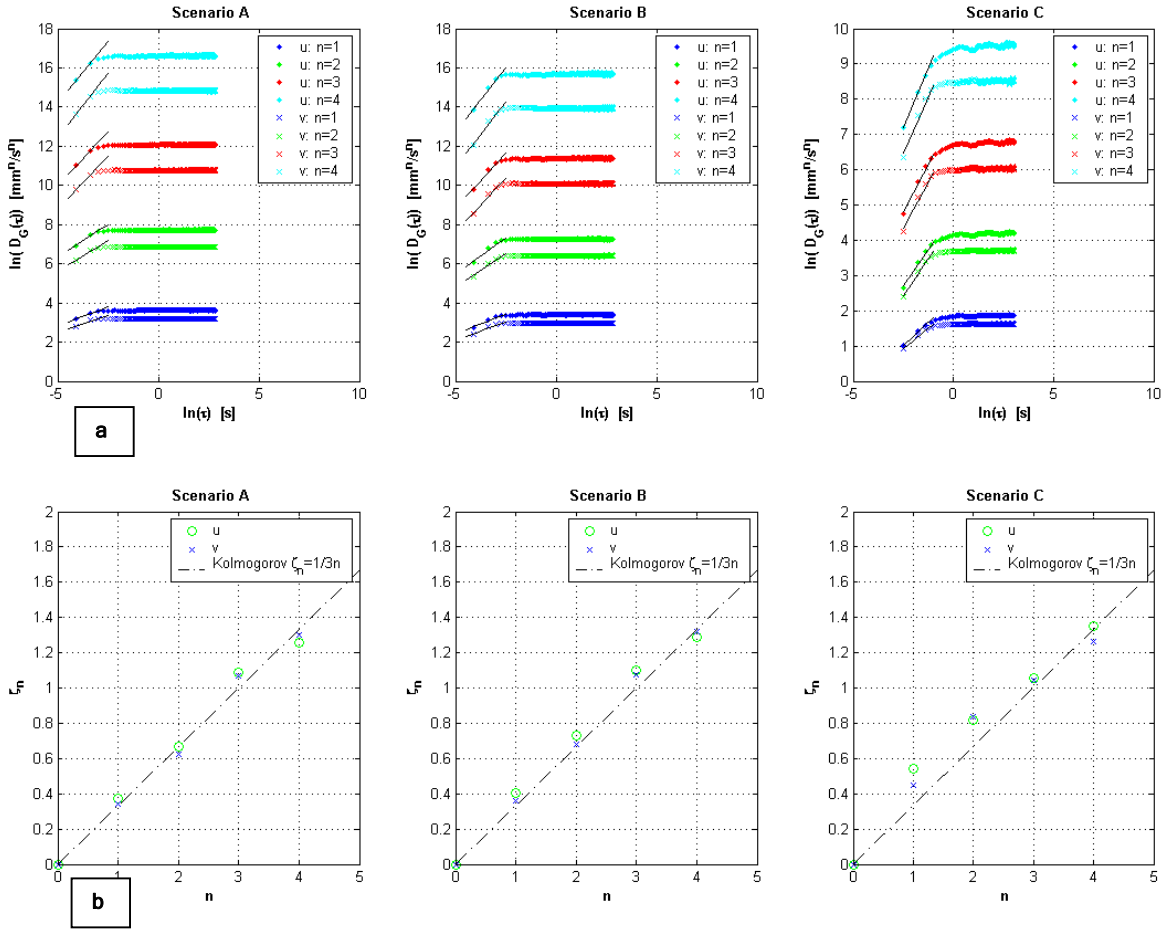

Figure G.1 – Temporal domain. **(a)** Generalised structure functions of order n=1 to 4, for the streamwise and spanwise instantaneous velocity. Data represents a space and ensemble average for time-histories at points along the x-axis. **(b)** Power law exponent (ξ_n) for the black lines of best fit in (a) plotted against the order of the structure function (n).

has been averaged over space and ensemble for the time-histories at points along the longitudinal centreline (y/D=0).

Figure G.2a presents the generalised structure functions of order n=1 to 4, evaluated in the *spatial domain* for flow regimes A, B and C. Figure G.2b plots the power law exponent, ζ_n, against the order of the structure function, n, for flow regimes A, B and C. Each structure function has been evaluated for the space-history along the longitudinal centreline of the flow field, ($u_i(x,0,0)$), and averaged over 800 time frames and ensemble.

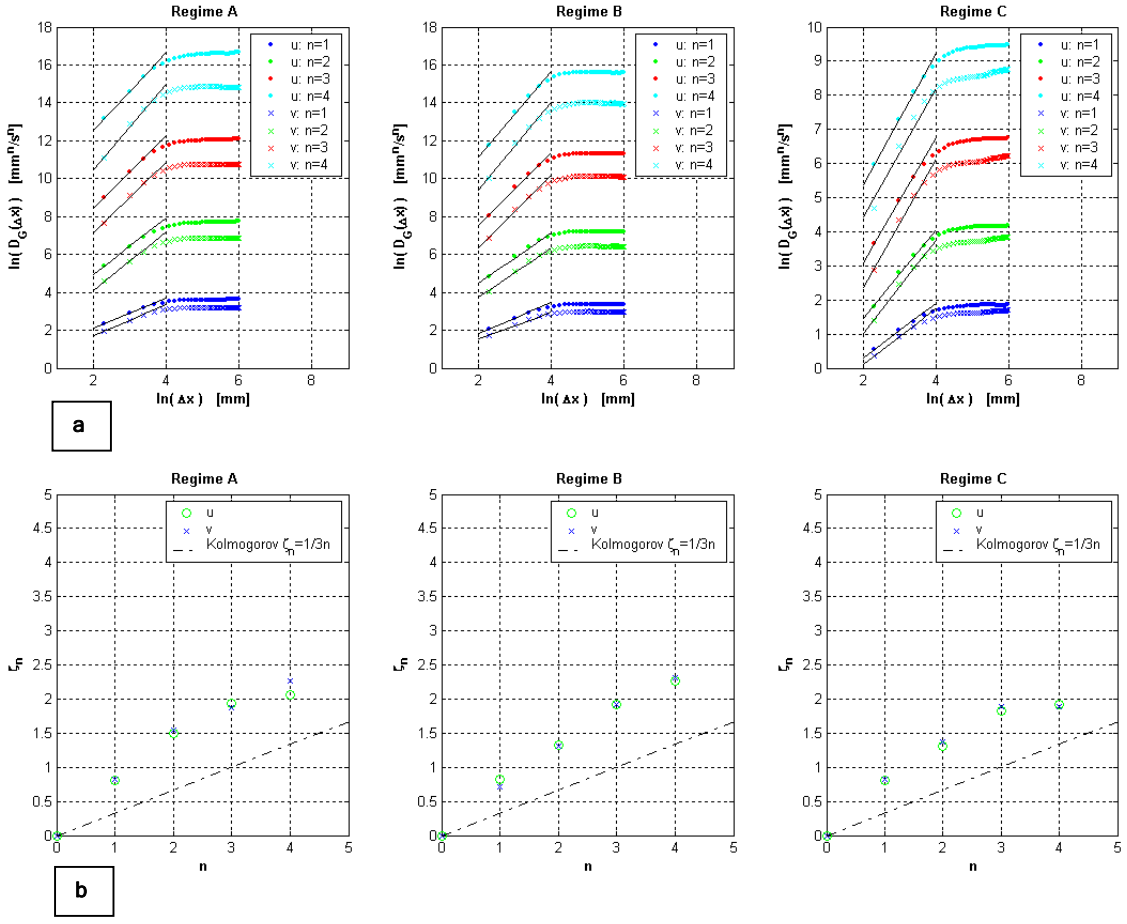

Figure G.2 – Spatial domain **(a)** Generalised structure functions of order n=1 to 4, for the streamwise and spanwise instantaneous velocity. Data represents a space and ensemble average for time-histories at points along the x-axis. **(b)** Power law exponent (ξ_n) for the black lines of best fit in (a) plotted against the order of the structure function (n).

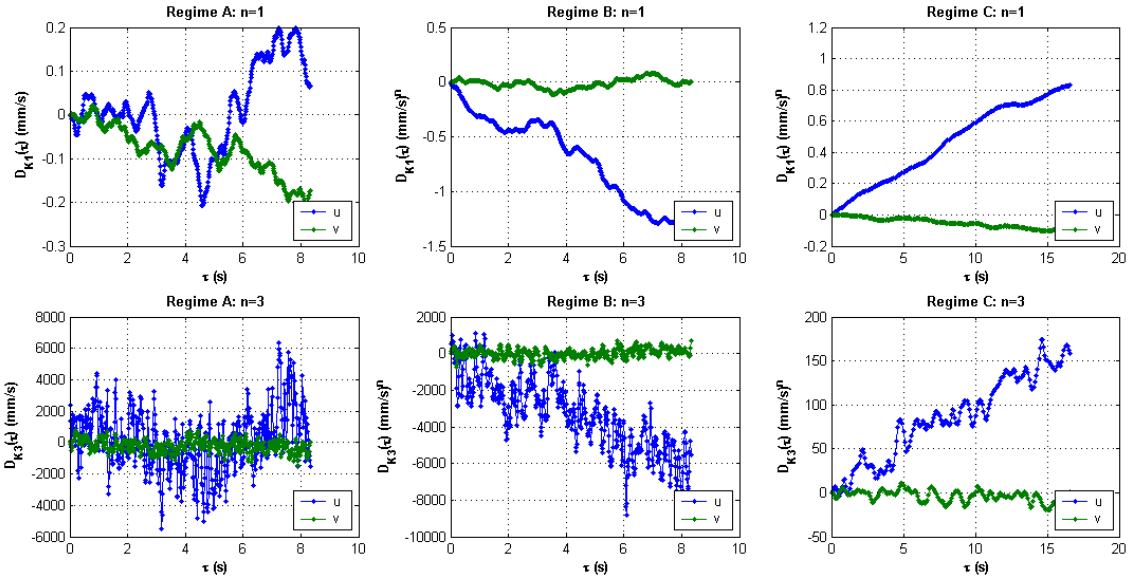

Figure G.3 - Temporal Domain: Kolmogorov structure function of order n=1 and n=3 for flow regimes A, B and C. Data represents a space and ensemble average for time-histories at points along the longitudinal centreline.

G.1.2 Kolmogorov Structure Functions

Figure G.3 presents the Kolmogorov structure functions of order n=1 and n=3 evaluated in the *temporal domain* for the streamwise and spanwise instantaneous velocity components. Each structure function has been averaged over space and ensemble for the time-histories at points along the longitudinal centreline (y/D=0).

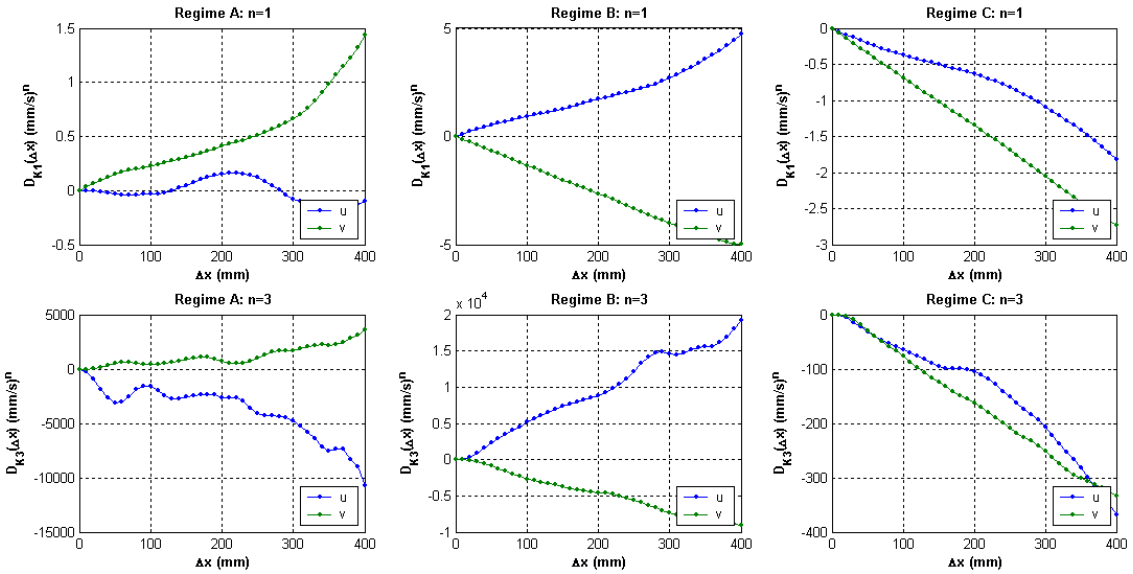

Figure G.4 - Spatial domain: Kolmogorov structure function of order n=1 and n=3 for flow regimes A, B and C. Data represents an ensemble average for time-histories at points along the x-axis.

Figure G.4 presents the Kolmogorov structure functions of order n=1 and n=3 evaluated in the *spatial domain* for the streamwise and spanwise instantaneous velocity components. Each structure function has been evaluated for the space-history along the longitudinal centreline of the flow field, ($u_i(x,0,0)$), and averaged over 800 time frames and ensemble.

G.2 SHALLOW TURBULENT WAKE FLOW

G.2.1 Generalised Structure Functions

Generalised structure functions have been evaluated for space-histories of the instantaneous streamwise and spanwise velocity components for the shallow turbulent wake flow regime (refer to Chapter 6). Space histories have been obtained in the longitudinal (x) direction for fixed values of y, over the range $6 \le x/D \le 12$ (refer to Figure 6.17). Figures G.5a and G.5c plot $D_{Gun_i}(\Delta x)$ and $D_{Gvn_i}(\Delta x)$ respectively for n=1 to 4 (tracking left to right). These figures are 2D surface plots, where the x-axis represents the transverse coordinate, normalized by the cylinder diameter, the y-axis denotes

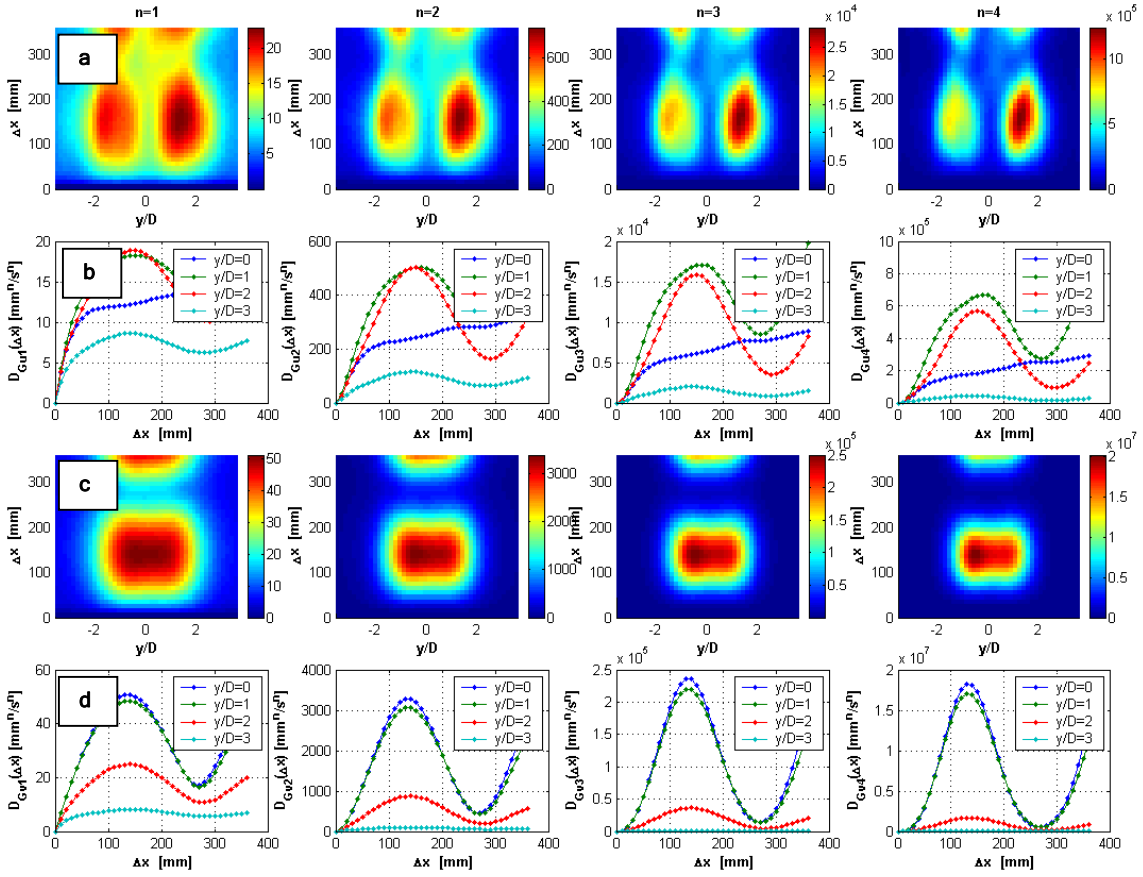

Figure G.5 - **(a)** $D_{Gun_i}(\Delta x)$ for n=1 to 4 **(b)** Cross-sections taken through (a) for designated values of y/D **(c)** $D_{Gvn_i}(\Delta x)$ for n=1 to 4 evaluated for space-histories **(d)** Cross-sections taken through (c) for designated values of y/D

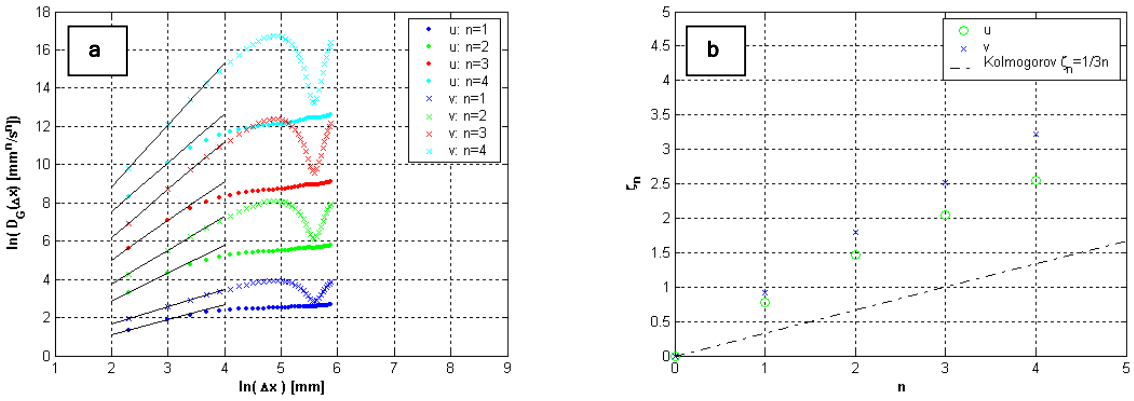

Figure G.6 - **(a)** Generalised structure functions of order n=1 to 4, for the streamwise and spanwise instantaneous velocity. Data represents a space and ensemble averaged for time-histories at points along the x-axis. **(b)** Power law exponent (ξ_n) for the black lines of best fit in (a) plotted against the order of the structure function (n).

the spatial delay (Δx) and the z-axis represents $D_{Gu_i n_i}(\Delta x)$ with units (m^{n_i}/s^{n_i}). Figures G.5b and G.5d depict cross section through the respective fields of Figures G.5a and G.5c for designated values of *y/D*. Each structure function represents an average over 800 time frames and ensemble.

Figure G.6a presents the generalised structure functions of order n=1 to 4, evaluated in the *spatial domain* for the structure functions plotted in Figure G.5 evaluated at *y/D*=0. Figure G.6b plots the power law exponent, ζ_n, against the order of the structure function, n, for the structure functions plotted in Figure G.5 evaluated at *y/D*=0.

G.2.2 Kolmogorov Structure Function

The third order Kolmogorov structure function has been evaluated for space-histories of the instantaneous streamwise and spanwise velocity components for the shallow turbulent wake flow regime (refer to Chapter 6). Space histories have been obtained in the longitudinal (x) direction for fixed values of y, over the range $6 \le x/D \le 12$ (refer to Figure 6.17). Figures G.7a and G.7b plot $D_{Ku3}(\Delta x)$ and $D_{Kv3}(\Delta x)$ respectively. These figures are 2D surface plots, where the x-axis represents the transverse coordinate, normalized by the cylinder diameter, the y-axis denotes the spatial delay (Δx) and the z-axis represents $D_{Ku_i 3}(\Delta x)$ with units (m^3/s^3). Figures G.5c and G.5d depict cross section through the respective fields of Figures G.7a and G.7b for designated values of *y/D*. Each structure function represents an average over 800 time frames and ensemble.

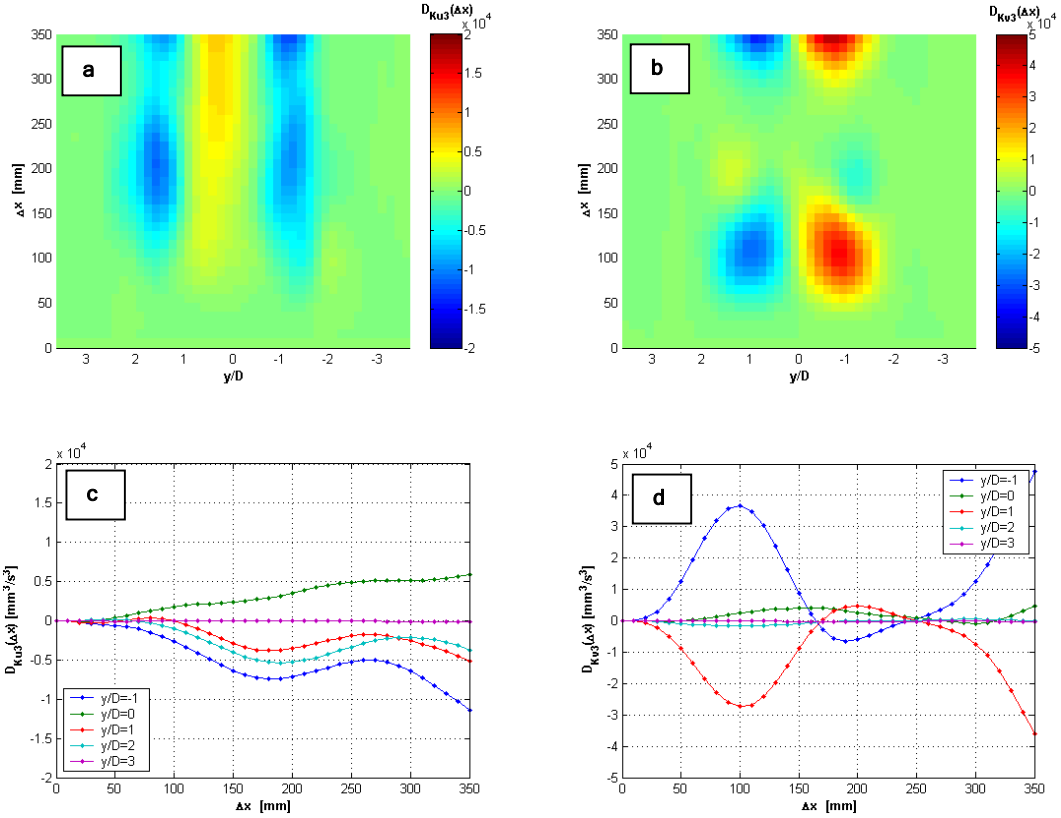

Figure G.7 - (a) $D_{Ku3}(\Delta x)$ evaluated for space-histories at points along the transverse axis **(b)** $D_{Kv3}(\Delta x)$ evaluated for space-histories at points along the transverse axis **(c)** Cross-sections taken through (a) for designated values of y/D **(d)** Cross-sections taken through (b) for designated values of y/D